Mesoporous Graphitic Carbon Nitride Supported CoPd Alloy Nanoparticles as Catalysts for Various Reactions of Terpenes

by

Ahsen Sare Yalın

A Dissertation Submitted to the

Graduate School of Sciences and Engineering

in Partial Fulfillment of the Requirements for

the Degree of

Master of Science

in

Chemistry

August 12, 2022

Mesoporous Graphitic Carbon Nitride Supported CoPd Alloy Nanoparticles as Catalysts for Various Reactions of Terpenes

Koç University

Graduate School of Sciences and Engineering

This is to certify that I have examined this copy of a master's thesis by

Ahsen Sare Yalın

and have found that it is complete and satisfactory in all respects,

and that any and all revisions required by the final

examining committee have been made.

Committee Members:

_____

Assoc. Prof. Önder Metin (Advisor)

_____

Assoc. Prof. Haydar Kılıç

_____

Assist. Prof. Safacan Kölemen

Date: 12.08.2022

Dedicated to my lovely family

ABSTRACT

Mesoporous Graphitic Carbon Nitride Supported CoPd Alloy Nanoparticles as Catalysts for Various Reactions of Terpenes

Ahsen Sare Yalın

Master of Science in Chemistry

August 12, 2022

Heterogeneous catalysis has attracted intensive attention due to the prevailing properties of heterogeneous catalysts such as high reusability and chemical stability. In recent years, 2D materials have found them enormous usage in heterogeneous catalysis owing to their unique optical, thermal, and electrical properties. Among them, mesoporous graphitic carbon nitride (mpg-CN) which is a polymeric, metal-free, non-toxic and low-cost material, has received great attention in the (photo)catalysis field. However, it suffers from several drawbacks such as fast charge carrier recombination and large band gap cause to construct heterojunction between another semiconductor or metal nanoparticles (NPs). Besides, the designing of platinum-group metals (PGM) based NPs have been dominating the heterogeneous catalysis field owing to their high catalytic activity, stability, and tolerance against poisoning. Among them, palladium (Pd) has gained the highest interest owing to its broader abundance and Pt-liked catalytic activity. Moreover, Pd demonstrates high activity in many organic reactions e.g. hydrogenation, dehydrogenation, oxidation, coupling reactions, etc. However, due to the current inflation in precious metals, Pd is the third most expensive PGM metals today, which limits its practical usage in industry. Hence, the last decade has witnessed the development of various bimetallic Pd alloys since they are more economical, and they boost catalytic activity compared to monometallic cunterparts owing to the synergistic effects between two divergent metals. However, a facile yet efficient synthesis of bimetallic PdM alloys, where M is the first-row transition metal, possesing high catalytic activity and stability is highly required to enhance their industrial usage.

In this thesis, we developed a facile synthesis protocol for the synthesis of designed novel heterogeneous catalysts composed of mpg-CN serving both as support and stabilizer and bimetallic alloy NPs and tested their catalytic activity in various reactions of terpenes including dehydrogenation, hydrogenation, and oxidation. For this purpose, mpg-CN was prepared by using a hard-template polycondensation method and exfoliated in solvent to anchor CoPd alloy nanoparticles between its nanosheets. In the presented protocol, mpg-CN served both as stabilizer and support material for yielded NPs. CoPd alloy NPs were obtained via the colloidal synthesis method in different compositions. The as-synthesized CoPd/mpg-CN nanocatalysts were characterized by using advanced techniques. The proposed synthetic method allowed to synthesize of nearly monodisperse CoPd alloy NPs with an average particle size of 3.0 ± 0.4 nm. After the construction of the prepared bimetallic alloys on the support material and a detailed investigation of their structural and photophysical properties, as-synthesized CoPd/mpg-CN nanocatalysts were utilized in dehydrogenation, hydrogenation, and oxidation of natural terpenes. Among all prepared CoPd/mpg-CN nanocatalysts, $Co_{37}Pd_{63}$/mpg-CN served the highest activity for all reactions. The dehydrogenation of 5 substrates was achieved in high conversion yields (≥91%). Also, the hydrogenation and oxidation products of several terpenes were

obtained, successfully. The reusability tests for dehydrogenation, hydrogenation, and oxidation showed that $Co_{37}Pd_{63}$/mpg-CN nanocatalysts can be reutilized up to 5 cycles without significant loss of its activity.

ÖZETÇE

Terpenlerin Çeşitli Dönüşüm Tepkimeleri için Mezogözenekli Grafitik Karbon Nitrüre Destekli CoPd Alaşım Nanokatalizörleri

Ahsen Sare Yalın

Kimya, Yüksek Lisans

12 Ağustos 2022

Heterojen kataliz, yüksek yeniden kullanılabilirlik ve kimyasal kararlılık gibi heterojen katalizörlerin üstün özelliklerinden dolayı yoğun ilgi görmektedir. Son yıllarda 2D malzemeler, benzersiz optik, termal ve elektriksel özellikleri nedeniyle heterojen katalizde kendilerine geniş kullanım alanı bulmuştur. Bunlar arasında polimerik, metal içermeyen, toksik olmayan ve düşük maliyetli bir malzeme olan mezogözenekli grafitik karbon nitrür (mpg-CN), (foto)kataliz alanında büyük ilgi görmektedir. Bununla birlikte, hızlı yük taşıyıcı rekombinasyonu ve büyük bant aralığı gibi çeşitli dezavantajlar başka bir yarı iletken veya metal nanoparçacıklar (NP'ler) arasında heteroeklem oluşturmaya neden olur. Ayrıca, platin grubu metaller (PGM) bazlı NP'lerin tasarımı, yüksek katalitik aktiviteleri, stabiliteleri ve zehirlenmelere karşı toleransları nedeniyle heterojen kataliz alanına hakim olmuştur. Bunlar arasında, paladyum (Pd), daha geniş bolluğu ve Pt benzeri katalitik aktivitesi nedeniyle en yüksek ilgiyi kazanmıştır. Ayrıca, Pd birçok organik reaksiyonda yüksek aktivite gösterir, örn. hidrojenasyon, dehidrojenasyon, oksidasyon, kenetlenme reaksiyonları vb. Bununla birlikte, Pd, endüstrideki pratik kullanımını sınırlayan üçüncü en pahalı PGM'dir. Bu nedenle, son on yılda, iki farklı metal arasındaki sinerjistik etkiler nedeniyle monometalik parçalara kıyasla katalitik aktiviteyi arttırdıkları için çeşitli bimetalik Pd alaşımlarının geliştirildi. Ancak, M'nin birinci sıra geçiş metali olduğu, yüksek katalitik aktiviteye ve stabiliteye sahip bimetalik PdM'nin kolay ve verimli sentezi, endüstriyel kullanımlarını geliştirmek için gereklidir.

Bu tez çalışmasında, mpg-CN ve CoPd alaşım NP'lerini içeren heterojen katalizörlerin sentezi için elverişli bir sentez metodu geliştirildi ve sentezlenen CoPd/mpg-CN nanokatalizörleri terpenlerin dehidrojenasyon, hidrojenasyon ve oksidasyon katalitik aktivitelerini test edildi. Bu amaçla, mpg-CN sert şablonlu polikondenzasyon yöntemiyle hazırlandı ve eksfoliye edildikten sonra nanotabakaları üzerinde CoPd alaşım nanopartikülleri sentezlendi. Geliştirilen protokolde, mpg-CN, elde edilen NP'ler için hem stabilizatör ve hemde destek malzemesi olarak görev yaptı. CoPd alaşımı NP'leri, kolloidal sentez yöntemi ile farklı kompozisyonlarda elde edildi. Sentezlenen CoPd/mpg-CN nanokatalizörleri, ileri teknikler kullanılarak karakterize edildi. Önerilen sentetik yöntem, ortalama parçacık boyutu 3.0 ± 0.4 nm olan neredeyse tek dağılımlı CoPd alaşımlı NP'lerin sentezlenmesine izin verdi. Hazırlanan bimetalik alaşımların destek malzemesi üzerine inşa edilmesinden ve yapısal ve fotofiziksel özelliklerinin ayrıntılı bir şekilde araştırılmasından sonra, sentezlenen CoPd/mpg-CN nanokatalizörleri, doğal terpenlerin dehidrojenasyonu, hidrojenasyonu ve oksidasyonunda kullanılmıştır. Hazırlanan tüm CoPd/mpg-CN nanokatalizörleri arasında, $Co_{37}Pd_{63}$/mpg-CN, tüm reaksiyonlar için en yüksek aktiviteyi gösterdi. 5 substratın dehidrojenasyonu, yüksek dönüşüm verimlerinde (≥%91) sağlandı. Ayrıca, birçok terpenin hidrojenasyon ve oksidasyon ürünleri başarıyla elde edildi. Dehidrojenasyon, hidrojenasyon ve oksidasyon için yeniden kullanılabilirlik testleri, $Co_{37}Pd_{63}$/mpg-CN nanokatalizörlerinin

aktivitesinde önemli bir kayıp olmaksızın 5 döngüye kadar yeniden kullanılabileceğini göstermiştir.

AKNOWLEDGEMENTS

Firstly, I would like to express my sincerest thank to my supervisor Assoc. Prof. Önder Metin for giving me a chance to be a member of Metin Research Group (MRG) and work with him during my Master journey. I am grateful to him for introducing me to the catalysis field. He affected my vision not only with his ambitious nature but also with his scientific knowledge. His desire for science remembered me of what I want to achieve. Also, I am very thankful for understanding when I could not think properly. He was more than a supervisor to me. He supported and trusted me in this journey. I could not achieve to complete this thesis without his help and guidance.

I would like to thank my jury members, Assist. Prof. Safacan Kölemen and Assoc. Prof. Haydar Kılıç for their time and interest. I owe to special thanks to Assist. Prof. Safacan Kölemen for his support and constant acceptance of my inquires. It was huge pleasure to meet with him and learn organic chemistry from him. Thank you very much for your cheerful conservations.

I would like to extend my thanks to Scientific and Technological Research Council of Turkey (TUBITAK) for the support (119Z199). Moreover, I am very grateful to Koç University Surface Science and Technology Center researchers for their guidance.

I would like to express my warmest thanks to Dr. rer. nat. Melek Sermin Özer, not only for her scientific perspective, expertise, and suggestions but also for her unique personality. This thesis could not be completed without her scientific vision. Her mentoring and guidance contribute to improving myself in every aspect of my life. Her precious heart, limitless energy, and charming smile have always enlightened my way. I am grateful for her endless support which gives shape to my scientific point of view and for trusting me. I could not imagine a life without her. Someday, even if we are not physically together, I will always feel her existence thanks to our intangible ties. Thank you to wait for me in the laboratory at late night, thank you to make me laugh, thank you to help me for finding my way in right direction, and thank you for being awesome.

I would like to express my gratitude to my lovely friend Güray Uluç Kaya for his endless support. Even when I did not believe in myself, he always had confidence in me. Even though I was the most overanxious person during my struggles, he attempted to keep me positive. I love learning, experiencing, and exploring a wide variety of things with him. I am grateful for all our wonderful moments.

I would like to thank my dear friends Aylin Kınık and Dilara Güntürkün for the past 7 years. I grew up with them and I learned with both of them how a friendship can be more than a friendship. In all my unforgettable moments, I was aways with them. Thus, I could not imagine how my life boring without you. Whenever I could not find strength, they were by my side to hold my hand all the time. I am incredibly appreciative of their endless love and support. I feel very lucky to have you. I hope we will share more dreams, more troubles, and joy for a long time.

I would like to thank Zafer Eroğlu for his assistance all the time. He answered all my questions, helped me in every scenario, and listen to my all complaints, forebearingly. I am appreciated his support during my journey. There are three amazing things that made by people from Erzurum. First one is cağ kebabı, second is kadayıf dolması, third one is Zafer Eroğlu. Thank you for your constant kindness to me.

I would like to express my appreciation to my dear friend Buse Sündü. She has never abstained to help me. She is not only a colleague but also a good friend. I am very thankful for your amazing friendship.

I would like to thank my friends Temirlan Kubanaliev, Aleyna Başak, and Sıla Alemdar for making the laboratory cheerful. Temirlan, thank you to teach me some Russian words. Aleyna, thank you for your splendid energy and laugh. Sıla, thank you for your joyful jokes.

I would like to express my deepest thanks to my dear friends Çağrı Özsan and Eda Kılıç. Our journey started at ITU, then proceeded at Koç University. Feeling their energy and support around me was consistently a tremendous treasure. I felt secure finding them in their laboratory whenever I went. After the exhausted working hours, our conversations have cheerred me up. Thank you for everything that you contributed to me.

I would like to thank Arda Görkem Tokur for being awesome. He is my joy. Thank you for the funniest jokes, thank you for your amazing energy, thank you for everything.

I would like to thank Dr. Sibel Eken Korkut, Seda Yılmaz, Begümhan Karapınar, and all Metin research group members for their unending supports in my journey. I always enjoyed our conversations and coffee breaks with Sibel Eken Korkut.

I would like to thank all the members of Kölemen research group. Especially, I would like to express my warmest gratitude to amazing scientists Sultan Çetin, Büşra Arslan, and Hande Gündüz for their supports.

I would like to thank my dear sister Sibel Gür for supporting me in every situation. She laughed with me in all my success. She held my hand when I fell. I am grateful to

my nephews Berra Gür and Emir Gür. Thank you for being such nice individuals. I am very lucky to have you. Also, I would like to thank my brother-in-law Coşkun Gür. He always supported me in all my decisions in his short life. I know you hear me in some way. I promise I will always guide your beloved children, Emir&Berra, and be with them in their troubles and happiness.

Also, I would like to thank Aysun Salman Tatlı for her precious support in my decisions that I have made.

Finally, I owe my special thanks to my mother Raziye Yalın, and my father Selahattin Yalın for trusting me and supporting me in all my decisions. They were always happier than me for my achievements. When I was under pressure and stressed, they always understood me and made me believe to get everything fine. I could not express how much I gratitude for their patience and love. I am always pushing myself to make them be proud. Thank you to let me be a person that I am shaped today. Thank you for everything!

TABLE OF CONTENTS

LIST OF TABLES

LIST OF FIGURES

ABBREVIATIONS

NP	Nanoparticle
BP	Black Phosphorous
h-BN	Hexagonal Boron Nitride
g-CN	Graphitic Carbon Nitride
mpg-CN	Mesoporous Graphitic Carbon Nitride
MOF	Metal Organic Framework
TMDs	Tarnsition Metal Dichalcogenides
VB	Valence Band
CB	Conduction Band
TGA	Thermal Gravimetric Analysis
PGM	Platinum-Group Metals
TOF	Turnover Frequeny
XRD	X-Ray Diffraction
XPS	X-Ray Photoelectron Spectroscopy
TEM	Transition Electron Microscope
HAADF-STEM	High-Angle Annular Dark Field Scanning TEM
BET	Brunauer-Emmett-Teller
PL	Photoluminescence
DMF	*N*,*N*-Dimethyl formamide
DCM	Dicholoromethane
CoPd	Cobalt-Palladium
ICP-MS	Inductively Coupled Plasma Mass Spectrometry
TRES	Time-Resolved Emission Spectroscopy
UV-DRS	Ultraviolet-Visible Diffuse Reflactance Spectroscopy
NMR	Nuclear Magnetic Resonance
GC-MS	Gas Chromatography Mass Spectrometry

Chapter 1:
INTRODUCTION

Pollution of natural sources such as water, soil, and air became one of the most critical problems that have to be fought in the 21st century. In this regard, green chemistry has received much more attention because of the requirement of ecological preservation. The actions related to green chemistry aim to decrease the usage of hazardous chemicals and increase the production of environmentally-benign substances. The advancements in catalysis play critical role to achieve the targets of green chemistry [1]. Catalysis term has been used for almost two centruies beginning from its first proposition by Jöns Jakob Berzelius in 1835 [2]. After Berzelius, many scientists have invested enormous efforts to produce new compound from small amounts of foreign substances. The reason behind of this phenomena was enlightened by Paul Sabatier (Nobel Prize in Chemistry, 1912) who contributed this field by explaining the reactive intermediates during catalytic reactions [2]. With all these breakingthrough scientific contributions, catalysis is described as the process which accelerates the chemical reactions and improve the yields while catalysts are substances expediting the reactions by proceeding them on a different pathway with a lower activation energy, they are not consumed during the reaction [3]. A typical catalytic effect is shown in Figure 1.1. High activation energy barrier of non-catalytic reactions is reduced by using catalysts. There are three types of catalysis: homogeneous, heterogeneous, and biocatalysis. Among these types, heterogeneous catalysis is a highly promising model due to its various extraordinary properties.

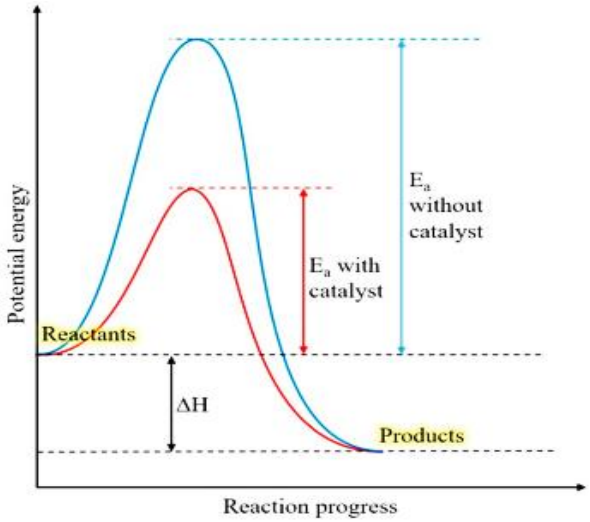

Figure 1.1: The effect of catalyst on a chemical reaction [4].

1.1. Heterogeneous Catalysis

Heterogeneous catalysis, where the substrates and catalysts are found in different phases, has one of the greatest shares of the development of many branches of science. Heterogeneous catalysis is typically composed of the catalyst in the solid phase and reactants in the liquid or gas phase. One of the most important advantages of heterogeneous catalysts is being easily recovered from the reaction medium. In a typical mechanism of heterogeneous catalysis, the reaction starts with adding the reactants and the catalyst to the reaction media. While the reaction proceeds, the surface of the catalyst serves as active sites for the reactants and the product is yielded after many steps (Figure 1.2) [5]. According to surface adsorption theory, the reaction starts with chemisorption between the surface of the catalyst and the substrates. The bonds of the reactants on the surface of the catalyst break via dissociation, thus; the new bonds between reactants establish on the surface of the catalyst. Desorption of product(s) from the surface is the last step in the process [1]. At the end of the reaction, the structurally altered catalyst reverts and are recovered as very similar to its original form [5].

Heterogeneous catalysts possess many advantages over homogeneous ones in terms of industrial applications and thus most industrial chemical processes are utilized heterogeneous catalysts. For example, the separation of homogeneous catalysts from the reaction media is very difficult but it is easy for the heterogeneous ones, which is the greatest advantage that overrides homogeneous catalysts. Moreover, recycling of homogeneous catalysts is challenging and high-cost while heterogeneous catalysts are regenerated effortlessly. Diffusion control is not possible since the homogeneous catalysts and reagents are in the same phase. However, diffusion can be controlled in the presence of heterogeneous ones. Additional purification steps should be provided for homogeneous catalysts but heterogeneous one requires fewer step [6]. Despite the drawbacks such as low selectivity and activity, the assets such as high stability and reusability make desirable the utilization of heterogeneous catalysts in industrial applications [7]. Hence, the development of synthetic methodologies for the preparation of heterogeneous catalysts is essential to constructing efficient and reliable catalysts for possible industrial applications [8,9]. Besides these approaches, nanomaterials have been recognized as an alternative to improve the selectivity and reactivity of heterogeneous catalysts. Among the reasons for the widespread usage of nanomaterials in industry and

academia, 2D semiconductors which are classified as nanomaterials are used as heterogeneous catalysts.

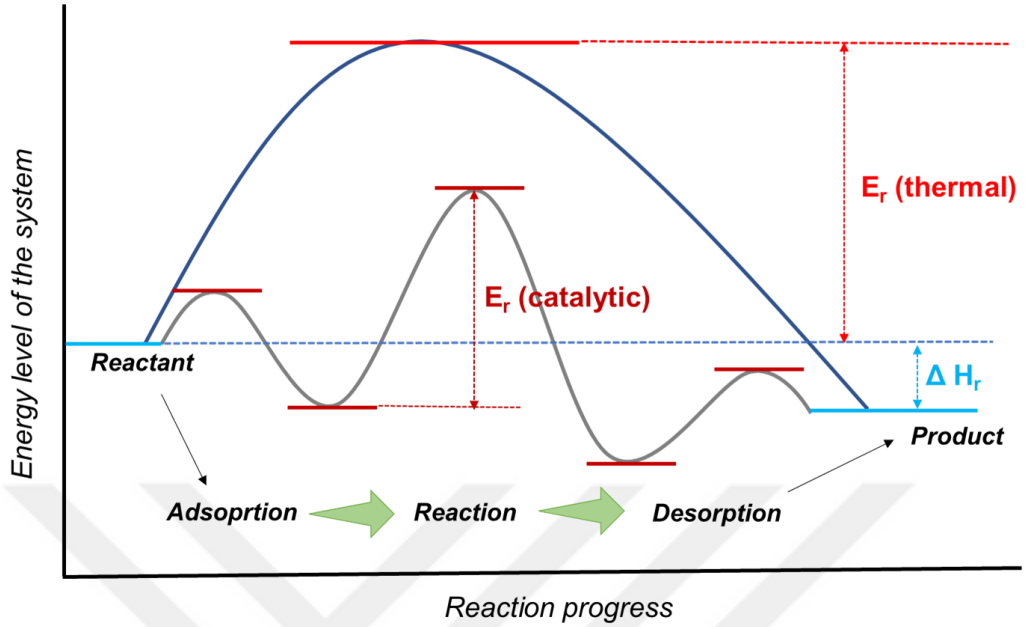

Figure 1.2: Mechanism of heterogeneous catalysis.

1.2. Nanomaterials and 2D Semiconductors

The materials whose at least one dimension is lower than 100 nm are called nanomaterials [10]. Nanomaterials are attractive functional materials due to their superior properties such as large surface area, excellent stability, lower density, high electron transfer rate, good light-collecting characteristic, easy preparation, and good biocompatibility [11,12]. Nanomaterials can be classified depending on their dimensions, namely 0D, 1D, and 2D materials available in these groups (Figure 1.3). The most prevalent kind of nanomaterials is zero-dimensional nanoparticles, which have dimensions that are on the nanoscale. These nanoparticles are tiny particles that resemble points, or spherical nanoparticles. Quantum dots, fullerenes, hollow spheres, nanolenses, rings, and atomic clusters are some of the most prevalent instances of these particles [13,14]. One such class of nanomaterials is called 1D materials, which include nanoparticles with at least one dimension greater than nanoscales and have additional dimensions that lie within the nano range. Nanofibers, nanotubes, and nanorods are the most typical types of 1D nanomaterials [13,14]. The final category of nanomaterials is referred to as 2D materials. These nanomaterials have two additional dimensions compared to the nanoscale (100 nm). Nanofilms, nanolayers, and nanocoatings are the most typical instances of this class. The nanomaterials in this category have plate-like structures [13,14].

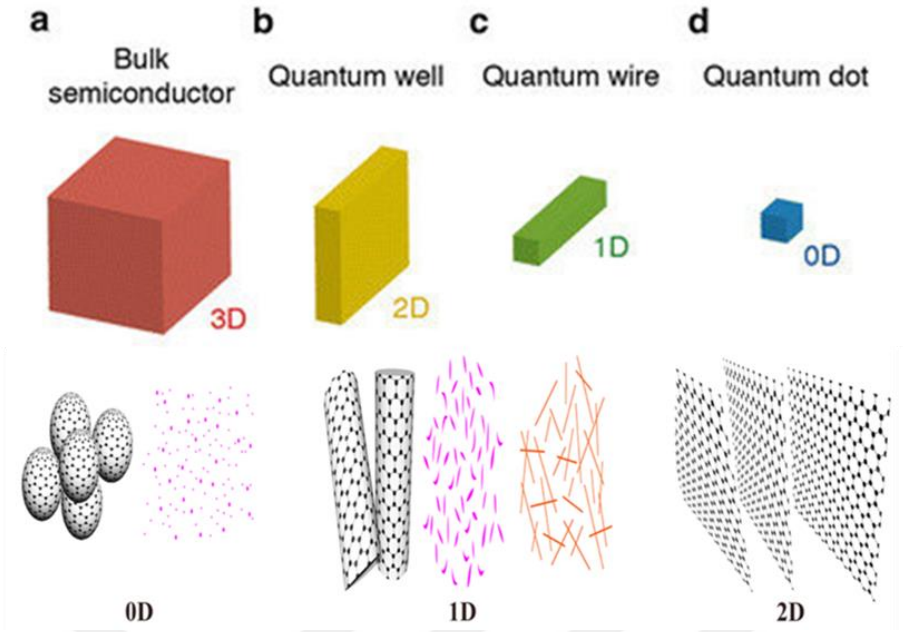

Figure 1.3: Classification of materials depending on their dimensions [15,16].

The most significant and famous example of 2D materials can be exemplified as graphene. The research conducted by Novoselov and Geim on graphene, a form of 2D graphite, earned them the 2010 Nobel Prize in Physics [17]. Graphite is composed of monolayers, termed graphene, which have a honeycomb structure. These monolayers are linked together by weak van der Waals forces [18]. The first step in isolating graphene layers, which took place 440 years after its creation, was the work that received the Nobel Prize [17]. Moving between two-dimensional planes is permitted for electrons. The limitation of the third direction and the isolation of graphene demonstrated that this material had distinct electrical and optical characteristics [19]. Electronics, optoelectronics, communications, and sensing are a few of the many vital application fields for semiconductors [20]. Since then, many 2D materials, a nanosheet-type nanostructure, have attracted great attention by scholars. A variety of 2D semiconductor materials, including graphene-based materials, black phosphorus (BP), hexagonal boron nitride (h-BN), graphitic carbon nitride (g-CN), metal-organic frameworks (MOF), transition metal oxides, and transiton metal dichalcogenides (TMDs), have already been synthesized and developed [21–23]. In Figure 1.4, the structures of several 2D materials are depicted.

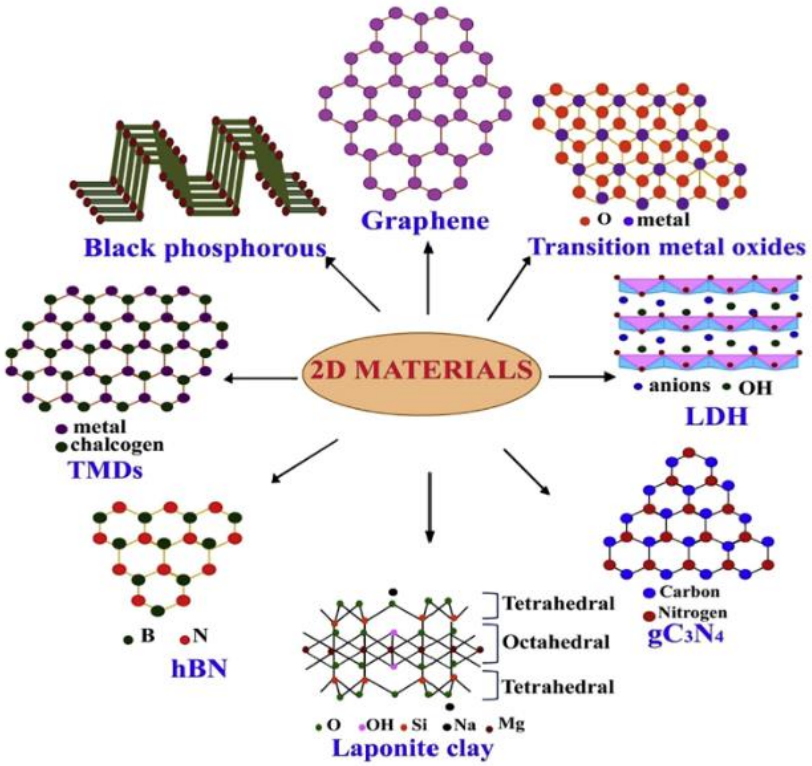

Figure 1.4: The structures of different types of 2D materials [24].

In light of the aforementioned properties of 2D materials, their application areas expand continuously. The most significant usage of 2D semiconductors is in the catalysis field. Due to the good light harvesting properties of 2D semiconductors, they are encountered in photocatalysis, greatly. The working principle of these semiconductor materials is illustrated in Figure 1.5. Upon light irradiation, excitation of electrons which are located at the valence band (VB) of the material through the conduction band (CB) occurred. During the excitation, positively charged holes are formed in VB and negatively charged electrons are accumulated on CB. Excited electrons can be used in the reduction reactions while holes contribute to oxidation. Even though 2D semiconductors have been developed in various applications, their pristine forms still suffer from low catalytic activity due to their low surface area, high charge carrier recombination, weak light absorption, and low chemical stability. To improve the efficiency of 2D materials in photocatalysis, many scientists have made different approaches to improve these shortcomings of 2D semiconducting materials. 2D semiconductors can be boosted to achieve superior settings by modifications such as doping, heterojunctions, surface/defect engineering, and so on [25]. The heterojunction is one of the most effective ways to enhance the diverse properties of 2D semiconducting materials for desired catalytic applications. Therefore, the following section is dedicated to the topic of heterojunctions.

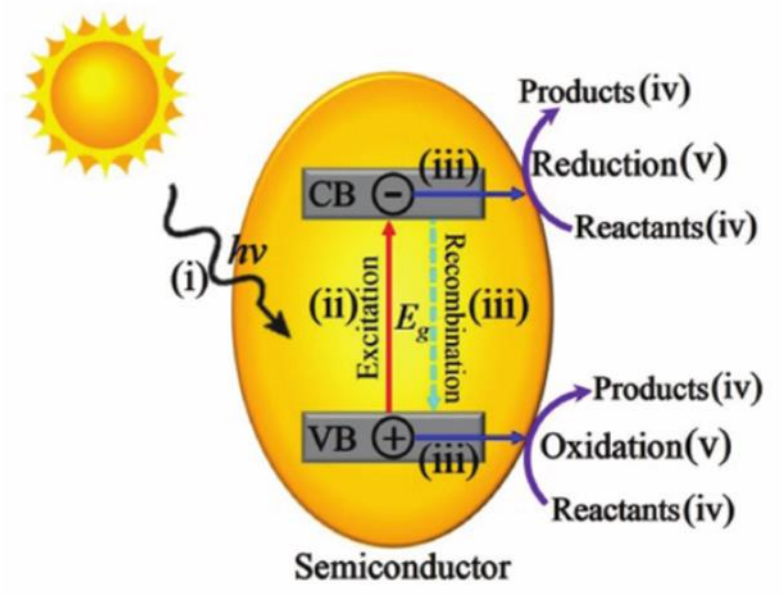

Figure 1.5: Schematic illustration of a photocatalytic mechanism in the presence of a semiconductor photocatalyst [26].

1.3. Heterojunctions

To decrease the charge carrier recombination of electron/hole pairs in pristine semiconducting materials, some modifications such as the construction of heterojunctions are needed. Heterojunction means an interface that is created between two regions of different semiconductors with distinct band gaps and optical properties [25]. There are several ways such as morphological modification and designing of nanostructures to optimize the energy band structure of two different semiconductors. However, these methods are not sufficient to achieve the perfect result due to their drawbacks such as increased recombination centers and distribution disorders. Herein, the heterojunctions become a part of activity [27]. Heterojunctions are composed of one or two photocatalysts and a cocatalyst [27,28]. It can be classified as 0D/2D, 1D/2D, and 2D/2D heterojunctions. 2D/2D heterojunction shows greater stability and connection of interfaces, by comparison, 0D/2D and 1D/2D [27]. Due to these prevailing properties, 2D/2D heterojunction will be mentioned in this part. This type of heterojunction system can be divided into four groups which are type-I, type-II, type-III, and Schottky junction. These heterojunction systems are illustrated in Figure 1.6.

In type-I heterojunction, the valence band (VB) and conduction band (CB) energy levels of the second semiconductor are lower than the first one. Thus, generated electrons and the holes in the first semiconductor move to the CB and VB of the second semiconductor [29].

In type-II heterojunction, it is known as staggered type alignment. CB and VB levels of one semiconductor are lower than another. Hence, the electrons flow through CB with lower energy, and the holes move through VB with higher energy. It causes electrons and holes to gather in different semiconductors [29].

In type-III heterojunction, it is the broken gap. When CB and VB levels of one semiconductor are very high, another one is vice versa. The bands of semiconductors do not correspond, so electron and hole flows do not exist [29].

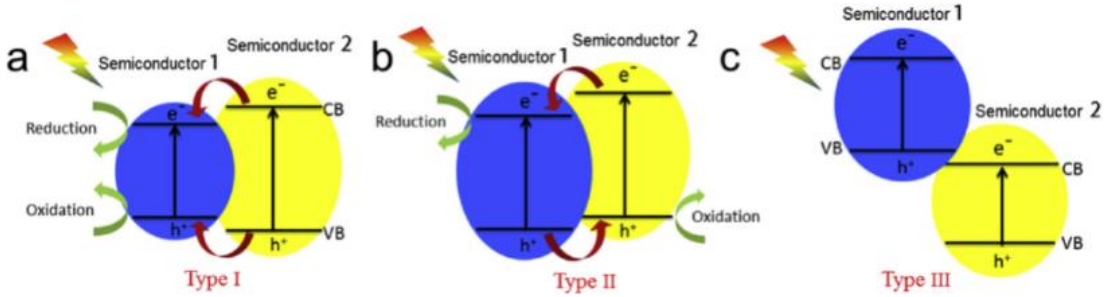

Figure 1.6: Different heterojunction systems (a) Type-I (b) Type-II (c) Type-III [30].

In the Schottky junction, a semiconductor and a conductive material such as noble metals, non-noble metals (e.g. Bi), graphene, etc. are required. The direction of the flow of charges is from the semiconductor to the conductive material. They transfer in that direction until the new equilibrium between their Fermi levels is constructed. Therefore, an electric field is created between the interfaces of metal-like material and semiconductors [27]. Its principle is shown in Figure 1.7.

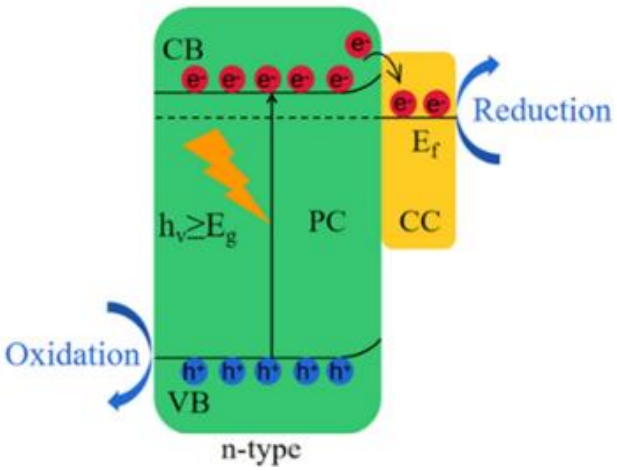

Figure 1.7: Illustration of a typical Schottky junction [27].

As mentioned above, conductive materials such as metal nanoparticles are required to create Schottky junction. Bimetallic nanoparticles can also be used for this purpose,

which is within the context of this thesis. It is important to know what bimetallic nanoparticles are along with their differences from monometallic ones, which are the topic of following section.

1.4. Monometallic and Bimetallic Nanoparticles

Nanoparticles (NPs) are solid particles with the size in the range of 10 to 100 nm. The properties of nanoparticles vary from their conventional solid forms. Their properties are observed as neither bulk material nor atomic/molecular structures. The form of nanoparticles may be in amorphous or crystalline form [31]. Nanoparticles may be divided into a number of groups based on their chemical composition. Pure metal nanoparticles are among the oldest and most widely utilized nanoparticles in science due to their exceptional physical features such as catalytic, structural, electronic, and optical. These unique qualifications cause their usage in diverse application areas such as catalysts, biosensors/sensors, nanoelectronic devices, and biomedical appliances [32,33]. Due to the widespread application areas of nanoparticles including catalysis, the development of a facile yet efficient methodologies for their synthesis is essential. There are two techniques to synthesize the nanoparticles (Figure 1.8). The first one is the top-down approach which is based on breaking bulk materials into nanoparticles and is sorted as following: ball milling, chemical etching, sputtering, explosion processes, thermal/laser ablation. The other one is the bottom-up approach which allows uniting the bulk material from nanoparticles and is classified as precipitation, vapor deposition, condensation, sol-gel processes, spray pyrolysis, laser pyrolysis, and aerosol processes [31,34].

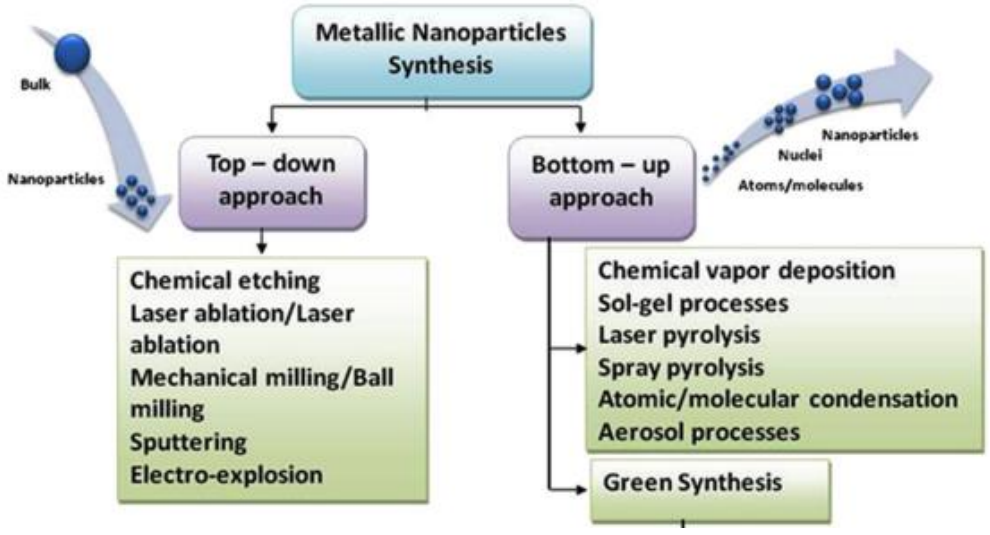

Figure 1.8: Different synthetic approaches for preparation of nanoparticles [35].

Synthesis strategies affect their morphology, composition of metals (alloy or core-shell), and structure which designate the applicability of nanoparticles [32,36,37]. Nanoparticles synthesized from only one noble metal are known as monometallic NPs, whereas those made from two distinct metals are defined as bimetallic NPs [38]. Because of the problems such as low surface absorption between the catalyst and reagent, the limited number of active sites, the catalytic performance and selectivity of monometallic NPs can be inadequate in some particular processes. Bimetallic NPs are therefore highly regarded for improving catalytic activity [39]. Catalytic performances of bimetallic nanoparticles surpass monometallic ones thanks to the synergistic effect between two diverse metals in the nanoparticle composition and splendid tunability in compositions and structures [40]. The electronic and geometric structures of NPs can be brought into compliance with the inclusion of a second metal in structure to reinforce the catalytic activity and selectivity [41,42]. Moreover, the extensive surface area of bimetallic nanoparticles provides them with huge adsorption power; thus, bimetallic nanoparticles show performance as more effective catalysts than monometallic ones [31]. Moreover, combining noble metals with transition metals such as Fe, Ni, and Co diminishes the content of noble metals and the cost of the catalyst [43].

The characteristics of bimetallic NPs differ depending upon their structures and the metals which are changed with synthesis procedures. Bimetallic nanoparticles can be found in distinctive forms such as core-shell, alloy, and cluster as shown in Figure 1.9 [31]. In core-shell structure, first step is reduction of one of the metals in catalyst to form the core and the growth of the other metal as a shell around the core is the following part. If the two metals mix in a homogeneous way with formation of metal-metal bond, it is called as alloy NPs. Clusters occur with the growth of two metals in a mixed interface and separate nucleation process [43].

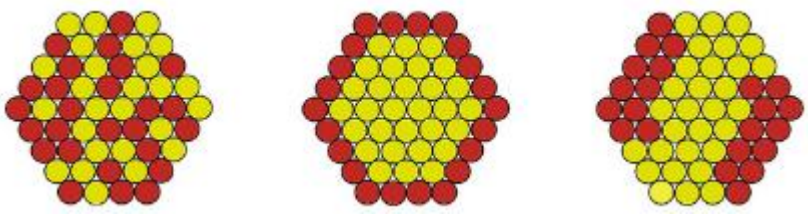

Figure 1.9: Different forms of bimetallic nanoparticles (a) alloy (b) core-shell (c) cluster [44].

In this section of the thesis, the properties, application fields, and different types of nanoparticles are summarized. Considering all of these, Pd-based bimetallic alloy NPs were formed in the context of this thesis. The other important point of this thesis is the use of semiconductor material, namely mesoporous graphitic carbon nitride (mpg-CN) as support material and stabilizer for the generated alloy NPs will be mentioned in the following part.

1.5. Mesoporous Graphitic Carbon Nitride (mpg-CN)

Graphitic carbon nitride is a polymeric semiconductor that has attracted great attention in research recently [45,46]. Berzelius constituted the polymeric derivative of carbon nitride and Liebig entitled melon in 1834 as shown in Figure 1.10 [47]. Franklin identified the structure of the compounds in 1922 and suggested the notion of carbonic acid (C_3N_4) [48].

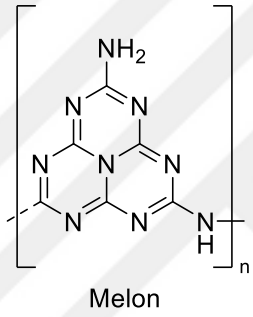

Figure 1.10: Melon structure as described by Liebig.

In 1937, tri-*s*-triazine unit in the graphitic carbon nitride was proposed as the basic structural pattern by Pauling and Sturdivant [49]. In 1940, the similarity between melon and graphite was expressed by Redemann and Lucas because of the planar and large structures of them. Compact condensation product with 21 molecules as $C_{126}H_{21}N_{75}$ molecular formula was close to Franklin's material which probably involved larger and smaller units together [50]. Theoretical predictions indicated high bulk structure and hardness resemblance between β–CN which is sp^3 hybridized C_3N_4 and diamond [51–55]. In light of these, further research studies started to prepare and characterize β–CN [56–61]. Low thermodynamic stability of β–CN phase caused complicated synthesis of the material [62]. Theoretical studies demonstrated that the most stable allotrope is g-CN at ambient conditions [54, 63–65]. To synthesize an excellent crystalline carbon nitride was always demanding. However, highly crystalline melon synthesis was achieved by Komatsu [66,67]. Moreover, crystal structures of melem and melam were determined by Schnick et al. [68,69]. McMillan et al. reported that a high crystalline carbon nitride imide

phase was observed via dicyandiamide precursor under high temperature and pressure [70]. Graphitic carbon nitride (g-CN) shown in Figure 1.11 is one of the most popular metal-free and non-toxic 2D semiconductor that spreads in various applications such as photocatalysis, biosensing, environmental remediation, etc. [71,72]. Since g-CN has huge potential to utilize in different fields, diverse synthesis methodologies have been proposed by many researchers from various precursors such as cyanamide, melamine, urea, etc.

Especially, it works effectively in the visible-light range with a band gap of ~2.7 eV (454 nm) [73,74]. The drawback of g-CN is being suffered from the fast recombination of charge carriers [73]. As mentioned in section 1.2, the coupling of g-CN with semiconductors and metals is one of the options to enrich the catalytic properties.

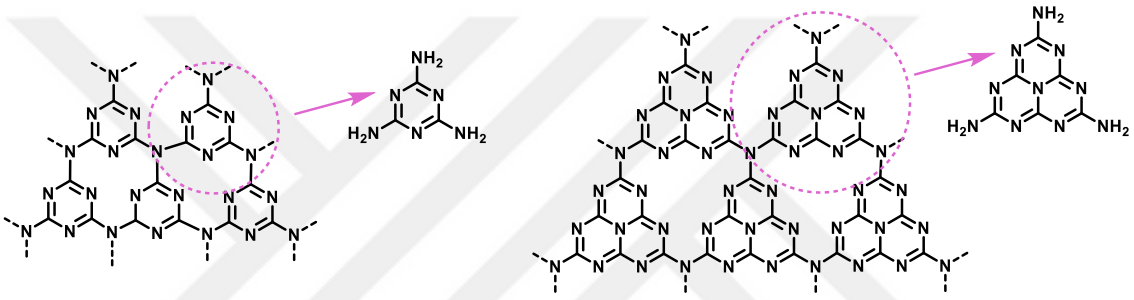

Figure 1.11: s-triazine unit (left), tri-s-triazine unit of g-CN (right).

Also, the further development of bulk g-CN is limited by general bulk material flaws such as limited specific surface area and fewer active sites. Support material should have a large surface area and suitable functional groups for metal decoration on its surface. Recent decades have seen a surge in interest in mesoporous materials. Because of the 2–50 nm pore channels that exist inside of them, mesoporous materials are renowned for having superior characteristics and possible uses compared to bulk materials [75,76]. Mesoporous materials, in general, offer several excellent qualities, including a very high specific surface area, an organized pore structure, a reduced density, more active sites, and a powerful capacity for adsorption [77–79]. Xu et al. achieved an increased surface area of g-CN up to 200 m^2g^{-1} by applying the hard template method in the presence of silica [80]. The improved material entitled mesoporous graphitic carbon nitride is a suitable support material due to its high surface area and its functional groups [73,81]. After that, nanoarchitecture studies of g-CN continued through several methods such as template method, exfoliation, and template-free strategy [82]. Therefore, g-CN with various nanostructures could be improved such as 0D nanodots, 1D nanostructures, 2D

nanosheets, and mesoporous structures [83–86]. Due to the several advantages of mpg-CN such as high surface area, large pore volume, easy preparation, etc., mpg-CN is utilized as a metal-free catalyst in many fields.

It is mentioned that the properties of mpg-CN make it desirable in different fields so far. The properties of mpg-CN will be mentioned in the context of thermal and chemical stability, optical and photoelectrochemical properties. To decide the thermal stability of mpg-CN, thermal gravimetric analysis (TGA) is used. It is observed that this material is quite stable up to 600 °C. The peak which is observed at 630 °C and the weight loss at this temperature indicates that decomposition of mpg-CN starts at this temperature. Analysis continues until any residue of material remains and it is observed that mpg-CN decomposes at 750 °C completely. This kind of thermal stability is one of the top ones for that kind of organic material. However, it should not be forgotten that changing of synthetic procedure alters the thermal stability of g-CN. Since different methods affect the degrees of polymerization [45,87]. To determine the chemical stability of g-CN, some tests are indicated in the literature. Carbon nitride has van der Waals interactions between its single layers. These interactions resist the solubility of g-CN in different solvents such as water, alcohols, DMF, THF, ether, and toluene. The situation changes in the presence of alkali and acidic media. When carbon nitride is exposed to alkali metal hydroxides, structural decomposition is observed. In the presence of concentrated acids, the observation of sheet-like dissolution is expected [45]. To observe the optical and photochemical properties of g-CN, UV-Vis and photoluminescence experiments are required. The classic absorption pattern whose organic semiconductor is observed for graphitic carbon nitride and bandgap adsorption is nearly 420 nm. The absorption of carbon nitride lightly depends on the synthesis method because of influences on the packing, structure, and defects [45,88]. Strong blue photoluminescence is observed for mpg-CN at room temperature. The maximum luminescence value is about 470 nm and its range is quite wide. Moreover, the photoluminescence spectrum differs by the degree of polymerization and the layered packing. The band structure of g-CN causes the usage of carbon nitrides as photoelectrochemical cells. Even bulk g-CN has a photocurrent when it is irradiated with light. The altering of the nanomorphology changes the electronic band structure [45]. Moreover, g-CN has a very characteristic and strong peak at 27.3° which indicates the interplanar stacking of aromatic units in the material [89]. Considering these properties of g-CN, it can be used as support material.

These are the explanation and characteristics of the mpg-CN. The all points which are important to understand the used catalysts for the project are explained so far. The applications of these catalysts were performed on transformation reactions of terpenes. Thus, the next section will involve terpenes.

1.6.Terpenes

Terpenes are available in nature greatly. Over 20,000 terpenes are identified in nature. Terpenes are the component of essential oils [90,91]. The building blocks of terpenes are isoprene unit (C_5H_8) and their structures can be cyclic such as p-cymene or linear such as β-myrcene as shown in Figure 1.12 [90,92]. They have a basic formula as $(C_5H_8)_n$, n indicates the number of isoprene units that are bound. Monoterpenes which are composed of 2 isoprene units are the simplest form of terpenes. Sesquiterpenes and diterpenes involve 3 and 4 isoprene units, respectively.

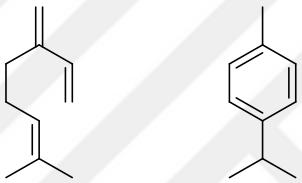

Figure 1.12: The structures of β-myrcene (left) and p-cymene (right).

Their production is supplied by different kinds of plants and by some animals. Terpenes can involve oxygen-containing functional groups such as aldehyde, ketone, carbonyl, and hydroxyl. These types of terpenes are named terpenoids. Terpenes exist in different plants and fruits and can be extracted. For example, limonene is found in citrus fruits; myrcene in daphne, mangos, and basil [93]; caryophyllene in black pepper; pinene in resin of pine tree; linalool in citrus and lavender [94]. In Figure 1.13, some kinds of terpenes are demonstrated.

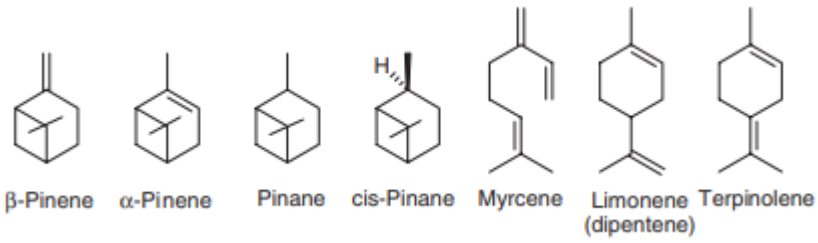

Figure 1.13: Different types of terpenes [95].

Terpenes have an important role in medicine and pharmacology. Terpenoids are used in the treatment of several diseases such as cancer and the protection of agricultural products. Moreover, terpenoids exhibit various properties such as anti-inflammatory, antimicrobial, antifungal, antiviral, and anti-allergenic. According to several research projects, monoterpenes can be useful in the prevention and treatment of cancer [90,96,97]. It is stated that D-limonene and perillyl alcohol have a significant role in chemopreventive and therapeutic properties to different types of human cancers. The improvement of some cancer cells such as mammary, fore-stomach, liver, lung, skin, colon, prostate, and pancreatic is constrained by these substances depending upon the applied dosage. It is proved that the monoterpenes possess some influence as antimicrobial and antifungal. The lipophilic character of monoterpenes leads to acting in an antimicrobial manner. Terpenes also act as an antifungal. It is stated in the research that carvone and perillaldehyde exhibit antifungal properties. Research with diverse kinds of microorganisms demonstrates that some isolated terpenes have an impact on antiviral activity. The properties of terpenes on diseases can be classified in this way [90].

Different kinds of reactions are available for terpenes. In respect of this thesis, dehydrogenation, hydrogenation, and aromatization reactions are conducted with several terpene molecules. Dehydrogenation reactions are based on the removal of hydrogen from the molecule. Dehydrogenation reactions of terpenes are very studied reactions. It is stated that the dehydrogenation of several terpenes such as limonene, terpinolene, carvone, and pinene was achieved in the presence of Pd and Pt catalysts by Listead, Michaelis, and Thomas [90,98]. Dehydrogenation of citral, geraniol, and menthol can be performed with liquid-metal catalysts to produce their aldehyde and ketones. Hydrogenation reactions can be considered anti-dehydrogenation. It is based on the addition of hydrogen in a molecule in the presence of a hydrogen donor substance. Catalytic hydrogenation of terpenes has been studied for a long time. Several published works demonstrated that high-pressure treatment and availability of different metal catalysts have achieved this type of reaction [99].

1.7. Motivation of the thesis

It is known that the concept of catalyst dates back centuries ago. Catalysts accelerates the rate of reactions via allowing them to proceed on a different pathway with a lower activation energy. Catalyst can be classified into 3 types: homogeneous, heterogeneous, and biocatalyst. Heterogeneous catalysts have prevailing properties against homogeneous

and biocatalysis. Reusability and high stability properties make it desirable in the industrial field. 2D semiconductors are a kind of nanomaterials in which a dimension of nanomaterial is nano-sized. To enhance the properties and to inhibit the fast recombination of 2D semiconductors, the preparation of heterojunctions is very useful. Owing to the superior characteristics of bimetallic nanoparticles, their applications are very common and studied. mpg-CN which is a kind of 2D material can be utilized as support material in the catalyst field. Due to its high surface area, suitable band gap, optical, electronic, and photoelectrochemical properties, it is a material which is developed for a long time. Terpenes have widespread studies because of their suitability in diverse areas especially medicine. Their catalytic transformation reactions can be achieved with a high yield. In the context of these all-covered sections, the topic of this thesis is constituted.

Chapter 2:
LITERATURE REVIEW

2.1. Palladium-based Bimetallic Alloys

Humphrey Davy provided the first awareness of a catalytic reaction between two gaseous reactants by observation in the experiments on the miner's safety lamp. Davy realized that a Pt wire was hot without a flame in the existence of air and coal-gas. He revealed that coal-gas and air reacted by contact with hot Pt surface without flame and just Pt and Pd wires could perform that [100]. The most considered catalysts are platinum-group metals (PGM) for approximately 200 years [101]. In industry, Pt was reported as the first utilized catalyst in the 19th century. The improvements in designing new platinum-group metals-based catalysts were maintained due to their prevailing properties such as high catalytic activity, selectivity, stability, and tolerance against poisoning [102]. Palladium as being classified among PGM has gained interest in research thanks to its broader abundance and Pt-liked catalytic properties [102]. Compared with the other metals among PGM, the electron configuration of Pd ($4d^{10}5s^{0}$) is exclusive and it is active for many reactions such as hydrogenation, dehydrogenation, oxidation, coupling reactions, hydrogenolysis, carbonylation, carbohydrate reforming, and hydrodesulfurization [103,104]. Nobel Prize in Chemistry in 2010 was presented to Suzuki, Heck, and Negishi because of their studies on Pd-catalyzed C-C coupling reactions [105,106]. Moreover, Pd catalysts have huge application areas in petroleum cracking, methane combustion, CO oxidation, alcohol oxidation, hydrogenation of unsaturated hydrocarbons, and dehydrogenation of alkanes [107–115]. Due to its wide application area and excellent properties, Pd catalysts take an important place in the industry [103]. In the context of sustainable chemistry, it is crucial to design heterogeneous Pd catalysts that contain less Pd while maintaining or improving catalytic performance. In this regard, due to their high surface-to-volume ratio and highly active surface atoms compared to those of bulk catalysts, the use of colloidal or supported Pd nanoparticles with a particle size smaller than 10 nm as a heterogeneous catalyst for various reactions, including organic transformations, has attracted considerable attention [116]. To enhance the catalytic performance of Pd NPs, bimetallic Pd alloys were generated; hence, the electronic and geometric structure of Pd NPs could be adjusted unlike monometallic Pd [104,117–119]. Intrinsic activity and selectivity of the available active sites which are affected by surface features of bimetallic Pd decide to catalytic performance [120–122]. The impacts to

regulate the surface features of bimetallic Pd NPs were listed as ligand, strain, and ensemble effects, as shown in Figure 2.1 [103,104,123].

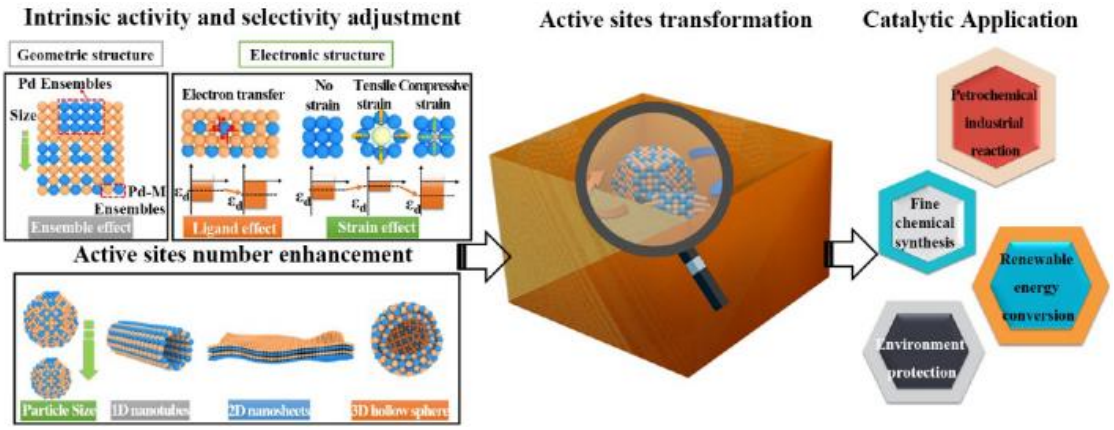

Figure 2.1: Schematic illustration of ligand effect, strain effect, and ensemble effect [103].

2.1.1. Control of Instrinctic Activity and Selectivity

2.1.1.1. Ligand Effect of Pd-based Bimetallic Catalysts

Electron withdrawing or electron donating from/to the other atoms concludes active sites with electron-rich or electron-deficient states which compose the electronic structure of active sites. Tuning these active sites is defined as the ligand effect. Adsorption features are specified by the influence of electron state on the d-band center of Pd and d-band filling controls the d-band position [124]. Pd has the ability to attain electrons from another metal due to the hybridization despite its d orbital being fully filled [103]. The classical d-band theory explains that d electron transfer from another metal leads to moving the d-band center away from the Fermi level which concludes weaker adsorption strength [103,125]. Adsorption strength has a significant role in intrinsic activity and selectivity.

Ligand effect in bimetallic Pd-based alloys:

In the alloy structures, electron transfer which results in the ligand effect occurs between the metals which are contributed to the alloy. It can be concluded that alloying with second metal brings adjusting the electronic structure of Pd [103]. Alloying of Pd with the metals whose higher electronegativity concludes the electron deficiency on Pd [126–128]. According to the reported results by Bai et al., the formation of alloy between Pd and Ir, with higher electronegativity than Pd, decreases the affinity of oxygen-containing species on Pd and it is observed that enhancing the capturing of OH* by reducing the

capturing of COO* causes to fast oxidation of CO_2 [95]. It is also stated by Hong et al., that the selectivity of Pd is increased by alloying with Ir over differing Pd/Ir ratios [128].

Combination of ligand effect and support effect:

Alongside the ligand effect, support material also influences the electronic and geometric structure of catalysts. Thus, intrinsic activity and selectivity could be enhanced by the combination of ligand and support effect [103]. The effect of this combination was explained by Wang et al. where CrPd alloy nanoparticles anchored on 3-aminopropyl triethoxysilane functionalized monochlortriazinyl β-cyclodextrin (M-β-CD). $Cr_{0.4}Pd_{0.6}$/M-β-CD was shown to be the best catalyst with TOF of 5771 mol H_2 mol $Pd^{1-}h^{-1}$ in the formic acid dehydrogenation for hydrogen production. The value was 15.3 times $Cr_{0.4}Pd_{0.6}$/C and 1.3 times Pd/ M-β-CD as shown in Figure 2.2. Alloying with Cr and the effect of support material which can donate its lone pairs on N increased the electron density and the catalytic activity of Pd [129].

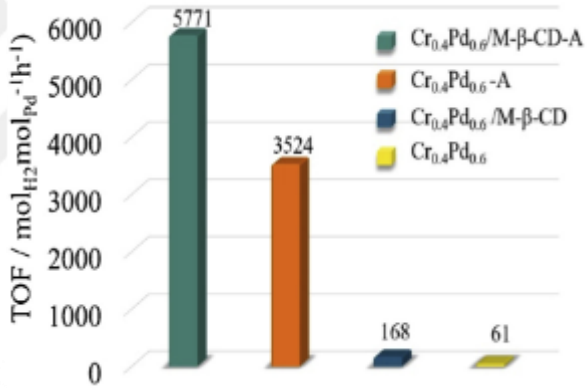

Figure 2.2: TOF values of the different CrPd catalyts in hydrogen production reaction via formic acid dehydrogenation [129].

2.1.1.2. Strain Effect on Pd-based Bimetallic Catalysts

The strain effect, which can be divided into two groups as tensile and compressive, is the second effect that adjusts the electronic structure of the active sites of the bimetallic nanocatalysts due to the lattice mismatch. The generation of tensile strain causes to shifting of the d-band center toward the Fermi level while compressive strain expands the d-band center of atoms [130].

Strain effect in bimetallic Pd-based alloys:

Strain and ligand effects have a crucial role in tuning the electronic structure of alloys. Hence, the contribution of both effects is not easily understood. According to the reports by Peng et al., the contribution of the strain effect predominates superior. It is expected the down-shift of the d-band center of Pd due to the ligand effect. On the contrary, the upshift d-band center which originates from different lattice parameters for Ag, Pd as 4.060 Å and 3.887 Å, respectively, should be observed because of the tensile strain for Pd. DFT calculations showed the upshifting of the d-band center with the enhancement of Ag/Pd ratio. It was concluded that the strain effect overcomes the ligand effect [131]. Moreover, Wu et al. stated that the catalysts which are prepared in two different phases as body-centered cubic (bcc) and face-centered cubic (fcc) show diverse catalytic performance in the oxygen reduction reaction. The lattice of the fcc phase of PdCu alloys is analyzed as 3.80 Å while the lattice of the bcc phase is 2.97 Å. The greater lattice parameter for the fcc structure causes more electron transfer to the O_2 molecule [132]. The strain effect on intrinsic activity is summarized in part.

2.1.1.3. Ensemble Effect of Pd-based Bimetallic Catalysts

Catalytic activity is affected by the ensemble effect which causes diverse atomic arrangements. It changes the adsorption configuration and strength of the species in the reaction. Two distinct types of active sites, segregated Pd ensemble sites and PdM sites, might be included in alloys or core-shell structures depending on the local atomic arrangements. The coordination number and size of the segregated clusters, the composition or ratio of Pd/M, and other organizational aspects of these sites can all be altered to achieve optimization [103].

2.1.1.3.1. Sites for segregated Pd ensemble

The term "segregated Pd ensemble sites" relates directly to Pd-based bimetallic catalysts in which Pd is the primary active site and the other component simply serves as a diluent for Pd. Segregated Pd ensembles can vary in size from a bigger cluster to a monomer, which has a variety of effects on various processes [103]. Han et al. examined the impact of Pd ensemble size on the PdAu (111) model catalyst's ability to selectively oxidize acetaldehyde to acetic acid. The bigger Pd ensembles encouraged the dissociation activation of O_2, which increased activity by enlarging Pd ensemble sites in a specific region while maintaining acceptable selectivity [133]. According to research by Lee et al.

on the ensemble impact of AuPd model catalysts for formic acid dehydrogenation, Pd trimer ensembles (3-fold hollow sites linked to three Pd atoms) demonstrated the lowest reaction barrier when compared to Pd monomer and dimer ensembles [134].

2.1.1.3.2. Bifunctional PdM sites

The Pd-M sites specifically relate to Pd-based bimetallic catalysts in which both Pd and M function as catalysts for the process. Typically, Pd and M are required to coactivate the reactant molecule, or Pd activates one reactant molecule while M activates another, or M performs additional tasks to help Pd. Regulating the Pd/M ratio for the PdM sites may affect the intermediate's adsorption configuration and performance [103]. For the selective activation of the C-O bond and the H_2 dissociation, Guo et al. used Ru and Pd, respectively. $RuPd_5/NH_2SiO_2$ performed better than high TOF (172 h^{-1}) and CO cleavage selectivity of 99% when the cooperative impact of PdRu sites was enhanced by adjusting the Pd/Ru ratio [135].

In brief, different effects such as ligand, strain, and ensemble on Pd-based alloys were expressed in this section.

As stated previously, Pd-based bimetallic alloys can be utilized as catalysts in different reactions. In the following part, some of these reactions will be explained.

2.1.2. Pd-based Bimetallic Alloys as Catalysts in Several Reactions

Herein, some studies on different reactions catalyzed by PdM alloy nanoparticles will be discussed in this part.

2.1.2.1. Hydrogenation Reactions

Hydrogenation is the name of a reaction comprising the addition of hydrogen to the unsaturated bonds [136]. In the industry, catalytic hydrogenation has an important role. The ability of dissociation of H_2 into atomic H by Pd is remarkable due to the suitable strength of Pd–H bond. Thus, Pd-based catalysts are extensively used in this kind of reaction [104]. Figure 2.3 demonstrates the H_2 activation ability corresponded to M–H bond energy, M represents metal, in the volcano relationship. According to the plot, the capacity of Pd is seen at the top to catalyze the hydrogenation reactions [137].

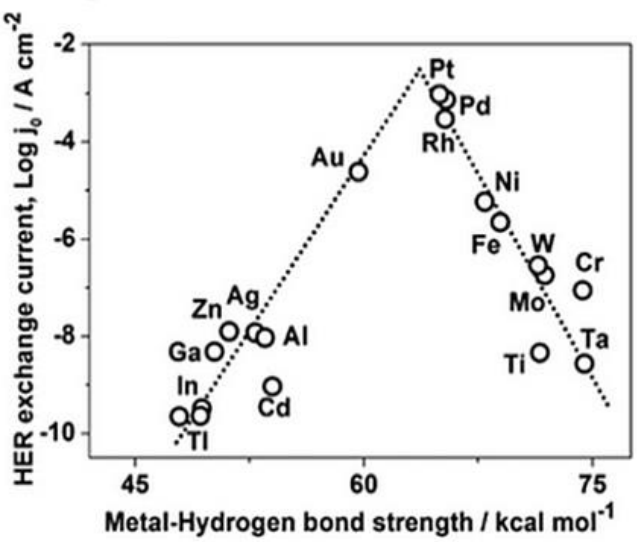

Figure 2.3: Volcano relationship of H_2 activation and metal-hydrogen bond strength [137].

Conversion of benzene to cyclohexane via hydrogenation is a crucial process for industry. The activity order of some transition metals for hydrogenation of benzene is as follows: Co<Pd<Ni<Pt<Ru in the context of interaction between substrates and metal NPs [138–142]. Yoon et al. indicated that Pd did not perform any activity for the formation of cyclohexane from benzene due to the weaker adsorption of benzene while Rh/CNT (carbon nanotube) had strong catalytic activity for hydrogenation of benzene at room temperature [143]. In the case of alloying of Pd with Rh, activity enhanced nearly twice that of the monometallic Rh catalyst. Due to the unique electronic structure of alloy, benzene and hydrogen activated successfully to yield cyclohexane.

Selectivity of hydrogenation for substrates with multi-unsaturated bonds can be a problem because of the multi-hydrogenation pathway. For instance, the hydrogenation of acetylene to ethylene is one of the most desirable reactions for the industry due to the extensive usage of ethylene for polymer synthesis [104]. It is known that supported monometallic Pd catalyst has a selectivity problem in the context of this reaction since a large Pd surface causes the formation of ethylene hydride which can be converted to ethane [144–146]. As stated by Choudhary et al., an alloy formed between Pd and Au enhances the conversion of acetylene to ethylene, shown in Figure 2.4 [147].

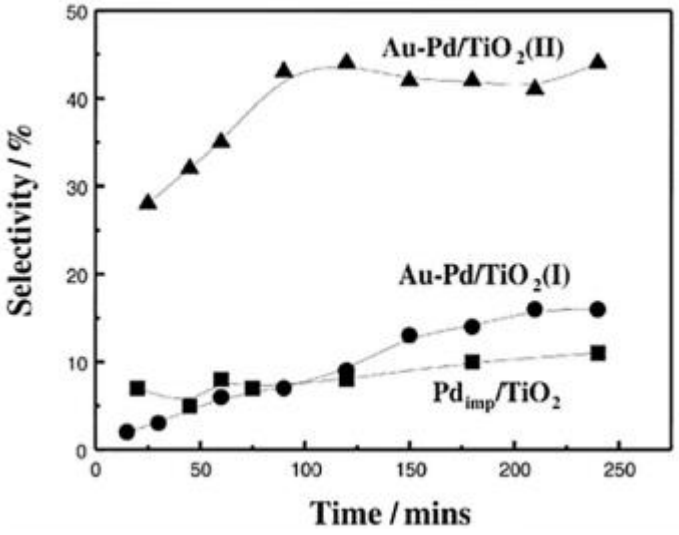

Figure 2.4: Ethylene selectivity in hydrogenation of acetylene for Pd alloys with Au (Au/Pd ratio is for (I) 2.0 and (II) 2.2) [147].

Within the scope of the industrial scale of hydrogen production from renewable sources, CO_2 conversion to methanol is very attractive [148–151]. The most common catalyst is Cu/ZnO for hydrogenation of CO_2 [152,153]. Haller et al. and Fierro et al. stated that the inclusion of Pd into Cu/ZnO catalyst increased methanol production due to the synergistic effect of Pd and Cu metals [154,155]. Owing to the exceptional ability of Pd to activate hydrogen molecules, Pd-based catalysts are expected to boost methanol production via the hydrogenation of CO_2. As explained by Bonivardi et al., when Ga_2O_3 was added to Pd/SiO_2 catalyst, its activity was strengthened 500-fold that of the monometallic Pd/SiO_2 due to the interaction between Ga and Pd [156]. Because of the empty 5s orbital of Pd, it accepts the electrons from late transition metals such as In, Zn, and Ga with s-valence electrons. Thus, the enhanced electron density of the surface of Pd-based alloy causes to increase in the interactions with intermediates and further hydrogenation of CO_2 occurs [104].

2.1.2.2. Dehydrogenation Reactions

Dehydrogenation reaction is the extraction of hydrogen from the structure to yield the unsaturated molecule [157]. As hydrogenation reaction, Pd-based catalysts can achieve to dehydrogenate process. The in-situ production of H_2 in polymer electrolyte membranes is one of the most desirable dehydrogenation reactions. The conversion of formic acid to CO_2 and H_2 is an example of this kind of reaction. Formic acid which is used as hydrogen storage material is commonly used to provide hydrogen to fuel cells because of its

superior properties such as high energy capacity [158–160]. According to the previous reports, dehydrogenation of formic acid can be fulfilled at 100 °C in the presence of Pd catalyst [160–162]. The formation of side products (CO and H_2O) can be also observed during the dehydrogenation of formic acid [163]. As reported by Gu et al., the high activity of monometallic Pd was observed for dehydrogenation of formic acid, yet CO production causes catalyst poisoning and loss the catalytic activity [164]. Then, it was realized that AuPd alloy demonstrated the highest activity for the dehydrogenation of formic acid without deactivation of the catalyst. This result originated from the high CO tolerance of Au. Also, Zhang et al. stated that $Ag_{42}Pd_{58}$ NPs exhibited the best catalytic activity in the context of dehydrogenation [165]. According to the results of Kim and Barteau and Hoshi et al., different adsorption states led to the formation of divergent products such as CO_2 and CO during the decomposition process of formate. As shown in Figure 2.5, the formation of CO_2 occurred with adsorbed bidentate while adsorbed monodentate produced CO [166,167]. Adsorbed bidentate provided the dehydrogenation pathway by improvement of back donation from catalyst surface to the formate species.

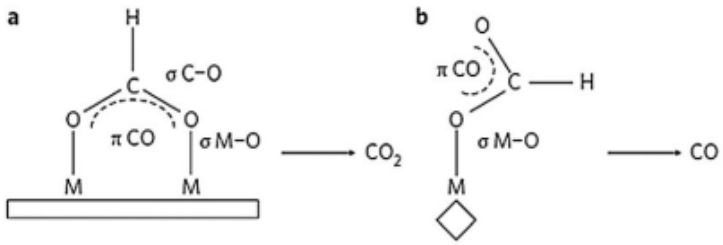

Figure 2.5: Interactions of formate with (a) adsorbed bidentate and (b) adsorbed monodentate [166,167].

As a result, alloy formation between Pd and different metals affects its selectivity and activity in the dehydrogenation reaction. In this thesis, Pd-based alloy nanoparticles were generated on the support material which is mesoporous graphitic carbon nitride. Thus, the examples in the literature mesoporous graphitic carbon nitride as a supporting material will be expressed in the following part.

2.2. Mesoporous Graphitic Carbon Nitride Synthesis Strategies as Support material

The abovementioned properties of mpg-CN are superior to other g-CN derivatives whereas they are used as supporting materials. For this purpose, to control the size, morphology, and porous structure, inorganic or organic materials are used as the template.

In the template-assisted strategy, there are 3 steps: the first step is based upon the template synthesis, the second one is the preparation of desired materials in the presence of these templates, and the last step is the removal of the templates [168,169]. This convenient synthetic methodology was chosen for the synthesis of support material that was used in the thesis.

In order to expedite the electron-hole separation and increase the catalytic performance of the mpg-CN, hybridizing is one of the common methods [170]. It is important to examine the enhanced performances of mpg-CN because of the synergistic impact between mpg-CN and other hybrid components. There are several methods to construct a hybrid for mpg-CN; however, only metal nanoparticles/mpg-CN will be covered in this part.

Metal Nanoparticles/mpg-CN;

mpg-CN has specific functional groups and mesopores that take charge of the stabilization of metal nanoparticles causes to enhance their performance and stability [171]. There are 4 synthetic methods which are generally used to involve the metal nanoparticles in the mpg-CN to control the size and distribution.

(i) *Wet-chemical impregnation strategy:* This method is based on the addition of porous support in a solution that includes the metal precursors. Inorganic metal salts such as metal sulfates, carbonates, chlorides, nitrates, or acetates, as well as organic metal complexes like metal acetylacetonates, are examples of common precursors [172]. The reduction process with a suitable reducing agent follows the first step. Thus, metal nanoparticles can be yielded inside and on the surface of mpg-CN [173]. Due to the high solubility of many precursors, water is the most often utilized solvent for inorganic salts, whereas organic solvents are mostly employed for precursors of organometallic compounds. Concentrations below (super)saturation are required to prevent the early deposition of the metal precursor in bulk solution [172].

(ii) *Photochemical deposition technique:* In this special strategy for semiconductors, metal nanoparticles yield on specific active sites of mpg-CN. Photogenerated electrons on various sites of the mpg-CN semiconductor may be used to selectively deposit metal nanoparticles on particular active sites. It is common practice to incorporate photogenerated hole scavengers (such as triethylamine, diisopropylethylamine, methanol, and so on) to neutralize positive charges, which can significantly speed up the creation of

metal nanoparticles. Typically, the metal anions were initially deposited onto the mpg-CN semiconductor by reducing photogenerated electrons under the influence of ultraviolet or visible light after the mpg-CN was first dispersed in a metal precursor solution. The approach used in this procedure is unique for semiconducting materials [174].

(iii) *Precipitation-reduction approach:* Precipitation of metal precursor in the inner and outer of the mpg-CN occurs in convenient reaction conditions. Supported catalysts have long been produced by precipitation, which may be caused by a change in circumstances like temperature, pH, or evaporation. The principles of nucleation and growth are applied in controlled precipitation from a precursor solution. Small and fairly monodisperse particles can be produced by an initial nucleation boom of tiny crystallites followed by development without the production of additional nuclei [172]. After the reduction process, metal nanoparticles formed onto mpg-CN support [175–177].

(iv) *Ion-exchange reduction method:* Firstly, an ion exchange typically took place on a charged mpg-CN, followed by the reduction of metal ions to nanoparticles by the proper reducing agent [178].

Among these methodologies, the wet-impregnation strategy was chosen for the synthesis of bimetallic alloys on support in this thesis. As-synthesized catalysts will be applied to organic transformations such as dehydrogenation, hydrogenation, and oxidation of terpenes. Thus, the next section will cover the terpenes and their reactions.

2.3. Terpenes

Terpenes are important components of plants, especially seeds and fruits. They are used as aroma and fragrance [179] Moreover, they can be utilized as sustainable raw materials in the industry to substitute petrol-based sources for the synthesis of hydrocarbons. In the view of continuous rise in oil prices, the usage of terpenes which are isolated natural chemicals is the economical and effective way to the production of value-added products that are synthesized by the oil industry [180]. For instance, there are abundant, natural, and low-cost terpenes such as limonene and pinene to use for the synthesis of value-added materials which will utilize as fragrance, pharmaceutics, solvent, and chiral intermediates [181]. Besides the economy, the Kyoto Protocol and the desire to decrease the dependence on imported raw petrol cause to utilize the biomass as an energy source and fuel [182]. In this sense, terpenes can be used as raw materials for the synthesis of value-added

products. Thus, the functional groups in the biomass can be benefited for the production of new products with improved properties or change in the available chemicals. In this context, various chemical processes such as isomerization/rearrangement, oxidation, carbonilation, and (de)hydrogenation were developed to synthesize desired products from terpenes [183–186].

2.3.1. Dehydrogenation of Terpenes

There are a few studies on catalytic dehydrogenation reactions of terpenes under green and sustainable solvent conditions [187]. Conversion of commercially available and low-cost compounds such as limonene to more valuable p-cymene is an important example in the context of this kind of reaction and it is illustrated in Figure 2.6. Tegge stated that the economical production of p-cymene provided benefits for various new products [188]. Moreover, p-cymene could be synthesized by Friedel-Crafts alkylation in the presence of toluene and 2-propanol [189]. The usage of the huge amount of dangerous acid catalysts leads to several problems such as transportation, safety, removal of pollutants, and corrosion. For example, alkylation reactions are usually conducted at high temperatures (200-450 °C) and several side products are formed; hence, the yield of p-cymene is generally limited to 50% [190]. The alternative pathway to produce p-cymene from natural terpenes is provided with high selectivity. Several reports exist about the aromatization of terpenes such as limonene, α–pinene, and industrial diterpenes in literature. It was reported the dehydrogenation of limonene or α–terpinene under mild reaction conditions in the presence of oxidants such as $KMnO_4/Al_2O_3$, chloranil, and *N*–lithioethylenediamine [191,192]. Furthermore, many of the studies demonstrated that the high temperature (250-550 °C) gas phase procedures included noble (especially Pd) or alkali metals, molecular sieves that involve Al, Zn, Fe, Cr, Ni, and Mn, ion-exchange clays, zeolites as catalyst [193–197].

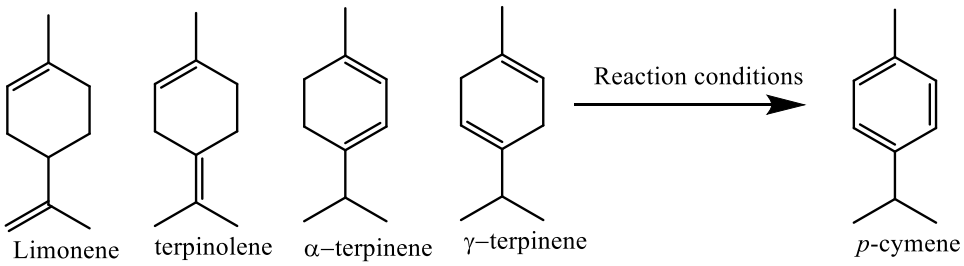

Figure 2.6: Catalytic dehydrogenation of natural terpenes to p-cymene.

2.3.2. Hydrogenation of Terpenes

In 1912, Ipat'ev reported the hydrogenation of terpenes which was another method to convert terpenes into value-added products for the first time, and this reaction was applied for several industrial objectives, prevalently [198]. Therefore, the selective hydrogenation of monoterpenes that has industrial applications of selective hydrogenation of limonene to precious products attracted intensive attention, and it is shown in Figure 2.7 [199].

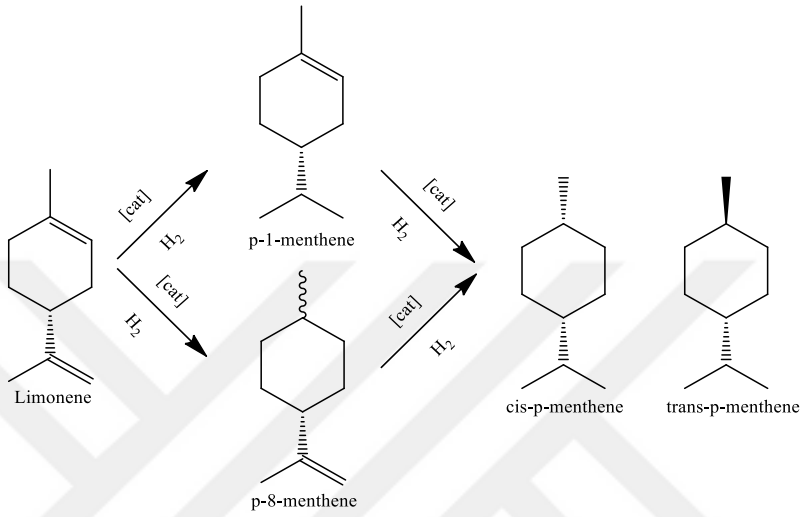

Figure 2.7: Reaction pathway for hydrogenation of limonene.

The formation of (+)–p–1–menthene which was a hydrogenation product of limonene was the attractive intermediate due to absorption of the chiral center and the existence of a double bond that can be functionalized. In order to synthesize the bulk chemicals (e.g., adhesives, coatings, additives agents for nourishment) and fine chemicals (e.g. steroids, antimalaria agent, menthol), (+)–p–1–menthene was utilized as starting material, widely [200]. Besides, hydrogenated products which were derivatized from (+)–p–1–menthene and p–menthane were indicated as biobased fuel additives [201]. In spite of the fact that hydrogenation of limonene in the existence of homogeneous catalysts was comprehensively studied, the catalyst recovery problem was an obstacle to practical applications. On the other hand, the application of this aforementioned reaction was reported in the presence of heterogeneous catalysts (Pt, Pd, Ni, Cu, Rh, Ru) with various supports [202–206]. Some monometallic nanoparticles with support materials were tested on selective hydrogenation of limonene [207]. However, these reactions have harsh conditions such as high temperature and H_2 pressure for catalytic hydrogenation. Due to the expensive special equipment and the safety problems for high H_2 pressure, certain problems with the recycling of H_2 consisted [208]. In recent days, Metin et al. improved

an easy transfer hydrogenation procedure which is conducted in the glass-pressure tube to reduce the unsaturated bonds (e.g. -NO_2, -CN, -C=O, -C=C-, etc.) in the presence of ammonia-borane as a hydrogen source in methanol [209,210]. In this procedure, the usage of a high-pressure hydrogen tank and expensive equipment is not required. Moreover, this procedure shows selectivity for reduction of the -NO_2 group in the presence of the second reducible functional groups such as -CN, -C=O.

2.3.3. Oxidation of Terpenes

The previous works demonstrated that toxic chromium or selenium-based reagents were used as the catalyst for the oxidation of terpenic olefins [211]. Thus, many sustainable pathways have been improved to convert into α,β–unsaturated ketones. Different types of heterogeneous catalysts were used in the oxidation of terpenes. In this part, cobalt-based catalysts will be covered. Molecular cobalt complexes, e.g. $Co(NO_3)_2$ or $Co(4–MeC_5H_3N)_2Br_2$, were utilized for the oxidation of α–pinene with high selectivity [212–214]. Gusevskaya et al. stated that mild oxidation of terpenes was performed with molecular oxygen in the presence of cobalt- and manganese-based ferrites. It was realized that the cobalt-based ferrites showed higher activity with higher TONs than manganese-based ferrites. The conversion of β–pinene with cobalt-containing ferrites as catalyst was achieved with high selectivity [215]. In 2007, Kholdeeva reported that the decoration of cobalt-containing polyoxometalate on hydrothermally stable silicates by means of electrostatic binding of CoPOM and amino-modified support. Oxidation products such as verbenone and verbenol were obtained with selectivities up to 70% [216]. In other work, cobalt-substituted MCM-41 catalysts were constructed via a combination of cobalt species and support material. It was observed that oxidation of isolongifolene yielded ketone with great selectivity in the presence of the aforementioned catalyst in the solventless medium under mild and aerobic conditions, as shown in Figure 2.8 [217].

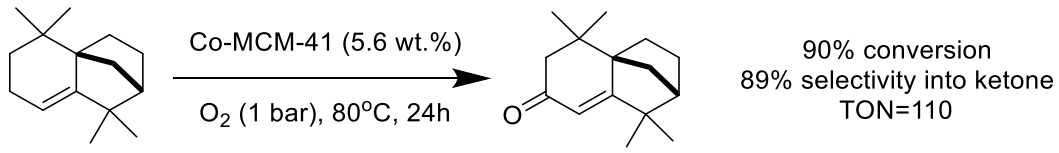

Figure 2.8: Oxidation of isolongifolene in the presence of Co-MCM41 [216].

It can be concluded that cobalt-containing catalysts can be effectively utilized for the oxidation of terpenes. Thus, Co-based bimetallic alloys can show high catalytic activity and selectivity because of the synergistic effect of different metals

Chapter 3:
MATERIALS & METHODS

In this chapter, materials, and methods which were utilized for the synthesis of mpg-CN, CoPd/mpg-CN nanocatalysts, and the catalytic transformation of terpenes were explained in detail. Moreover, the characterization of the synthesized materials was performed using advanced techniques.

3.1. Materials

LUDOX HS-40 colloidal silica 40% water suspension (98%), ammonium hydrogen difluoride (NH_4HF_2, 95%), cobalt(II) nitrate ($Co(NO_3)_2.6H_2O$, 98%), cobalt(II) chloride ($CoCl_2$, 98%), bis(acetylacetonate) cobalt(II) ($Co(acac)_2$, 97%), palladium(II) acetate ($Pd(OAc)_2$, 46.6-49%), palladium(II) acetylacetonate ($Pd(acac)_2$, 99%), dimetylcarbamil chloride (98%), sodium hydride (NaH, 98%), pyridine (≥99%) , etil chloroformate (97%), tetrakistriphenylphosphine palladium ($Pd(PPh_3)_4$, 99%), trimethylsilyl ciyanide (TMSCN, 98%), ammonia-borane (NH_3BH_3, 90%), tert-buthyl hydroperoxide (TBHP, in 5.0-6.0 M decane) were purchased from Sigma-Aldrich. Sodium borohydride ($NaBH_4$, ≥98%) were received from Merck. Guanidine hydrochloride ($CH_5N_3.HCl$, 98%), cobalt(II) acetate ($Co(OAc)_2.4H_2O$, 98%), potasiumtetrachloropalladate (K_2PdCl_4, 99.9%, 32.2% Pd content) were obtained from Alfa Aesar. Palladium(II) bromide (39.8-40.1% Pd) was bought from Acros Organics. Hydrogen peroxide (H_2O_2, 35%), *N*,*N*-dimethylformamide (DMF, ≥99.0), dichloromethane (DCM, ≥99.0) were received from Isolab chemicals. Hydrochloric acid (HCl, 37%) was purchased from Tekkim.

3.2. Synthesis of Mesoporous Graphitic Carbon Nitride (mpg-CN)

Mesoporous graphitic carbon nitride was synthesized by the polycondensation method at high temperature as a common method in the literature as shown in Figure 3.1 [218]. First of all, 4.0 g guanidine hydrochloride was dissolved in 4 mL water and added to 10 g of a solution of LUDOX HS-40 colloidal silica as a template which was weighted in a 100 mL round-bottom flask. The mixture was allowed to stir overnight at 50 °C. After the cooling process to room temperature, the as-prepared white material was crushed in ceramic mortar to obtain the powder. The resultant powder was transferred into a quartz crucible with a lid to place in a horizontal quartz tube oven for the annealing process. The oven was heated to 550 °C with a ramp rate of 4-5 °C per minute under Ar gas flow for 2 hours and it was kept at this temperature for 2 hours. At the end of this process, the

acquired pale yellow powder solid was reacted with 4 M, 200 mL of ammonium hydrogen difluoride for 48 hours to remove the remained silica template. Then, the yielded powder solid material was washed 3 times with water, and once with ethanol using a centrifuge at 7500 rpm for 10 minutes to remove residuals. Finally, it was dried with the help of a vacuum oven and kept for further use.

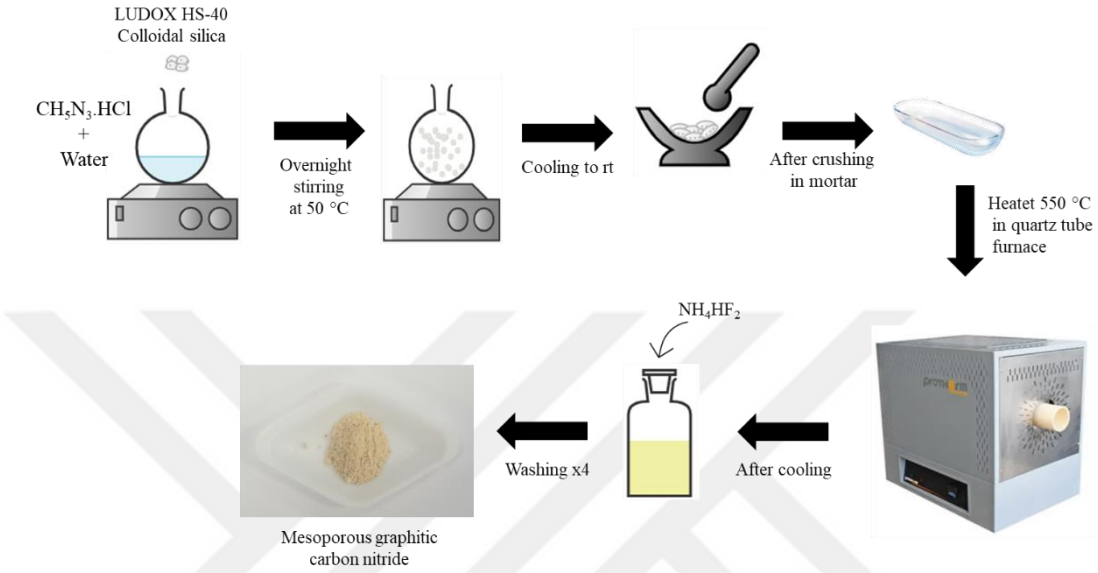

Figure 3.1: Synthesis scheme for mesoporous graphitic carbon nitride.

3.3. Synthesis of Cobalt Palladium Alloy Nanoparticles on mpg-CN (CoPd/mpg-CN)

CoPd alloy nanoparticles on support material which was mpg-CN were synthesized by using a colloidal synthesis method. The synthesis of these nanocatalysts was carried out in a specially designed four-necked glass reactor under an inert gas atmosphere (Argon) with a thermocouple to control the temperature. The setup can be seen in Figure 3.2. The decision of the optimum synthesis conditions for CoPd/mpg-CN nanoparticles was essential, thus; different metal precursors for Co and Pd which were mentioned in the part 3.1 were utilized in diverse ratios. The following synthesis method was repeated for all precursors. Firstly, 50 mg of mpg-CN was dispersed in 18 mL DMF for 2 hours by an ultrasonic bath. After that, 0.1 mmol of $Co(OAc)_2$ and 0.1 mmol of $Pd(acac)_2$ were added into the mpg-CN dispersion and the resultant mixture was sonicated for 1 hour. Then, the obtained mixture was transferred into the four-necked glass reactor and it was stirred vigorously for 15 minutes under inert (Argon) gas atmosphere. After that, the reaction temperature was set to 110 °C. When the reaction reached that temperature, the 2 mmol of borane *tert*-butylamine (BTB) mixture in 2 mL DMF was injected into the reaction medium and it was stirred under argon atmosphere for 1 hour. It was obtained that the

color of the mixture turned from yellow to brown after the addition of BTB in the reaction mixture and it showed the starting of the nanoparticle formation. After 1 hour at that temperature, the reaction was removed from the heating source and it was cooled down to room temperature. The cooled mixture was washed two times with the addition of ethyl alcohol with help of a centrifuge at 7000 rpm for 12 minutes. The obtained catalyst was dried *in-vacuo* and stored for further use.

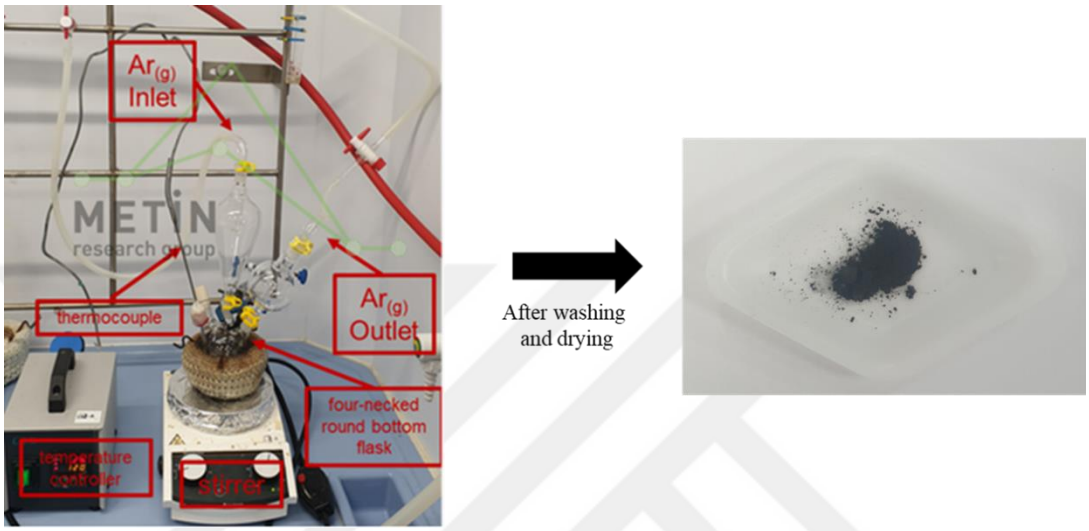

Figure 3.2: Reaction setup for synthesis of CoPd/mpg-CN.

3.4. Instrumentation

The powder X-ray patterns (XRD) were recorded on a D2 Phaser Bruker with an X-ray source of CuKα radiation (λ = 1.5418 Å), 30 kV, 10 mA by step scanning with a step size of 0.02°, the interval of 1 second per step in the range of 2θ = 10-80°, to identify crystalline phases present. Thermo K-Alpha X-ray photoelectron spectrometer (XPS) equipped with Al−Kα source was employed to analyze the surface chemistry of the prepared materials. All transmission electron microscope (TEM) images were recorded on a HT7800 TEM instrument that is equipped with dual-mode objective lens for HR-TEM analysis, scanning TEM (STEM) and energy dispersive X-ray operated at 120 kV. Inductively Coupled Plasma-Mass Spectrometer analyses were performed on an Agilent 7700x (ICP-MS). For the ICP-MS analysis, the powder samples were digested in 10 mL aqua regia (8.0 mL HNO_3 + 2.0 mL HCl) via Start D Milestone Microwave Digestion system and diluted with 2 v/v % HNO_3 blank solution. Photoluminescence spectroscopy (PL) measurement was conducted with an Agilent Cary Eclipse PL using an excitation source of 350 nm. Time-resolved spectroscopy (FSL) measurements were carried out with Edinburgh Instruments FLS1000 Spectrometer using a 377 nm laser source. The

Brunauer-Emmett-Teller (BET) surface area and pore size analysis were measured by using a Micromeritics ASAP 2020 using nitrogen adsorption–desorption isotherms. The absorption data was recorded using diffuse reflectance ultraviolet–visible-near infrared spectrometry (DRS, UV-VIS-NIR) via Shimatzu UV-3600 UV-VIS-NIR spectrophotometer. NMR spectra were operated at 500 MHz for ^{1}H NMR and recorded on Varian in $CDCl_3$ with tetramethylsilane (TMS) as the internal standard. Coupling constants (*J* values) were given in Hz and chemical shifts were indicated as parts per million (ppm). Splitting patterns were shown as s (singlet), br s (broad singlet), d (doublet), t (triplet), q (quartet), and m (multiplet). GC-MS spectra were recorded on an Agilent Technologies 7890B GC-system with an Agilent 5977 A MSD HP-5 column (0.25 mm × 30 m, film: 0.25 μm).

3.5. Catalytic Activity Studies

The catalytic activity of as-synthesized nanocatalysts was studied for the transformation reactions of terpenes such as dehydrogenation, hydrogenation, and oxidation reactions.

3.5.1. General Procedure for Dehydrogenation Reactions of Different Terpenes in the presence of CoPd/mpg-CN as Catalyst

All optimization and substrate scope studies for dehydrogenation reactions were conducted in a glass thermolysis tube with a lid. To determine the optimized conditions, a specific amount of catalyst was weighed and put in a glass thermolysis tube. 1 mmol of the corresponding substrate was added to the tube and it was stirred at a determined temperature for a significant time. The catalyst amount, reaction temperature, and reaction time were determined by optimization reactions. Reaction time and temperature differed for some substrates. At the end of the reaction, the catalyst was removed from the reaction media and the crude mixture was analyzed by NMR spectroscopy.

3.5.2. General Procedure for Hydrogenation Reactions of Different Terpenes in the presence of CoPd/mpg-CN as Catalyst

In the presence of as-synthesized CoPd/mpg-CN nanocatalysts, perillyl alcohol was selected as a model substrate for optimization reactions. The reactions were conducted in a glass thermolysis tube with a lid. Firstly, the determined amount of catalyst was weighed and transferred to the thermolysis tube, and a significant amount of methanol was added to it. The catalyst was dispersed by ultrasonic bath for 10 minutes. Then, a specific amount of perillyl alcohol was added and dispersed for 5 more minutes. After the ending

of the sonication process, 3 eq. of ammonia borane (NH_3-BH_3) was added to the mixture and stirred for a while at room temperature. When the reaction was finished, the catalyst was removed from the reaction by syringe filter, and the obtained compound was detected by GC-MS. The same procedure was applied to 10 different substrates. These substrates also were synthesized. The synthetic procedure of them were mentioned below.

3.5.2.1. Synthesis of substrates for hydrogenation trials of catalyst

3.5.2.1.1. Synthesis of perillyl alcohol (1) and carveol (2)

*Synthesis of perillyl alcohol **1***

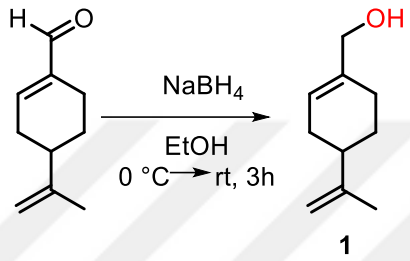

Scheme 3.1: Synthesis of perillyl alcohol from perillyl aldehyde

The desired amount of perillyl aldehyde was dissolved in ethyl alcohol in a round-bottom flask. It was placed in an ice bath. 1.2 eq. $NaBH_4$ was added to the reaction mixture. After the dissolution of $NaBH_4$ in reaction media, it was stirred at room temperature for 3 hours. At the end of the reaction, the solution was washed with DCM and water. The organic phase was dried over Na_2SO_4, filtered, and concentrated under reduced pressure. Compound **1** was used without further purification. **^{1}H NMR** (500 MHz, $CDCl_3$) δ: 5.61 (s, 1H), 4.64 (d, J = 6.0 Hz, 2H), 3.91 (d, J = 15.2 Hz, 2H), 2.42 (s, 1H), 2.05 (m, 4H), 1.82 (m, 2H), 1.66 (s, 3H), 1.40 (m, 1H).

*Synthesis of carveol **2***

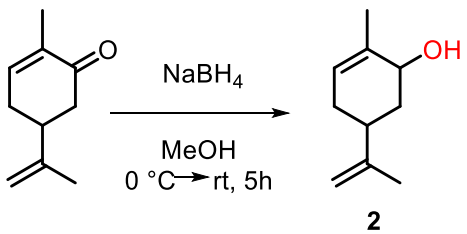

Scheme 3.2: Synthesis of carveol from carvone

The determined amount of carvone was put in the round-bottom flask and methanol was added to it. Flask was placed in an ice bath. After that, 1.1 eq. $NaBH_4$ was added to the

reaction mixture, and it was dissolved in methanol at 0 °C. The reaction was stirred at room temperature for 5 hours. The reaction solution was washed with DCM and water. The organic layer was dried over with Na_2SO_4, filtered, and concentrated under pressure. Compound **2** was used without further purification. **^{1}H NMR** (500 MHz, $CDCl_3$) δ: 5.45 (s, 1H), 4.69 (d, *J* = 0.8 Hz, 2H), 4.14 (s, 1H), 2.26–2.20 (m, 1H), 2.13–2.10 (m, 1H), 2.03 (d, *J* = 15.7 Hz, 1H), 1.93–1.88 (m, 1H), 1.71 (d, *J* = 10.1 Hz, 6H), 1.50–1.43 (m, 1H).

3.5.2.1.2. Synthesis of allylic acetates

*Synthesis of allylic acetate **3***

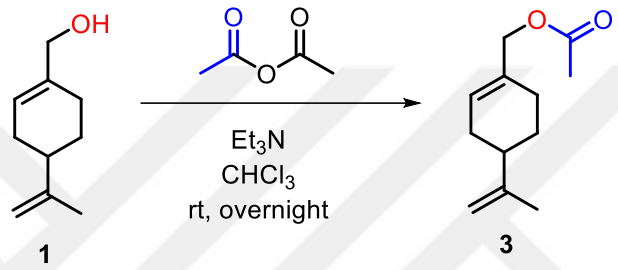

Scheme 3.3: The synthesis of allylic acetate from perillyl alcohol

The determined amount of perillyl alcohol (**1**) was dissolved in chloroform. The addition of 3 eq. acetic anhydride and 2 eq. triethylamine was followed as the next step and stirring at room temperature overnight was performed. The mixture was extracted with DCM and water. The organic phase was dried over with Na_2SO_4. It was filtered and the solvent was removed from the media. Compound **3** was detected by NMR. **^{1}H NMR** (500 MHz, CDCl3) δ: 5.72 (s, 1H), 4.68 (d, *J* =7.7 Hz, 2H), 4.42 (br s, 2H), 2.13 (d, *J* = 11.7 Hz, 2H), 2.03 (br s, 5H), 1.96–1.90 (m, 1H), 1.82–1.80 (m, 1H), 1.45 (s, 3H).

*Synthesis of allylic acetate **4***

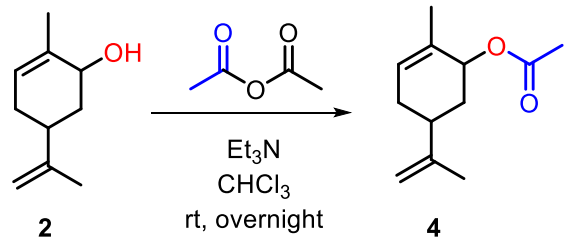

Scheme 3.4: The synthesis of allylic acetate from carveol

The determined amount of carveol (**2**) was put in a tube and chloroform was added as a solvent to it. 4 eq. acetic anhydride and 4 eq. triethylamine were added to the reaction

mixture, and it was allowed to stir at room temperature overnight. After extraction with DCM and water, the organic layer was dried over with Na_2SO_4, filtered, and the solvent was removed. Compound **4** was obtained and prepared for NMR analysis. **^{1}H NMR** (500 MHz, $CDCl_3$) δ: 5.46 (s, 1H), 4.69 (br s, 2H), 4.15 (m, 1H), 2.29–2.20 (m, 1H), 2.14–2.10 (m, 1H), 2.05 (s, 3H), 1.95–1.89 (m, 1H), 1.72 (s, 3H), 1.70 (s, 3H), 1.60 (s, 1H), 1.50–1.43 (m, 1H).

3.5.2.1.3. Synthesis of allylic carbonates

*Synthesis of allylic carbonate **5***

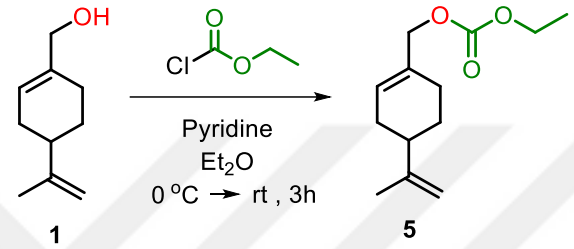

Scheme 3.5: The synthesis of allylic carbonate from perillyl alcohol

Compound **1** and dry diethyl ether were added to a 10 mL of a round-bottom flask. After dissolving the starting material, 4 eq. pyridine and 4 eq. ethyl chloroformate were added to the resulting mixture at 0 °C and stirred for 15 minutes. Then, the reaction mixture was stirred for 3 hours at room temperature. After that, its extraction was performed with ether and water. The organic layer was dried with Na_2SO_4 and filtered. After removing the solvent from the reaction media *in vacuo*, compound **5** was prepared for NMR analysis. **^{1}H NMR** (500 MHz, $CDCl_3$) δ: 5.72 (br s, 1H), 4.64 (d, J =9.0 Hz, 2H), 4.43 (m, 2H), 4.11 (q, J = 7.1 Hz, 2H), 2.12–2.01 (m, 4H), 1.93–1.86 (m, 1H), 1.77 (dd, J = 9.5, 4.2 Hz, 1H), 1.65 (s, 3H), 1.45–1.36 (m, 1H), 1.23 (t, J = 7.2 Hz, 3H).

*Synthesis of allylic carbonate **6***

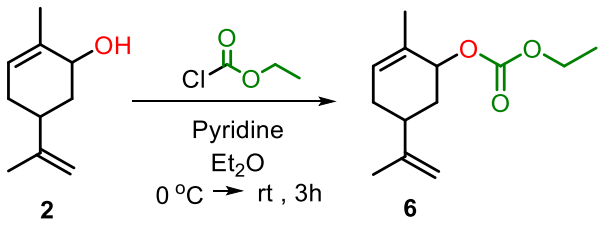

Scheme 3.6: The synthesis of allylic carbonate from carveol

To the solution of compound **2** in diethyl ether in a round-bottom flask, 4 eq. pyridine and 4 eq. ethyl chloroformate were added. Then, it was stirred for 15 minutes at 0 °C.

After stirring at room temperature for 3 hours, the extraction was done with ether and water. After the addition of Na_2SO_4 to the obtained organic layer, it was filtered and concentrated *in-vacuo*. Then, compound **6** was acquired and prepared for NMR analysis. **^{1}H NMR** (500 MHz, $CDCl_3$) δ: 5.60–5.55 (m, 1H), 5.27 (br s, 1H), 4.72–4.69 (m, 2H), 4.21–4.16 (m, 2H), 2.26–2.21 (m, 1H), 2.06 (m, 1H), 1.98–1.90 (m, 1H), 1.70 (s, 3H), 1.67 (dd, J = 2.3, 1.1 Hz, 3H), 1.63–1.53 (m, 1H), 1.32–1.27 (m, 4H).

3.5.2.1.4. Synthesis of allylic nitriles

*Synthesis of allylic nitrile **7***

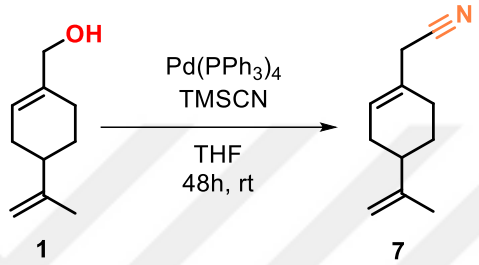

Scheme 3.7: The synthesis of allylic nitrile from perillyl alcohol

Synthesis of compound **7** was conducted in Schlenk flask at Schlenk line to operate the reaction under an inert atmosphere. 10% mol $Pd(PPh_3)_4$ as catalyst was added to Schlenk flask and kept under argon gas atmosphere. Then, dry THF as a solvent was added to it to dissolve the catalyst. The perillyl alcohol solution was prepared by using dry THF and the resulting solution was transferred to the Schlenk flask and followed by the addition of 2.2 eq. trimethylsilyl cyanide (TMSCN) dropwisely using a syringe. It was stirred at room temperature for 48 hours. After that, the compound was extracted with DCM and water, the organic phase was dried over with Na_2SO_4, filtered, and concentrated. Compound **7** was used without further purification. The compound was determined by GC-MS; τ_R= 21.8 min.

*Synthesis of allylic nitrile **8***

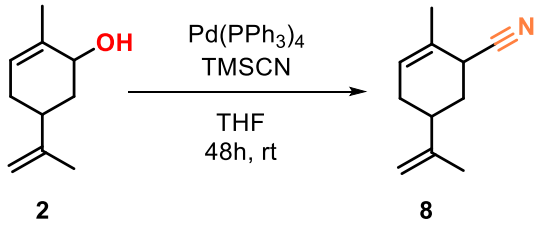

Scheme 3.8: The synthesis of allylic nitrile from carveol

The same procedure was followed as the synthesis of **7**. The compound **8** was used without further purification. The compound was determined by GC-MS; τ_R= 16.3 min.

3.5.2.1.5. Synthesis of allylic carboxylic acids from nitriles

*Synthesis of allylic carboxylic acid **9***

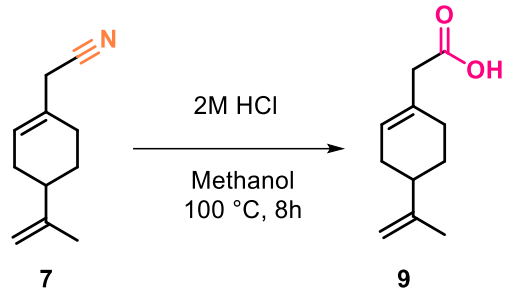

Scheme 3.5: The synthesis of allylic carboxylic acid (**9**) from the nitrile **7**

The as-synthesized nitrile **7** that was mentioned above was used for the synthesis of carboxylic acid. Nitrile (**7**) was dissolved in methanol and 3 mL of 2 M HCl solution was added to it. The mixture was stirred at 100 °C for 8 hours. After that, extraction was done with DCM and water. After drying, filtration, and concentration, the yielded compound **9** was used without further purification. The compound was determined by GC-MS; τ_R= 14.2 min.

*Synthesis of allylic carboxylic acid **10***

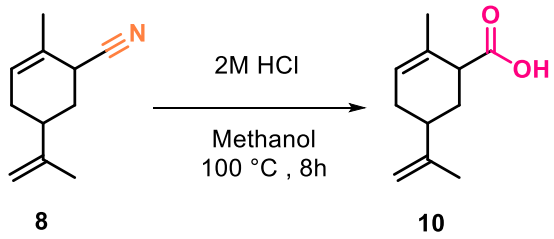

Scheme 3.10: The synthesis of allylic carboxylic acid (**10**) from the nitrile **8**

The as-synthesized nitrile **8** that was mentioned above was used for the synthesis of carboxylic acid. Nitrile (**8**) was dissolved in methanol and 3 mL of 2 M HCl solution was added to it. The mixture was stirred at 100 °C for 8 hours. After that, extraction was done with DCM and water. After drying, filtration, and concentration, compound **10** was yielded without further purification. The compound was determined by GC-MS; τ_R= 14.2 min.

3.5.3. General Procedure for Oxidation Reactions of Different Terpenes in the presence of CoPd/mpg-CN as Catalyst

Optimization reactions were conducted in the presence of α-pinene as the model substrate. The optimization and substrate scope reactions were performed in a tube closed with a rubber septum. First of all, a specific amount of catalyst was put in the tube and 3 mL of solvent was added to it. It was dispersed for 15 minutes with help of an ultrasonic bath. During this time, the oil bath was heated up to the desired temperature. After sonication, a tube was placed in an oil bath and 0.5 mmol of the corresponding substrate and 1.5 eq. of oxidant were added to the reaction mixture by micropipette. It was stirred for the determined time at that temperature. At the end of the reaction, the catalyst was filtered by a syringe filter to remove it from the reaction media. The 40 μL of the remained mixture was taken by micropipette, and it was diluted with 2 mL of ethyl acetate in a GC vial to analyze it by GC-MS.

3.5.3.1. Studies to Construct Calibration Curve for GC-MS to Use in Oxidation Reactions

To construct the calibration curves for the model substrate and the product, which was verbenone, 9 homogeneous mixtures with different concentrations were prepared. First mixture contained 10 μL verbenone, 10 μL n-decane, and 10 μL α-pinene. The second mixture contained 20 μL of each component and so forth. Since TBHP solution contains 40 μL of n-decane in 150 μL, 40 μL n-decane was set as standard. To find the relations between verbenone/n-decane and α-pinene/n-decane, 3 μL samples of each mixture were injected into the GCMS. After each injection, areas of verbenone, α-pinene, and n-decane were recorded by integrating the corresponding peaks. Each mixture's number of moles of each component was calculated as shown in Equation 3.1. Since 40 μL n-decane was standardized, each component's area and the number of moles were divided by 40 μL of the area of n-decane area and the number of moles. After divisions were done, linear relations were found by plotting graphs with respect to the ratio of areas on the x-axis and the ratio of the number of moles on the y-axis. These graphs are shown in Figure 3.3.

$$\frac{Area\ of\ component}{mol\ of\ component} = \frac{Area\ of\ IS\ (40uL)}{mol\ of\ IS\ (40uL)} \tag{3.1}$$

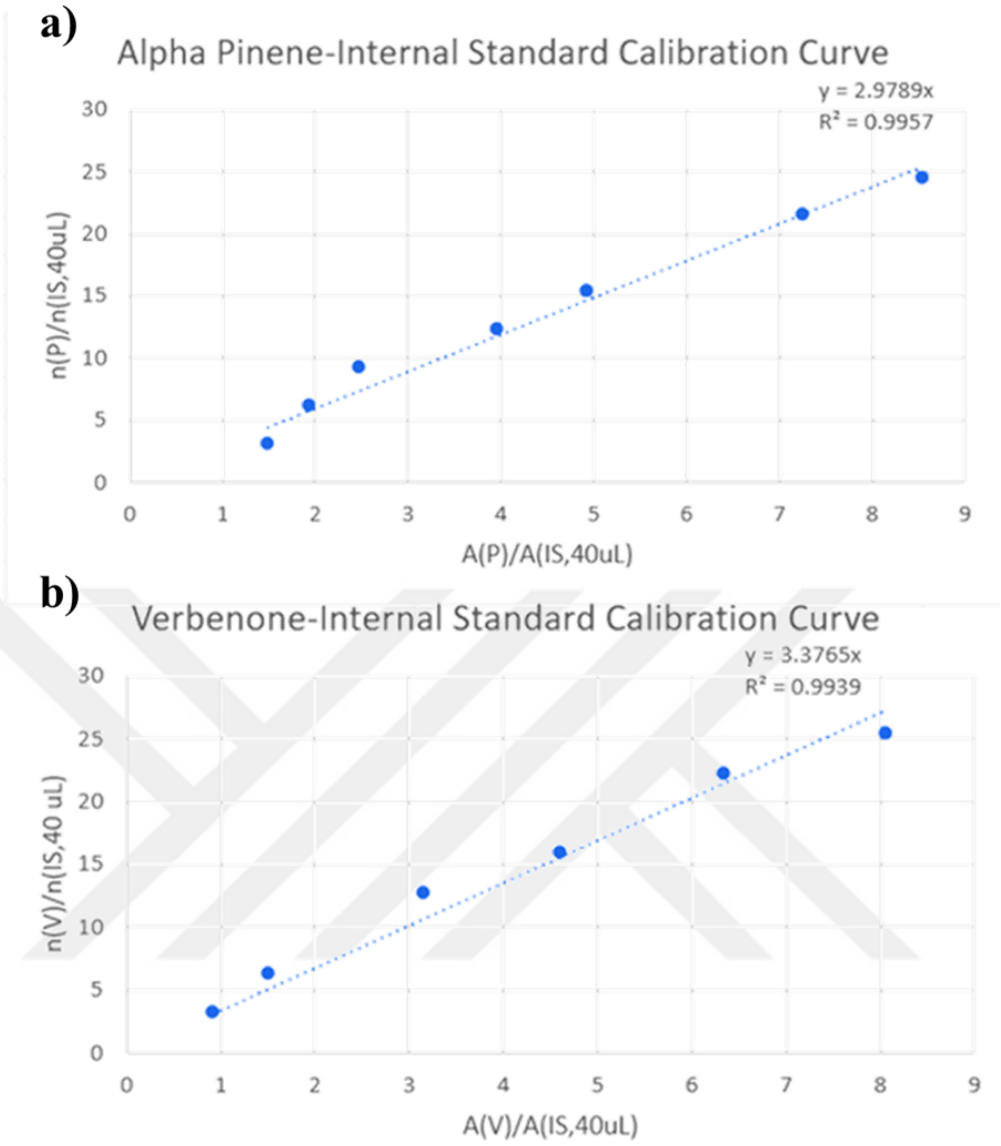

Figure 3.3: Constructed calibration curves for (a) α-pinene-n-decane (b) verbenone-n-decane.

Chapter 4:
RESULTS & DISCUSSION

In this chapter, the structural characterization and photophysical properties of as-synthesized CoPd/mpg-CN nanocatalysts with different ratios were discussed in detail. Moreover, all synthesized nanocatalysts were tested in the dehydrogenation, hydrogenation, and oxidation of various terpenes. Finally, the results of the reusability tests are reported.

4.1. Structural Characterization of CoPd/mpg-CN Nanocatalysts

Structural characteristics of as-synthesized nanocatalysts are explained by several advanced characterization techniques. XRD analysis, TEM analysis, EDS mapping, ICP-MS analysis, XPS analysis, and BET surface area measurement are utilized among these techniques.

4.1.1. XRD and TEM Analyses of CoPd/mpg-CN Nanocatalysts to Determine the Optimum Synthesis Route

To acquire a high quality of bimetallic alloy nanoparticles, the selection of metal precursors is essential. Several experiments have been conducted to decide the usage of the best metal source to yield the desired alloy formation. Powder XRD analysis of the alloy nanoparticles which were formed with the usage of different Pd and Co precursors was studied to figure out this trend. The crystal structure of the nanocatalysts which were prepared with K_2PdCl_4 as a Pd source and different Co sources such as $CoCl_2$, $Co(NO_3)_2$, $Co(OAc)_2$, and $Co(acac)_2$ was shown in Figure 4.1a. Two broad and intense diffraction peaks at 2θ = 27.3° and 39-40° can be clearly seen in the XRD pattern. The peak at 2θ = 27.3° results from the interplanar stacking of mpg-CN structure and corresponds to the (002) diffraction plane. This proved the existence of the mpg-CN in the crystal structure. mpg-CN has another characteristic peak at 2θ = 13.1°, which belongs to the (100) plane and is referred to as in-plane stacking of tri-s-triazine units [219], is not observed in the XRD pattern. This originates from the development of the distance of its interlayers and deformity of in-plane patterns during the formation of bimetallic alloy nanoparticles on support material [73]. Also, the peak of Pd face-centered cubic (111) planes is at 2θ = 39.8°, a slight shifting of this peak toward a higher 2θ degree is proven to the formation of alloy nanoparticles between Co and Pd [220]. According to Figure 4.1 a, the higher shifting is observed for the material which was synthesized with $Co(OAc)_2$ as the Co

source. Figure 4.1 b showed the XRD patterns of nanocatalysts which were prepared with $Co(OAc)_2$ as a Co source and different Pd sources such as $Pd(OAc)_2$, $Pd(acac)_2$, $PdBr_2$, and K_2PdCl_4. In view of the XRD patterns, it demonstrates that the shifting toward a higher degree for Pd (111) plane is detected for the nanocatalyst that was prepared in the presence of $Pd(acac)_2$ as the Pd source.

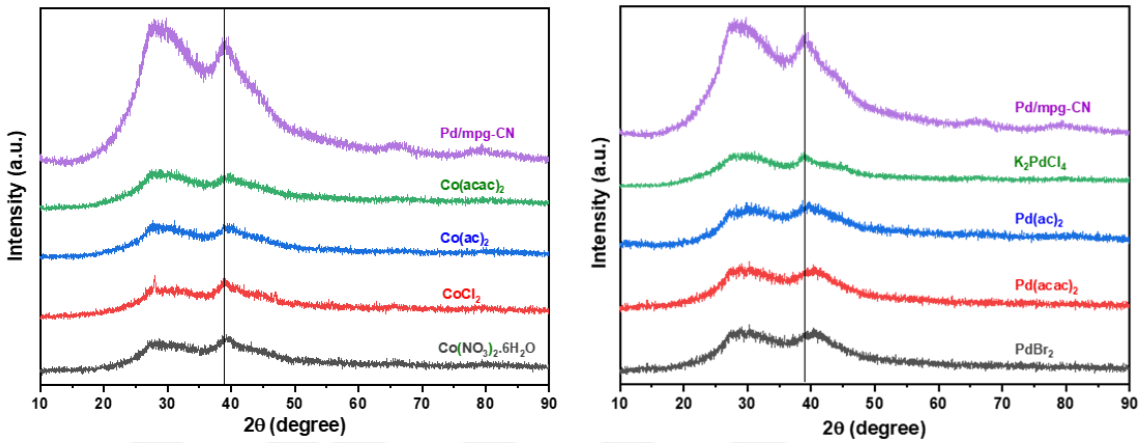

Figure 4.1: XRD patterns of CoPd/mpg-CN nanocatalysts are prepared by using (a) different Co precursors in the presence of K_2PdCl_4 and (b) different Pd precursors in the presence of $Co(OAc)_2$.

Next, TEM analyses were conducted to illuminate the surface morphologies of as-synthesized nanocatalysts and to observe the alloy formation on the support material. Figure 4.2 shows the TEM images of different CoPd/mpg-CN catalysts that were synthesized in the existence of $Co(OAc)_2$ and different Pd precursors. It is determined that CoPd alloys with divergent particle size, morphology, and dispersion are generated on mpg-CN when diverse Pd precursors are utilized during the synthesis. Figure 4.2 a, c, and d demonstrate that CoPd alloys formed as small particles and agglomerations on thin mpg-CN nanolayers. On the other hand, it is determined that the most prevailing CoPd alloy formation on mpg-CN is observed for $Pd(acac)_2$ precursor in Figure 4.2 b. Thereafter, $Co(OAc)_2$ and $Pd(acac)_2$ were utilized as metal sources for the synthesis of CoPd/mpg-CN nanocatalysts.

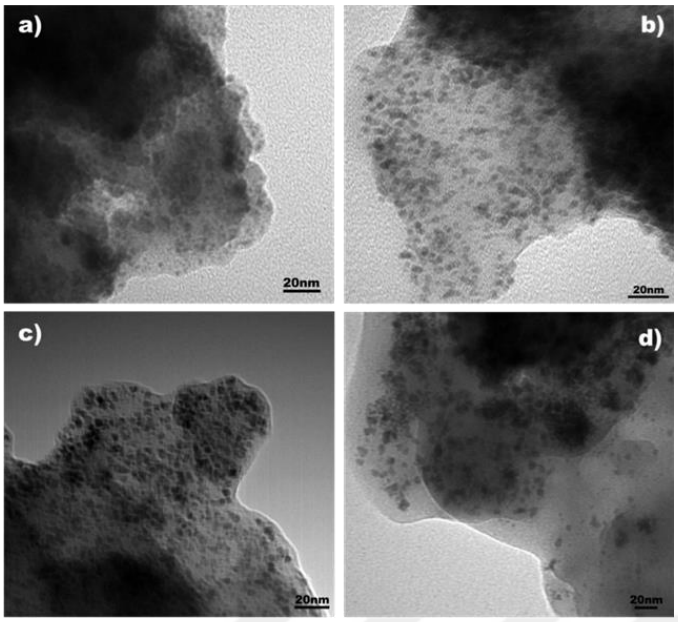

Figure 4.2: TEM images of CoPd/mpg-CN nanocatalysts prepared by using $Co(OAc)_2$ precursor in the presence of different Pd precursors (a) $PdBr_2$, (b) $Pd(acac)_2$, (c) $Pd(OAc)_2$, and (d) K_2PdCl_4.

The morphology, particle size, and distribution of CoPd nanoparticles on mpg-CN nanosheets in the structure of CoPd/mpg-CN which were generated by using optimum conditions ($Co(OAc)_2$ and $Pd(acac)_2$) are examined by TEM analysis. TEM images of this catalyst at two different magnifications are represented in Figure 4.3. The average particle size of nanoparticles is calculated as 3.0 ± 0.4 nm. There is no agglomerated particle or clump observable in the TEM images. The ICP-MS analysis performed on the optimized synthesis of CoPd/mpg-CN nanocatalysts revealed that the CoPd composition of the most active nanocatalyst was $Co_{37}Pd_{63}$. This conclusion was also supported by the catalytic activity tests (*vide infra*). In addition to the alloy composition, the metal loading ratio of the $Co_{37}Pd_{63}$/mpg-CN nanocatalysts was determined to be 15.04 % Pd and 6.02 % Co by mass.

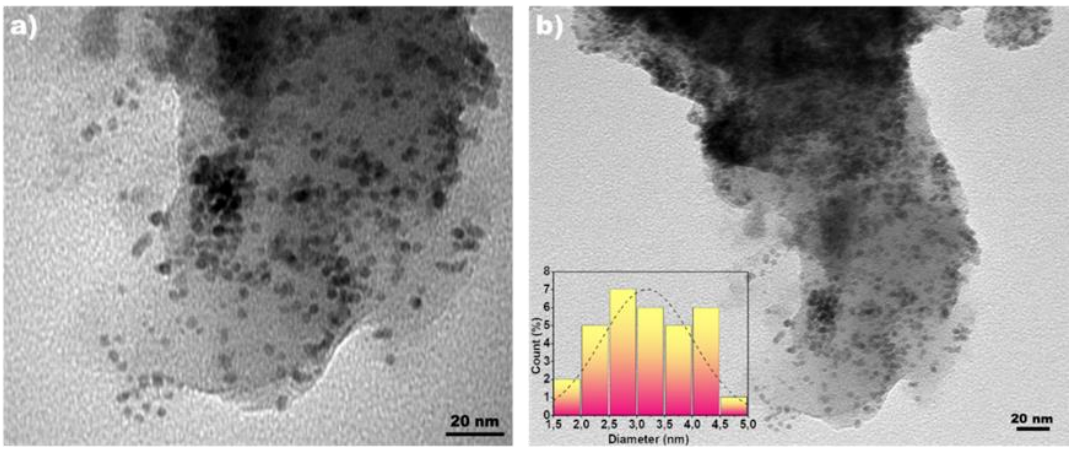

Figure 4.3: Representative TEM images of $Co_{37}Pd_{63}$/mpg-CN nanocatalysts were recorded at different magnifications. The inset shows the particle size histogram.

High-angle annular dark field scanning TEM (HAADF-STEM) and the associated EDS elemental mapping were carried out for further improvement of the alloy formation between Co and Pd atoms, also showing their elemental distribution upon mpg-CN, the recorded images are depicted in Figure 4.4. Based on the images, it can be concluded that Co and Pd atoms show very similar elemental mapping patterns and disperse over mpg-CN smoothly. Also, the solid solution (alloy) form on support material is demonstrated.

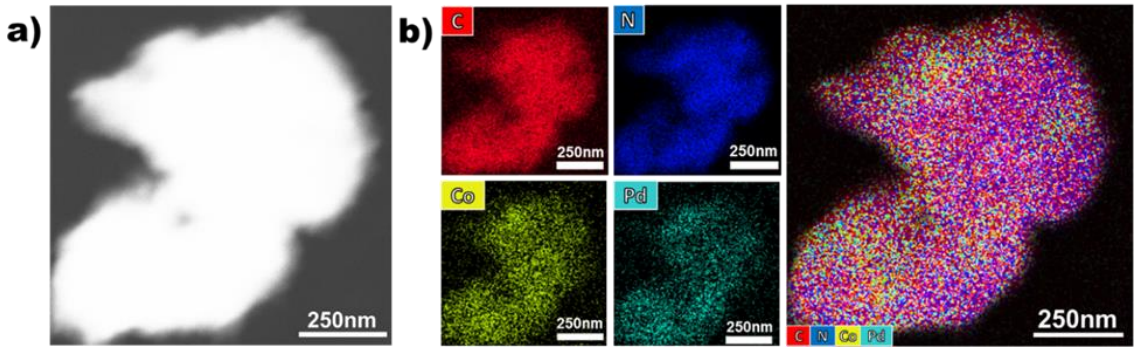

Figure 4.4: (a) HAADF-STEM image and (b) corresponding elemental mapping images of $Co_{37}Pd_{63}$/mpg-CN nanocatalyst.

4.1.2. XRD and TEM Analyses of CoPd/mpg-CN Nanocatalysts at Different Alloy Compositions

The different compositions of CoPd alloy nanoparticles were prepared via the developed procedure. The molar ratios that were used to synthesize all compositions of CoPd NPs are given in Table 4.1.

Table 4.1: Molar ratios for different compositions of CoPd nanoparticles.

Catalyst	Molar ratio ($Pd(acac)_2$:$Co(OAc)_2$)
$Co_{24}Pd_{76}$/mpg-CN	0.15:0.05
$Co_{60}Pd_{40}$/mpg-CN	0.05:0.15
$Co_{32}Pd_{68}$/mpg-CN	0.08:0.12
$Co_{35}Pd_{65}$/mpg-CN	0.12:0.08
$Co_{37}Pd_{63}$/mpg-CN	0.10:0.10

Figure 4.5 demonstrates the XRD patterns of all nanocatalyst compositions. $Co_{37}Pd_{63}$/mpg-CN and $Co_{35}Pd_{65}$/mpg-CN alloy compositions were obligated to the biggest shift toward the highest 2θ angles. Thus, the alloy formation of these nanocatalysts was demonstrated with interaction of Co and Pd metals.

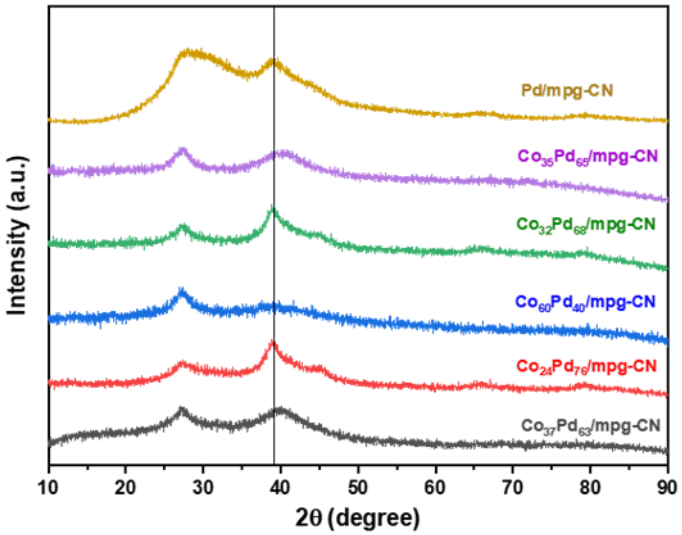

Figure 4.5: XRD patterns of all compositions of CoPd/mpg-CN nanocatalysts by using $Pd(acac)_2$ and $Co(OAc)_2$.

TEM analyses of different compositions were studied and represented in Figure 4.6. The big particles and clumps are observable for $Co_{24}Pd_{76}$/mpg-CN and $Co_{60}Pd_{40}$/mpg-CN

catalysts in Figure 4.6 a, b. The approximate particle size with a partial distribution is 6.5 nm for $Co_{32}Pd_{68}$/mpg-CN and is depicted in Figure 4.6 c. It is detected that $Co_{35}Pd_{65}$/mpg-CN has a good particle distribution on mpg-CN with an average particle size of 3.0 nm which can be seen in Figure 4.6 d. On the other hand, Figure 4.6 e shows the CoPd nanoparticles distributed on support material properly with a 3.01 nm particle size for $Co_{37}Pd_{63}$/mpg-CN.

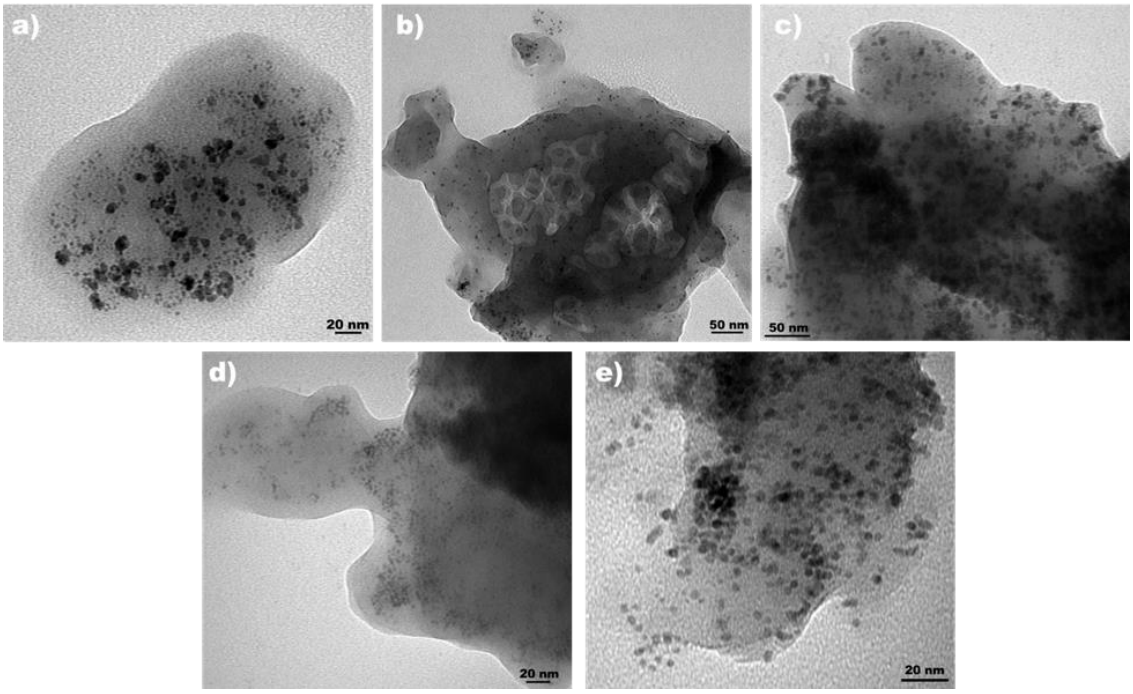

Figure 4.6: TEM images of CoPd/mpg-CN nanocatalysts at different compositions (a) $Co_{24}Pd_{76}$/mpg-CN (b) $Co_{60}Pd_{40}$/mpg-CN (c) $Co_{32}Pd_{68}$/mpg-CN (d) $Co_{35}Pd_{65}$/mpg-CN (e) $Co_{37}Pd_{63}$/mpg-CN.

4.1.3 XPS Analysis

X-ray photoelectron spectroscopy is a fundamental technique for the analysis of surface structure, composition, and chemical oxidation states of the atoms on the surface of nanocatalysts. The detailed XPS analysis of $Co_{37}Pd_{63}$/mpg-CN nanocatalysts was studied and reported herein. XPS survey spectrum represented in Figure 4.7 a expresses the existence of C, N, O, Co, and Pd atoms in the structure. It is observable that the high-resolution XPS spectra of C 1s and N 1s core levels show the all-expected C-N and C-C bonds in mpg-CN structure and are illustrated in Figure 4.7 b, c, and f. In the case of the high-resolution XPS spectrum of C 1s, three main peaks are demonstrated at binding energies (BEs) of 284.5, 286.5, and 288.1 eV as served in Figure 4.7 b. The peak observed at BE of 284.5 eV corresponds to C atoms at C-C and C=C bonds, the peak located at BE of 286.5 eV shows to C-N bond in $C(N)_3$, and the peak at BE of 288.1 eV is attributed to the N-C=N bonds in s-triazine units [221]. Three major peaks can be separated at BEs of 398.7, 400.7, and 401.0 eV in high-resolution XPS spectra of N 1s as represented in Figure 4.7 c. The peaks are assigned to sp^2 hybridized C=N-C, tertiary nitrogen $N(-C-)_3$ groups, and C-N bond, respectively [73,221].

Figure 4.7 d exhibits the high-resolution XPS spectrum of Co 2p region. BEs of two major peaks with asymmetric shapes are detected at 781.2 and 797.0 eV with spin-orbit components of Δ= 15.8 eV, which correspond to metallic Co $2p_{3/2}$ and Co $2p_{1/2}$ core levels. By comparison with reference metallic Co peaks, it is realized the shifting toward higher BEs [222]. The observable weak peaks in the spectrum are satellite peaks.

In the case of the high-resolution XPS spectrum of Pd 3d level, two peaks are noticeable at BEs of 335.5 and 340.7 eV with a spin-orbit component of Δ= 5.2 eV, as shown in Figure 4.7 e. These peaks are attributed to metallic Pd $3d_{5/2}$ and $3d_{3/2}$ core levels. Also, shifting toward higher BEs in comparison to the peak of reference metallic Pd (333.3-333.4 eV) indicates the loss of electron density of Pd atoms [223,224].

Due to the strong electron interactions between Pd and Co atoms, the observed BE shiftings prove that Pd atoms alter their electronic states and contribute to forming alloy structures [222].

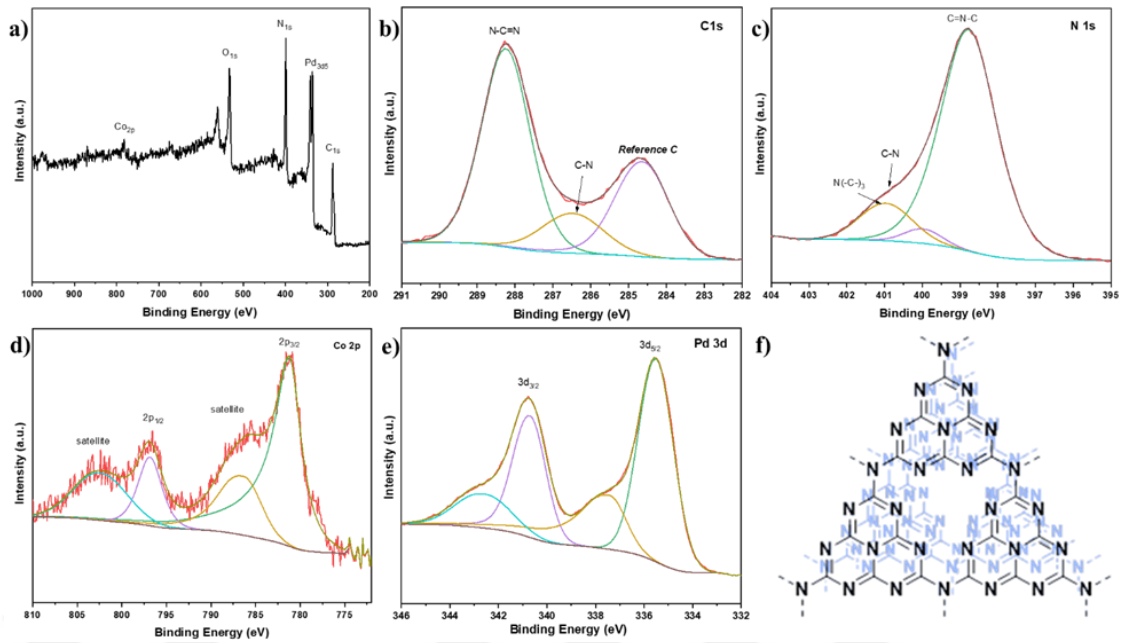

Figure 4.7: (a) XPS survey spectrum and high-resolution XPS spectrums of (b) C 1s, (c) N 1s, (d) Co 2p, (e) Pd 3d, and (f) mpg-CN structure $Co_{37}Pd_{63}$/mpg-CN nanocatalysts.

4.1.4. BET Surface Area Analysis

The understanding of the structural change of mpg-CN, which was utilized as both the stabilizer and support material, is essential to understand its role. Therefore, N_2 adsorption-desorption analyses were performed on pristine mpg-CN and $Co_{37}Pd_{63}$/mpg-CN nanocatalysts and the isotherms are given in Figure 4.8. Both isotherms showed a typical type IV isotherm indicating the existence of mesoporous structure [225]. The average adsorption pore sizes of mpg-CN and $Co_{37}Pd_{63}$/mpg-CN were calculated as 17.0 nm and 15.8 nm, respectively. Moreover, BET surface areas of pristine mpg-CN and $Co_{37}Pd_{63}$/mpg-CN were indicated as 164.89 and 136.61 m^2g^{-1}. It is realized that the pore size and surface area of $Co_{37}Pd_{63}$/mpg-CN decrease compared to pristine mpg-CN due to the blocking pores of mpg-CN with yielded nanoparticles. This result confirms the supporting role of mpg-CN for the stabilization of CoPd nanoparticles.

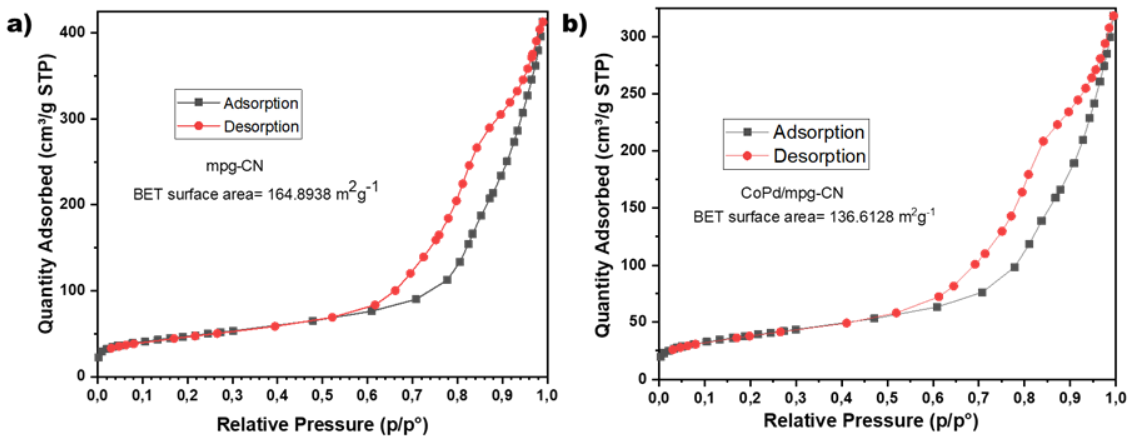

Figure 4.8: BET surface area of (a) pristine mpg-CN and (b) $Co_{37}Pd_{63}$/mpg-CN nanocatalysts.

4.2. Investigation of Photophysical Properties

Photophysical properties of the as-synthesized materials are investigated by UV-Vis diffuse reflectance spectroscopy (UV-DRS), photoluminescence (PL), and time-resolved emission spectroscopy (TRES) to understand whether the heterojunctions are created between mpg-CN and nanoparticles due to the semiconducting property of mpg-CN under visible light.

4.2.1. UV-DRS and PL Analysis

UV-Vis DRS spectrum of mpg-CN and $Co_{37}Pd_{63}$/mpg-CN is presented in Figure 4.9 a. Compared to the absorption of mpg-CN, it is realized that $Co_{37}Pd_{63}$/mpg-CN has a stronger absorption between 360-520 nm. Furthermore, PL is an important tool to observe the heterojunction formation between a semiconductor material and metal nanoparticles. Figure 4.9 b indicates the PL emission of mpg-CN and $Co_{37}Pd_{63}$/mpg-CN and it is observed that the emission of mpg-CN decreases after the formation of nanoparticles on mpg-CN. This result explains the formation of the Schottky junction between mpg-CN and metal nanoparticles.

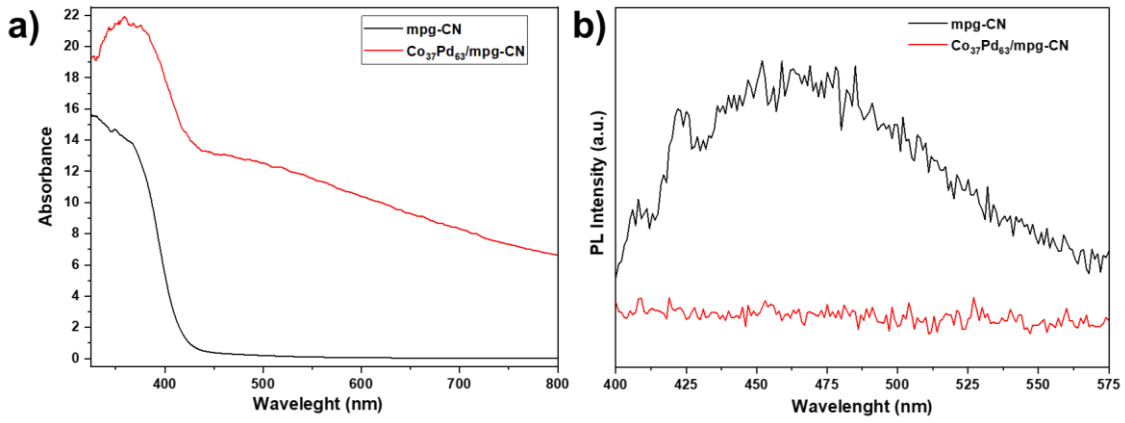

Figure 4.9: (a) UV-Vis DRS spectrum (b) PL spectrum of pristine mpg-CN, $Co_{37}Pd_{63}$/ mpg-CN nanocatalysts.

4.2.2. TRES Analysis

Due to the formation of the Schottky junction between mpg-CN and CoPd nanoparticles, recombination of excited electrons and holes is prevented via charge transfer from the conduction band of mpg-CN to a d-band level of NP. TRES gives a deep insight into the charge transfer dynamics. Figure 4.10 illustrates the TRES of pristine mpg-CN and $Co_{37}Pd_{63}$/mpg-CN nanocatalysts. It is represented that mpg-CN has a longer lifetime in comparison with the lifetime of $Co_{37}Pd_{63}$/mpg-CN nanocatalysts, indicating the rapid decay of electrons on the surface of NPs [226].

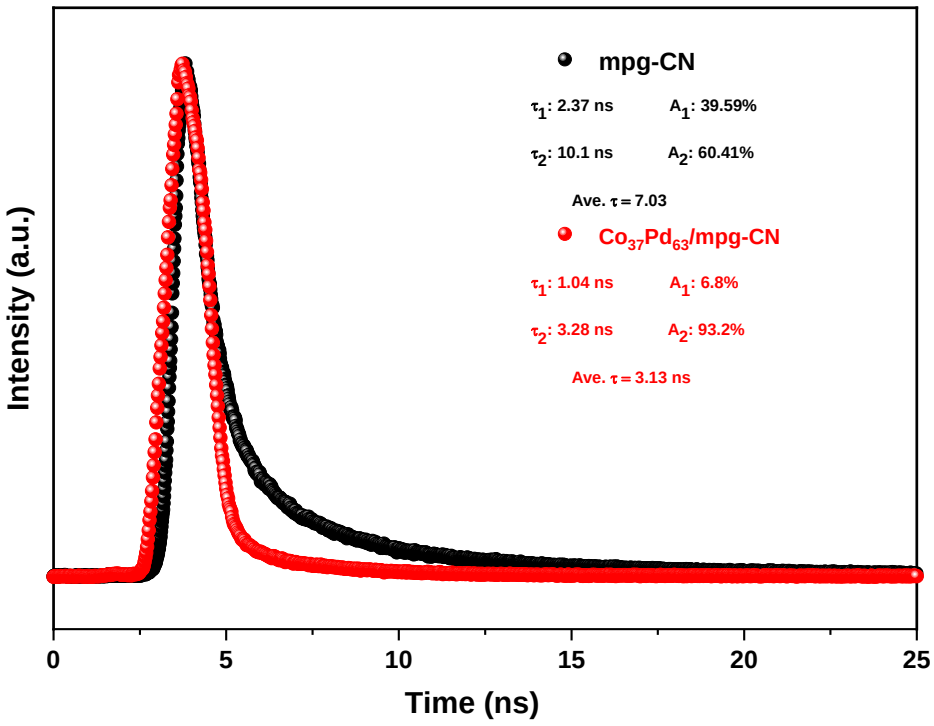

Figure 4.10: Time-resolved emission spectrum of pristine mpg-CN and $Co_{37}Pd_{63}$/mpg-CN nanocatalysts.

4.3. Analysis of Catalytic Activity of CoPd/mpg-CN nanocatalysts

It is essential to exhibit high catalytic activity for a catalyst that is synthesized and characterized successfully. After all characteristic properties of nanocatalysts were identified, the catalytic activity trials investigated three different types of reactions of terpenes such as dehydrogenation, hydrogenation, and oxidation reactions. In this part of the chapter, the results of catalytic activity tests are reported as follows.

4.3.1. Dehydrogenation of Terpenes in the presence of CoPd/mpg-CN Nanocatalysts

Reactions were performed as the procedure was mentioned in Chapter 3. To decide the optimized reaction conditions is crucial to test the activity on several substrates. Hence, optimization studies of catalysts were completed, firstly. α,β,γ–himachalene (**1)** was selected as the model substrate to conduct all optimization reactions. The parameters are demonstrated to choose optimum reaction conditions in the existence of CoPd/mpg-CN nanocatalysts as summarized in Table 4.2.

Firstly, model reaction was conducted with mpg-CN and monometallic Co/mpg-CN catalyst, and desired product ar–himachalene formation was not yielded (Table 4.2, entries 1, 2). On the contrary, the product was obtained with 99% conversion in the presence of monometallic Pd/mpg-CN (Table 4.2, entry 3). The reactions were performed at 120 °C for 14 hours in the presence of CoPd/mpg-CN nanocatalysts at different compositions to examine the effect of the bimetallic alloy composition on catalytic activity. It was observed that the altered alloy composition did not have a significant impact on the activity (Table 4.2, entries 4-5). However, the highest conversion rate was achieved at 97% with $Co_{37}Pd_{63}$/mpg-CN nanocatalysts (Table 4.2, entry 5). Therefore, this alloy composition was chosen to pursue the catalytic activity tests considering the Pd amount. The reactions were proceeded to monitor the effect of catalyst amount and temperature in the context of the activity. The conversion rate dropped to 49%, dramatically, when 5 mg catalyst was utilized in the model reaction (Table 4.2, entry 6). Thus, reactions were performed with 10 mg catalyst amount for further experiments. It was shown that any product formation did not provide in the case that reaction temperature was decreased to 100 °C (Table 4.2, entry 7). In the light of these, optimized conditions were constituted as 10 mg of $Co_{37}Pd_{63}$/mpg-CN catalyst, 120 °C, and 14 hours.

Table 4.2. Optimization of the dehydrogenation of terpenes in the presence of CoPd/mpg-CN nanocatalysts[a]

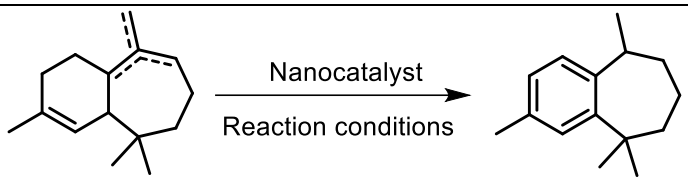

1 **2**

Entry	Catalyst	Reaction Conditions	Conversion[b] (%)
1	mpg-CN	14 h, 120 °C, 10 mg	-
2	Co/mpg-CN	14 h, 120 °C, 10 mg	-
3	Pd/mpg-CN	14 h, 120 °C, 10 mg	99
4	$Co_{35}Pd_{65}$/mpg-CN	14 h, 120 °C, 10 mg	94
5	**$Co_{37}Pd_{63}$/mpg-CN**	**14 h, 120 °C, 10 mg**	**97**
6	$Co_{37}Pd_{63}$/mpg-CN	14 h, 120 °C, 5 mg	49
7	$Co_{37}Pd_{63}$/mpg-CN	14 h, 100 °C, 10 mg	-

*[a] Reaction conditions: 1.00 mmol of **1a** and 10 mg of nanocatalyst for 14 h at 120 °C unless otherwise noted. [b] Conversions calculated based on ^{1}H NMR.*

Under the optimized conditions, the catalytic activity of $Co_{37}Pd_{63}$/mpg-CN was studied on dehydrogenation reactions of several terpenes, and the results are depicted in Table 4.3. The reactions were successfully completed for various terpenes in the presence of $Co_{37}Pd_{63}$/mpg-CN nanocatalyst. First of all, no product formation was detected for the dehydrogenation of limonene **3** under optimized conditions because of the important effect of temperature on the dehydrogenation of limonene [63]. Thus, the optimized conditions were improved by elevating the temperature and extending the reaction time for limonene and various substrates. Increasing the reaction temperature to 180 °C caused to 99% conversion of limonene **3** to *p*–cymene **4** (Table 4.3, entry 1). The conversion of terpinolene **5** was provided to dehydrogenation product **6** as 91% (Table 4.3, entry 2). It was recognized that dehydrogenation of α–terpinene **7** was yielded to *p*–cymene **5** with 99% (Table 4.3, entry 3). As shown in Table 4.3, the formation of product **5** occurred at a prolonged reaction time of 18 h for γ-terpinene **8** (Table 4.3, entry 4). Carvone **9** was converted to carvacrol **10** with an 18% yield after enhancing the reaction time of 24 h and temperature of 180 °C (Table 4.3, entry 5). The dehydrogenation of carveol **11** was performed at 180 °C for 24 h to afford product **10** with 99% conversion (Table 4.3, entry 6). The conversion of verbenone **12** to product **4** was not achieved even though the reaction time and temperature were increased (Table 4.3, entry 7).

Table 4.3. $Co_{37}Pd_{63}$/mpg-CN catalyzed dehydrogenation reactions of terpenes[a]

Entry	Substrate	Product	Conversion[b] (%)
1[c]	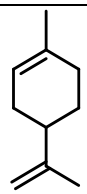 **3**	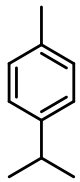 **4**	99
2	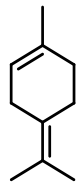 **5**	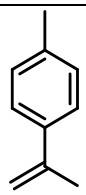 **6**	91
3	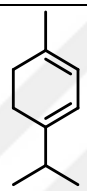 **7**	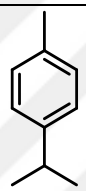 **4**	99
4[d]	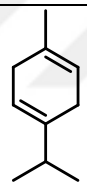 **8**	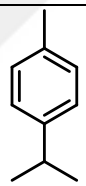 **4**	99
5[c,e]	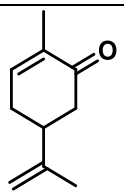 **9**	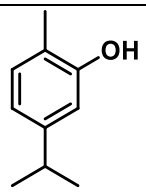 **10**	18
6[c,e]	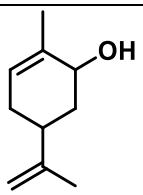 **11**	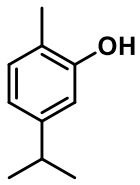 **10**	99

7[c,e]	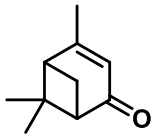 **12**	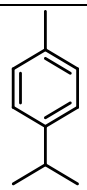 **4**	-

[a] Reaction conditions: 1.00 mmol substrate and 10 mg nanocatalyst, 14 h, 120 °C. [b] Conversions are calculated by ^{1}H NMR. [c] 180 °C. [d]18 h. [e] 24 h.

4.3.2. Hydrogenation of Terpenes in the presence of CoPd/mpg-CN Nanocatalysts

To investigate the activity of CoPd/mpg-CN nanocatalysts in the hydrogenation of terpenes, perillyl alcohol **1** was chosen as the model substrate. The formation of possible products and reaction conditions are given in Scheme 4.1.

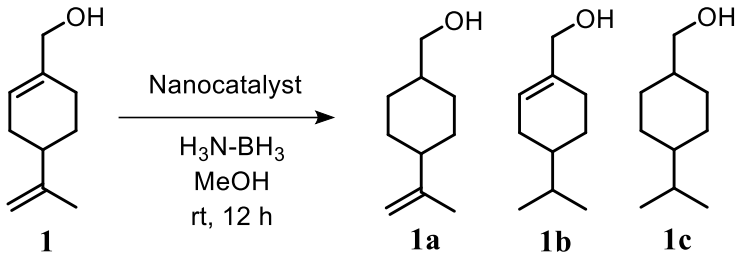

Scheme 4.1: Hydrogenation of perillyl alcohol as a model substrate

The reactions were conducted with $Co_{35}Pd_{65}$/mpg-CN and $Co_{37}Pd_{63}$/mpg-CN nanocatalyst to yield the possible products as shown in Scheme 4.1. Both catalysts produced the products with high conversion rates. However, $Co_{37}Pd_{63}$/mpg-CN was selected and utilized as a catalyst in the hydrogenation reaction of as-synthesized substrates in the context of selectivity of the products and less Pd amount. Table 4.4 shows the results of $Co_{37}Pd_{63}$/mpg-CN catalyzed hydrogenation of terpenes.

It was recognized that acetate structure **3** was decomposed during the reaction and hydrogenation products **11** & **12** of this substrate were listed. The total conversion was calculated as 93% for substrate **3**. Product **11** which was produced with a reduction of the double bond at the tail of the structure was produced at the rate of 13% while product **12**'s that was reduced both double bonds at the rate of 80% (Table 4.4, entry 1). As demonstrated by Table 4.4, entry 2, two different product formations were afforded as desired product **13** and product **11** that was formed with hydrogenation of decomposed substrate with 75% conversion. The allylic acetate **4** which was derived from the carveol was converted to **13** and **11** with a conversion of 33% and 42%, respectively. Allylic carbonates **5** & **6** were converted to the same product **11** with 32% and 34% conversion, respectively (Table 4.4, entries 3, 4). Only one product **14** which was reduced double bond at the tail was obtained for substrate **7** in the conversion of 20% (Table 4.4, entry 5). According to Table 4.4, entry 6, two diverse products were detected without the decomposition of substrate **8**. Product **15** which the nitrile group and double bonds in the structure were reduced was formed in a conversion of 93% while product **16** which was obtained with the reduction of double bonds was detected in a conversion of 5%.

Carboxylic acid derivatives were derived from as-prepared nitriles. The functional group of carboxylic acid **9** and a single double bond at the tail of the structure were hydrogenated to yield product **17** with 56% conversion (Table 4.4, entry 7). In the consequence of hydrogenation of carboxylic acid derivative **10**, the attained products were alcohol generated by reduction of the double bond with functional -COOH as depicted in Table 4.4, entry 8. Alcohols **18** & **19** were provided 24% and 76%, respectively.

Table 4.4. Hydrogenation reactions of terpenes in the presence of $Co_{37}Pd_{63}$/mpg-CN nanocatalyst

Entry	Substrate	Conversion[a] (%) / Product/s
1	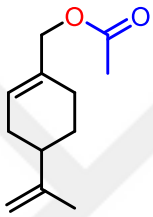 **3**	 **11** 13% 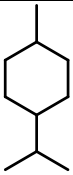 **12** 80%
2	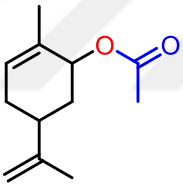 **4**	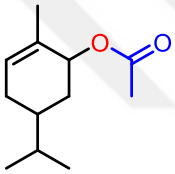 **13** 33% 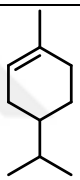 **11** 42%
3	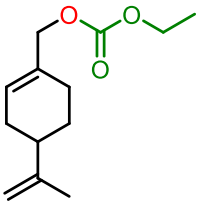 **5**	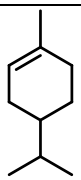 **11** 32%
4	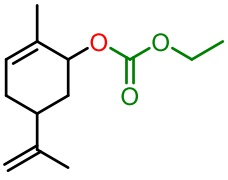 **6**	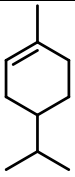 **11** 34%

5	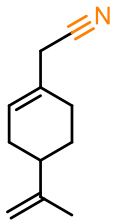 **7**	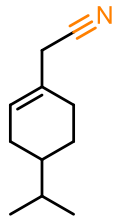 **14** 20%
6	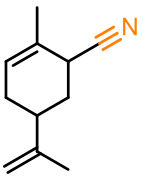 **8**	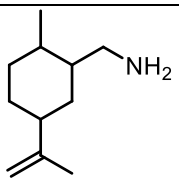 **15** 93% 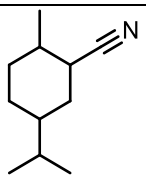 **16** 5%
7	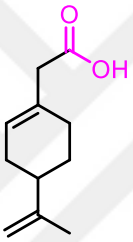 **9**	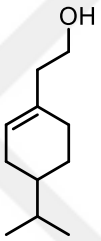 **17** 56%
8	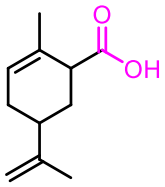 **10**	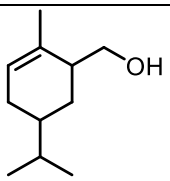 **18** 24% 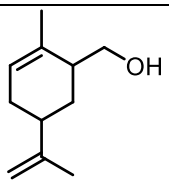 **19** 76%

[a]*Conversions were calculated by GC-MS.*

4.3.3. Oxidation of Terpenes in the presence of CoPd/mpg-CN Nanocatalysts

As mentioned in part 4.3.1, optimized reaction conditions are required to decide before substrate scope. In this part, the studied optimization trials and substrate scope of oxidation are explained in detail. Optimization studies were examined on model reaction where α-pinene was selected as a model substrate, and possible products were illustrated by Scheme 4.2.

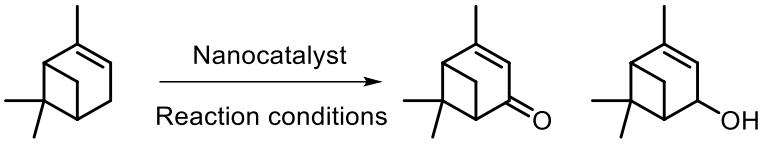

Scheme 4.2: Model reaction for optimization studies of oxidation reactions

The altered parameters to determine the optimized reaction conditions are demonstrated in Table 4.5. Initially, a solvent-free reaction was conducted with a 10 mg catalyst, TBHP as oxidant, at 90 °C for 24 hours and any product formation was not observed (Table 4.5, entry 1). To find the most suitable solvent for the reaction medium, acetonitrile (MeCN) was utilized as a solvent under the same conditions. Hereby, verbenone as product was produced with 94% conversion and 93% yield (Table 4.5, entry 2). When the solvent was changed to dioxane, conversion was obtained as 92% while yield decreased dramatically to 0.2% for the desired product (Table 4.5, entry 3). As a consequence of these results, catalyst amount was studied in the presence of MeCN as solvent. Compared to the results of entries 2 and 4, it was clearly communicable that conversion was not substantially affected by this change; however, the yield was calculated as 7% (Table 4.5, entry 4). Then, the solvent effect was proceeded to monitor. Conversion and yield rates dropped when the reactions were performed with other solvents (Table 4.5, entries 5-8); hence, MeCN was used as a solvent in all other reactions. After that, oxidant screening was performed. When O_2 was provided to the reaction, conversion and yield of the product were calculated as 62% and 7%, respectively (Table 4.5, entry 9). Also, it was concluded that hydrogen peroxide (H_2O_2) as an oxidant did not yield any product (Table 4.5, entry 10). Finally, the reaction temperature decreased to 70 °C to determine the convenient temperature to obtain the desired product. In this case, conversion was calculated as 94% and yield as 16% at the end of the reaction (Table 4.5, entry 11). As a result of these, optimized conditions were defined as 10 mg of nanocatalyst, MeCN as the solvent, and TBHP as the oxidant at 90 °C for 24 hours.

Table 4.5. Optimization of the oxidation of terpenes in the presence of $Co_{37}Pd_{63}$/mpg-CN nanocatalyst

Entry	Catalyst	Reaction conditions	Conversion[a] (%)	Yield[a] (%)
1	$Co_{37}Pd_{63}$/mpg-CN	10 mg, solventless, TBHP, 90 °C, 24 h	-	-
2	$Co_{37}Pd_{63}$/mpg-CN	10 mg, MeCN, TBHP, 90 °C, 24 h	94	93
3	$Co_{37}Pd_{63}$/mpg-CN	10 mg, Dioxane, TBHP, 90 °C, 24 h	92	0.2
4	$Co_{37}Pd_{63}$/mpg-CN	5 mg, MeCN, TBHP, 90 °C, 24 h	89	7
5	$Co_{37}Pd_{63}$/mpg-CN	5 mg, IBN, TBHP, 90 °C, 24 h	72	2
6	$Co_{37}Pd_{63}$/mpg-CN	5 mg, n-BuOH, TBHP, 90 °C, 24 h	59	21
7	$Co_{37}Pd_{63}$/mpg-CN	5 mg, Toluene, TBHP, 90 °C, 24 h	78	2
8	$Co_{37}Pd_{63}$/mpg-CN	5 mg, THF, TBHP, 90 °C, 24 h	54	0
9	$Co_{37}Pd_{63}$/mpg-CN	10 mg, MeCN, O_2, 90 °C, 24 h	62	7
10	$Co_{37}Pd_{63}$/mpg-CN	10 mg, MeCN, H_2O_2, 90 °C, 24 h	-	-
11	$Co_{37}Pd_{63}$/mpg-CN	10 mg, MeCN, TBHP, 70 °C, 24 h	94	16

[a]*Conversion and yield were calculated by GC-MS.*

The substrate scope of oxidation reactions was studied after optimized conditions were determined and the results are shown in Table 4.6. According to the results in Table 4.6, $Co_{37}Pd_{63}$/mpg-CN nanocatalyst demonstrated the catalytic activity for all substrates. As depicted in Table 4.6, entry 1, the total conversion of limonene **1** was calculated as 17% while main product **2** formation was 8%, and side product **3** formation was 9%. Terpinolene **4** converted to product **5** with 99% of conversion (Table 4.6, entry 2). The oxidation of α–terpinene **6** and γ–terpinene **8** was achieved to product **7** in the conversion

of 99% (Table 4.6, entries 3-4). The indicated product **10** was yielded with 14% from β–pinene **9** (Table 4.6, entry 5). It was realized that the formation of ketones **12** and **14** occurred with 7% and 16% conversion for 2–carene **11** and 3–carene **13**, respectively. Moreover, the side product, p–cymnene, **7** formation was noticed with 22%. (Table 4.6, entries 6-7). Valencene **15** formed nootkatone **16** with 49% conversion (Table 4.6, entry 8). It was observed that the product **18** formation was detected in the proportion of 62% in the presence of α,β,γ–himachalene **17** as substrate (Table 4.6, entry 9).

Table 4.6. $Co_{37}Pd_{63}$/mpg-CN catalyzed oxidation of various terpenes

Entry	Substrate	Conversion[a] (%)	
		Product	Side Product
1	 **1**	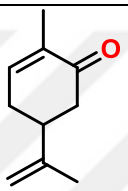 **2** 8%	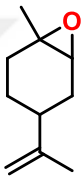 **3** 9%
2	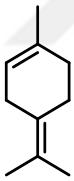 **4**	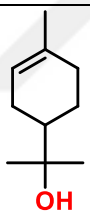 **5** 99%	X
3	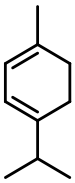 **6**	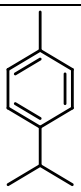 **7** 99%	X
4	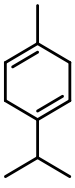 **8**	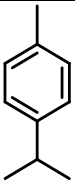 **7** 99%	X

5	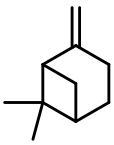 **9**	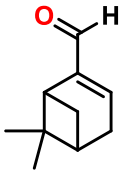 **10** 14%	X
6	 **11**	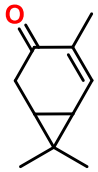 **12** 7%	X
7	 **13**	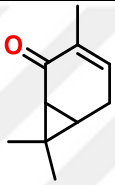 **14** 16%	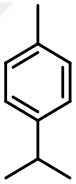 **7** 22%
8	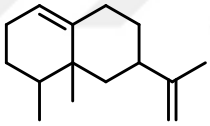 **15**	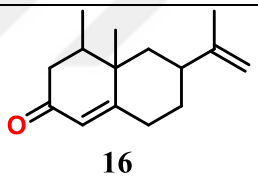 **16** 49%	X
9	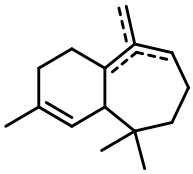 **17**	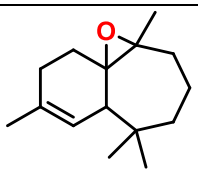 **18** 62%	X

[a]*Conversion and yield were calculated by GC-MS.*

4.4. Reusability tests of CoPd/mpg-CN nanocatalysts

The reusability of heterogeneous catalysts is one of the most significant properties. Therefore, reusability tests were performed for all types of reactions which were covered in the part for catalytic activity tests. The results of the experiments are presented in this part.

Initially, reusability tests for dehydrogenation reactions of nanocatalyst were studied on the model reaction under optimized conditions which were reported in part 4.3.1, and the results are exhibited in Figure 4.11. It is concluded that $Co_{37}Pd_{63}$/mpg-CN nanocatalysts can be re-used for up to 2 cycles. Due to the solvent-free reaction condition of the dehydrogenation reaction, the active sites of catalyst could be covered and poisoned; thus, the surface absorption were blocked during the reusability test. Thus, nanocatalyst lost its activity after the second cycle. As is seen in Figure 4.11 b, the morphological structure of the nanocatalyst was not changed at the end of the 4 cycles.

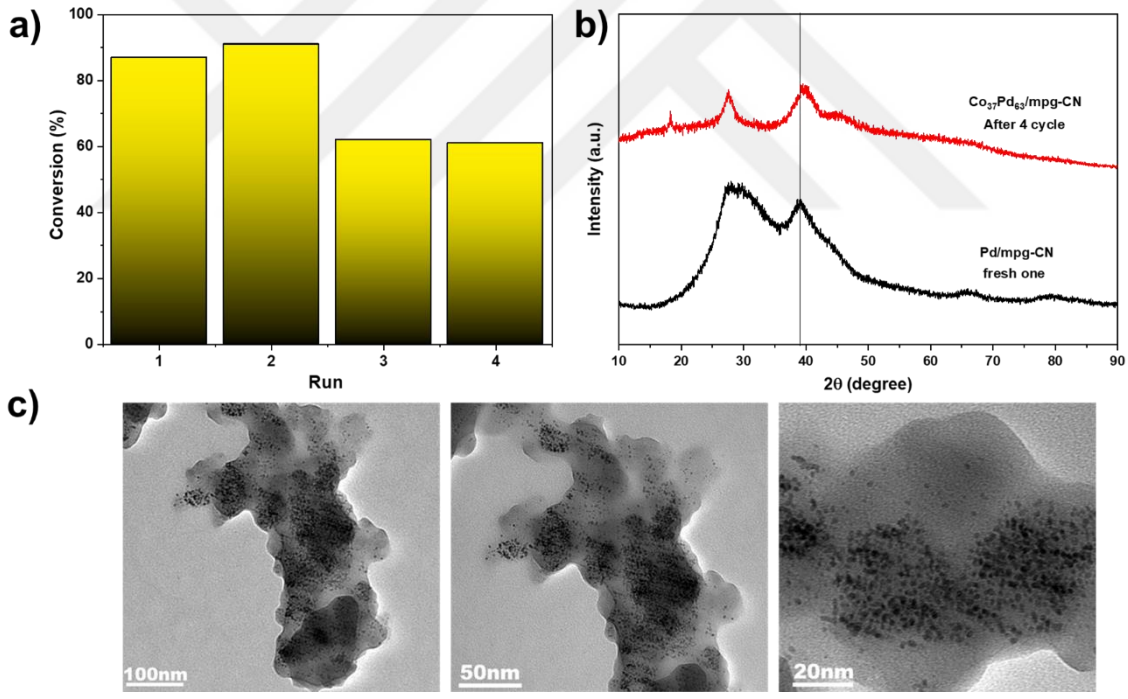

Figure 4.11: (a) Corresponding graph of the result of the reusability test for dehydrogenation reaction of terpenes (b) XRD pattern of nanocatalyst after the 4th cycle (c) representative TEM image of the catalyst after the last run.

Secondly, the reusability property of nanocatalyst was investigated in the hydrogenation reaction of terpenes, and the results are demonstrated in Figure 4.12. Nanocatalyst can be reutilized for up to 4 cycles without a huge drop-in conversion rate to 89%. Considering

the XRD pattern and TEM image in Figure 4.12 b, c, any sharp structural and morphological changes were not detected for the nanocatalysts after 4 cycles.

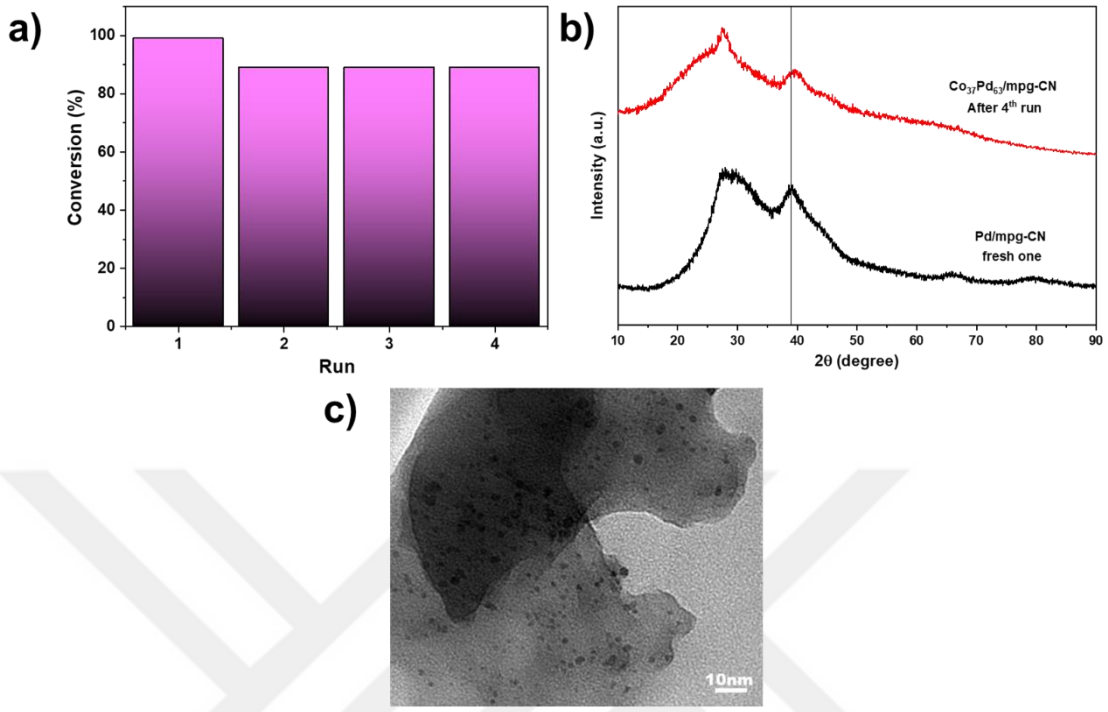

Figure 4.12: (a) Corresponding graph of the result of the reusability test for hydrogenation reaction of terpenes, (b) XRD pattern of nanocatalyst after the 4th cycle, and (c) representative TEM image of the catalyst after the last cycle.

Finally, a reusability study of the nanocatalyst was performed for the oxidation reaction of terpenes, and the results are displayed in Figure 4.13. It is observed that the nanocatalyst did not lose its activity for oxidation reaction after 5 cycles, the activity of the nanocatalyst retained 86% in the last cycle (Figure 4.13 b). Moreover, any obvious alterations in the structure and morphology of the nanocatalyst were not encountered after 5 cycles in Figure 4.13 a, c.

In the conclusion of reusability tests, the continuous high catalytic activity of $Co_{37}Pd_{63}$/mpg-CN nanocatalyst was indicated for dehydrogenation, hydrogenation, and oxidation reactions of terpenes.

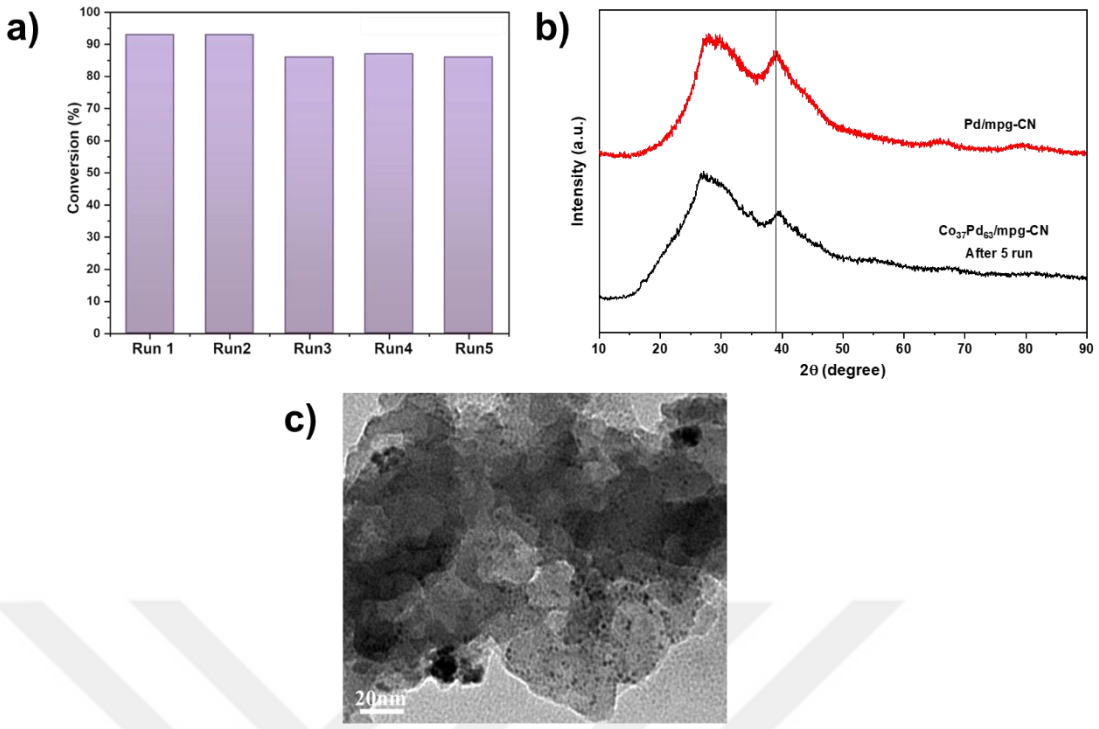

Figure 4.13: (a) Corresponding graph of the result of the reusability test for hydrogenation reaction of terpenes (b) XRD pattern of nanocatalyst after the 5th cycle (c) representative TEM image of the catalyst after the last cycle.

Chapter 5:
CONCLUSION AND OUTLOOK

In this thesis, a novel and facile protocol were developed to synthesize bimetallic alloy nanoparticles on a support material. mpg-CN, which was used both as support material and stabilizer, was prepared by utilizing the well-established hard-template polycondensation method. After the preparation of mpg-CN, bimetallic CoPd alloy nanoparticles were generated on mpg-CN via a chemical reduction method. The effect of different precursors on alloy formation was investigated to reveal the optimum pathway for the synthesis of nanocatalysts. Analyses of alloy formation of nanocatalysts were completed by using XRD and TEM. After the selection of the best alloy formation constructed by $Co(OAc)_2$ and $Pd(acac)_2$ precursors, different compositions of CoPd/mpg-CN were studied by alteration of Co:Pd ratios during synthesis to further use in catalytic activity experiments. Characterization of all compositions unveiled that $Co_{35}Pd_{65}$/mpg-CN and $Co_{37}Pd_{63}$/mpg-CN could be successfully synthesized employing XRD and TEM analysis. Detailed characterization of $Co_{37}Pd_{63}$/mpg-CN was served by XPS, EDS, BET, UV-DRS, and PL analysis. Taking the results into consideration, alloy formation was proved. Investigation of catalytic activity was provided by derivatization of terpenes such as dehydrogenation, hydrogenation, and oxidation reactions. After the optimization table was constructed, the related nanocatalysts were used in the dehydrogenation of 7 different terpenes. 5 of them were able to be converted into the desired product with high conversion rates while the transformation of one substrate was converted with a low rate and one of them failed. In the part of catalytic hydrogenation of terpenes, 10 diverse terpenes were synthesized and hydrogenated in the presence of $Co_{37}Pd_{63}$/mpg-CN nanocatalysts. The hydrogenation of all substrates was achieved; however, it was observed that some substrates, namely 3, 5, 6, decomposed during the process, and the hydrogenation products of decomposed substrates were yielded. It can be concluded that the $Co_{37}Pd_{63}$/mpg-CN did not have selectivity on the hydrogenation reaction. In the next part, CoPd/mpg-CN catalyzed oxidation reactions were performed. After the construction of calibration curves and optimization reactions, 9 substrates could be oxidized under optimized conditions. According to the reusability tests, the nanocatalysts were able to re-use up to 2 cycles in dehydrogenation, 4 cycles in hydrogenation with 89% conversion in the last run, and 5 cycles in oxidation with 86% conversion in the last run. [227]

That being said results showed that the success of the mpg-CN/CoPd nanocatalysts was revealed for the transformation reactions of many natural terpenes in the context of high efficiency and cost-effective method. The presented thesis contributed to the literature in terms of the development of a novel synthesis method for the synthesis of mpg-CN stabilized PdM alloy nanoparticles and the application of as-synthesized nanocatalysts in the conversion of several terpenes into value-added products. Overall, I believe that mpg-CN-supported bimetallic alloy nanocatalysts will be exploited widely in the derivatization of natural terpenes in near future and be served not only in metal catalysis but also photocatalysis in organic applications due to the acceptable photophysical properties. Moreover, we believe that the PdM/mpg-CN nanocatalysts have a high potential to be utilized in industry.

BIBLIOGRAPHY

[1] S. Wacławek, V. V. T. Padil, and M. Černík, “Major Advances and Challenges in Heterogeneous Catalysis for Environmental Applications: A Review,” *Ecological Chemistry and Engineering S*, vol. 25, no. 1, pp. 9–34, Mar. 2018, doi: 10.1515/eces-2018-0001.

[2] J. Wisniak, “The History of Catalysis. From the Beginning to Nobel Prizes,” *Educación Química*, vol. 21, no. 1, pp. 60–69, Jan. 2010, doi: 10.1016/s0187-893x(18)30074-0.

[3] W. T. GRUBB, “Catalysis, Electrocatalysis, and Hydrocarbon Fuel Cells,” *Nature*, vol. 198, no. 4883, pp. 883–884, Jun. 1963, doi: 10.1038/198883b0.

[4] S. I. Sinar Mashuri *et al.*, “Photocatalysis for Organic Wastewater Treatment: From the Basis to Current Challenges for Society,” *Catalysts*, vol. 10, no. 11, p. 1260, Oct. 2020, doi: 10.3390/catal10111260.

[5] G. Rothenberg, *Catalysis*. Wiley, 2008. doi: 10.1002/9783527621866.

[6] G. Baskar, R. Aiswarya, S. Soumiya, N. Mohanapriya, and S. Roselin Nivetha, “Recent Advances in Heterogeneous Catalysts for Biodiesel Production,” *Journal of Energy and Environmental Sustainability*, vol. 4, pp. 1–5, Jul. 2017, doi: 10.47469/jees.2017.v04.100038.

[7] A. Z. Fadhel, P. Pollet, C. L. Liotta, and C. A. Eckert, “Combining the Benefits of Homogeneous and Heterogeneous Catalysis with Tunable Solvents and Nearcritical Water,” *Molecules 2010, Vol. 15, Pages 8400-8424*, vol. 15, no. 11, pp. 8400–8424, Nov. 2010, doi: 10.3390/molecules15118400.

[8] Y. Zhang, “Preparation of heterogeneous catalysts based on CWAO technology,” *Journal of Physics: Conference Series*, vol. 1549, no. 3, p. 032052, Jun. 2020, doi: 10.1088/1742-6596/1549/3/032052.

[9] K. L. Fujdala and T. D. Tilley, “Design and synthesis of heterogeneous catalysts: the thermolytic molecular precursor approach,” *Journal of Catalysis*, vol. 216, no. 1–2, pp. 265–275, May 2003, doi: 10.1016/s0021-9517(02)00106-9.

[10] X. Cheng, “Nanostructures: fabrication and applications,” *Nanolithography: The Art of Fabricating Nanoelectronic and Nanophotonic Devices and Systems*, pp. 348–375, Jan. 2014, doi: 10.1533/9780857098757.348.

[11] Y. Zhou, H. Yin, and S. Ai, “Applications of two-dimensional layered nanomaterials in photoelectrochemical sensors: A comprehensive review,” *Coordination Chemistry Reviews*, vol. 447, p. 214156, Nov. 2021, doi: 10.1016/j.ccr.2021.214156.

[12] R. Keçili, S. Büyüktiryaki, I. Dolak, and C. M. Hussain, “The use of magnetic nanoparticles in sample preparation devices and tools,” *Handbook of Nanomaterials in Analytical Chemistry: Modern Trends in Analysis*, pp. 75–95, Jan. 2020, doi: 10.1016/b978-0-12-816699-4.00005-0.

[13] J. Jeevanandam, A. Barhoum, Y. S. Chan, A. Dufresne, and M. K. Danquah, “Review on nanoparticles and nanostructured materials: history, sources, toxicity and regulations,” *Beilstein Journal of Nanotechnology 9:98*, vol. 9, no. 1, pp. 1050–1074, Apr. 2018, doi: 10.3762/bjnano.9.98.

[14] V. Singh, P. Yadav, and V. Mishra, “Recent Advances on Classification, Properties, Synthesis, and Characterization of Nanomaterials,” *Green Synthesis of Nanomaterials for Bioenergy Applications*, pp. 83–97, Aug. 2020, doi: 10.1002/9781119576785.ch3.

[15] H. A. E. Omr, M. W. Horn, and H. Lee, “Low-Dimensional Nanostructured Photocatalysts for Efficient CO2 Conversion into Solar Fuels,” *Catalysts 2021, Vol. 11, Page 418*, vol. 11, no. 4, p. 418, Mar. 2021, doi: 10.3390/catal11040418.

[16] F. T. Rabouw and C. de Mello Donega, “Excited-State Dynamics in Colloidal Semiconductor Nanocrystals,” *Topics in Current Chemistry 2016 374:5*, vol. 374, no. 5, pp. 1–30, Aug. 2016, doi: 10.1007/s41061-016-0060-0.

[17] K. S. Novoselov *et al.*, “Electric field in atomically thin carbon films,” *Science (1979)*, vol. 306, no. 5696, pp. 666–669, Oct. 2004, doi: 10.1126/science.1102896/suppl_file/novoselov.som.pdf.

[18] D. D. L. Chung, “Review Graphite,” *Journal of Materials Science 2002 37:8*, vol. 37, no. 8, pp. 1475–1489, Apr. 2002, doi: 10.1023/a:1014915307738.

[19] A. H. Castro Neto, F. Guinea, N. M. R. Peres, K. S. Novoselov, and A. K. Geim, "The electronic properties of graphene," *Reviews of Modern Physics*, vol. 81, no. 1, pp. 109–162, Jan. 2009, doi: 10.1103/revmodphys.81.109/figures/38/medium.

[20] A. Chaves *et al.*, "Bandgap engineering of two-dimensional semiconductor materials," *npj 2D Materials and Applications 2020 4:1*, vol. 4, no. 1, pp. 1–21, Aug. 2020, doi: 10.1038/s41699-020-00162-4.

[21] C. Zhu, D. Du, and Y. Lin, "Graphene-like 2D nanomaterial-based biointerfaces for biosensing applications," *Biosensors and Bioelectronics*, vol. 89, pp. 43–55, Mar. 2017, doi: 10.1016/j.bios.2016.06.045.

[22] H. Zhang, "Ultrathin Two-Dimensional Nanomaterials," *ACS Nano*, vol. 9, no. 10, pp. 9451–9469, Sep. 2015, doi: 10.1021/acsnano.5b05040/asset/images/large/nn-2015-050406_0011.jpeg.

[23] J. Kang, V. K. Sangwan, J. D. Wood, and M. C. Hersam, "Solution-Based Processing of Monodisperse Two-Dimensional Nanomaterials," *Accounts of Chemical Research*, vol. 50, no. 4, pp. 943–951, Apr. 2017, doi: 10.1021/acs.accounts.6b00643/asset/images/large/ar-2016-006436_0007.jpeg.

[24] A. Jayakumar, A. Surendranath, and M. PV, "2D materials for next generation healthcare applications," *International Journal of Pharmaceutics*, vol. 551, no. 1–2, pp. 309–321, Nov. 2018, doi: 10.1016/j.ijpharm.2018.09.041.

[25] X. Bao, Q. Ou, Z. Q. Xu, Y. Zhang, Q. Bao, and H. Zhang, "Band Structure Engineering in 2D Materials for Optoelectronic Applications," *Advanced Materials Technologies*, vol. 3, no. 11, p. 1800072, Nov. 2018, doi: 10.1002/admt.201800072.

[26] S. Cao *et al.*, "Photoelectrochemical sensors based on heterogeneous nanostructures for in vitro diagnostics," *Biosensors and Bioelectronics: X*, vol. 11, p. 100200, Sep. 2022, doi: 10.1016/j.biosx.2022.100200.

[27] M. Z. Qin *et al.*, "2D/2D Heterojunction systems for the removal of organic pollutants: A review," *Advances in Colloid and Interface Science*, vol. 297, p. 102540, Nov. 2021, doi: 10.1016/j.cis.2021.102540.

[28] B. Zhu, B. Cheng, J. Fan, W. Ho, and J. Yu, “g-C3N4-Based 2D/2D Composite Heterojunction Photocatalyst,” *Small Structures*, vol. 2, no. 12, p. 2100086, Dec. 2021, doi: 10.1002/sstr.202100086.

[29] J. Low *et al.*, “Heterojunction Photocatalysts,” *Advanced Materials*, vol. 29, no. 20, p. 1601694, May 2017, doi: 10.1002/adma.201601694.

[30] Y. Yan, Z. Zeng, M. Huang, and P. Chen, “Van der waals heterojunctions for catalysis,” *Materials Today Advances*, vol. 6, p. 100059, Jun. 2020, doi: 10.1016/j.mtadv.2020.100059.

[31] G. Sharma *et al.*, “Novel development of nanoparticles to bimetallic nanoparticles and their composites: A review,” *Journal of King Saud University - Science*, vol. 31, no. 2, pp. 257–269, Apr. 2019, doi: 10.1016/j.jksus.2017.06.012.

[32] S. Mondal *et al.*, “Biogenic synthesis of Ag, Au and bimetallic Au/Ag alloy nanoparticles using aqueous extract of mahogany (Swietenia mahogani JACQ.) leaves,” *Colloids and Surfaces B: Biointerfaces*, vol. 82, no. 2, pp. 497–504, Feb. 2011, doi: 10.1016/j.colsurfb.2010.10.007.

[33] S. Khan and M. K. Hossain, “Classification and properties of nanoparticles,” *Nanoparticle-Based Polymer Composites*, pp. 15–54, Jan. 2022, doi: 10.1016/b978-0-12-824272-8.00009-9.

[34] L. H Madkour, “Ecofriendly green biosynthesized of metallic nanoparticles: Bio-reduction mechanism, characterization and pharmaceutical applications in biotechnology industry,” *Global Drugs and Therapeutics*, vol. 3, no. 1, 2017, doi: 10.15761/gdt.1000144.

[35] J. Singh, T. Dutta, K. H. Kim, M. Rawat, P. Samddar, and P. Kumar, “‘Green’ synthesis of metals and their oxide nanoparticles: applications for environmental remediation,” *Journal of Nanobiotechnology 2018 16:1*, vol. 16, no. 1, pp. 1–24, Oct. 2018, doi: 10.1186/s12951-018-0408-4.

[36] U. Pal, J. F. Sánchez-Ramírez, L. Nolasco-Hernández, J. Mendoza-Álvarez, and J. A. Pescador-Rojas, “Synthesis and optical properties of Au-Ag alloy nanoclusters with controlled composition,” *Journal of Nanomaterials*, vol. 2008, no. 1, 2008, doi: 10.1155/2008/620412.

[37] N. Alam, S. Das, • Shaikh Batuta, D. Mandal, • Naznin, and A. Begum, "Green-nanochemistry for safe environment: bio-friendly synthesis of fluorescent monometallic (Ag and Au) and bimetallic (Ag/Au alloy) nanoparticles having pesticide sensing activity," *Journal of Nanostructure in Chemistry 2016 6:4*, vol. 6, no. 4, pp. 373–395, Nov. 2016, doi: 10.1007/s40097-016-0209-y.

[38] D. A. Hashim, A. M. Alwan, and M. F. Jawad, "An investigation of Structural Properties of Monometallic (Ag, Pd) and Bimetallic (Ag@Pd) Nanoparticles Growth on Macro Porous Silicon," *International Journal of Nanoelectronics and Materials*, vol. 11, no. 4, 2018.

[39] J. Fan *et al.*, "Recent Progress on Rational Design of Bimetallic Pd Based Catalysts and Their Advanced Catalysis," *ACS Catalysis*, vol. 10, no. 22, pp. 13560–13583, Nov. 2020, doi: 10.1021/acscatal.0c03280/asset/images/large/cs0c03280_0017.jpeg.

[40] L. Shi *et al.*, "One-step synthesis of Au-pd alloy nanodendrites and their catalytic activity," *Journal of Physical Chemistry C*, vol. 117, no. 24, pp. 12526–12536, Jun. 2013, doi: 10.1021/jp4013202/suppl_file/jp4013202_si_001.pdf.

[41] A. Groß, "Reactivity of Bimetallic Systems Studied from First Principles," *Topics in Catalysis 2006 37:1*, vol. 37, no. 1, pp. 29–39, Mar. 2006, doi: 10.1007/s11244-006-0005-x.

[42] H. C. Ham, G. S. Hwang, J. Han, S. W. Nam, and T. H. Lim, "Geometric parameter effects on ensemble contributions to catalysis: H 2O2 formation from H2 and O2 on AuPd alloys. A first principles study," *Journal of Physical Chemistry C*, vol. 114, no. 35, pp. 14922–14928, Sep. 2010, doi: 10.1021/jp102851d/suppl_file/jp102851d_si_001.pdf.

[43] A. K. Singh and Q. Xu, "Synergistic Catalysis over Bimetallic Alloy Nanoparticles," *ChemCatChem*, vol. 5, no. 3, pp. 652–676, Mar. 2013, doi: 10.1002/cctc.201200591.

[44] "Two metals are better than one | Argonne National Laboratory." https://www.anl.gov/article/two-metals-are-better-than-one (accessed Aug. 05, 2022).

[45] Y. Wang, X. Wang, and M. Antonietti, “Polymeric Graphitic Carbon Nitride as a Heterogeneous Organocatalyst: From Photochemistry to Multipurpose Catalysis to Sustainable Chemistry,” *Angewandte Chemie International Edition*, vol. 51, no. 1, pp. 68–89, Jan. 2012, doi: 10.1002/anie.201101182.

[46] H. Li, L. Wang, Y. Liu, J. Lei, and J. Zhang, “Mesoporous graphitic carbon nitride materials: synthesis and modifications,” *Research on Chemical Intermediates*, vol. 42, no. 5, pp. 3979–3998, May 2016, doi: 10.1007/s11164-015-2294-9/figures/17.

[47] J. LIEBIG, “Uber einige Stickstoff - Verbindungen,” *Annalen der Pharmacie*, vol. 10, no. 1, pp. 1–47, Jan. 1834, doi: 10.1002/jlac.18340100102.

[48] E. C. Franklin, “The ammono carbonic acids,” *J Am Chem Soc*, vol. 44, no. 3, pp. 486–509, Mar. 1922, doi: 10.1021/ja01424a007/asset/ja01424a007.fp.png_v03.

[49] A. I. Shatenshtein, C. Slobutsky, and L. F. Audrieth, “The Structure of Cyameluric Acid, Hydromelonic Acid and Related Substances,” *Proceedings of the National Academy of Sciences*, vol. 23, no. 12, pp. 615–620, Dec. 1937, doi: 10.1073/pnas.23.12.615.

[50] C. E. Redemann and H. J. Lucas, “Some Derivatives of Cyameluric Acid and Probable Structures of Melam, Melem and Melon,” *J Am Chem Soc*, vol. 62, no. 4, pp. 842–846, Apr. 1940, doi: 10.1021/ja01861a038/asset/ja01861a038.fp.png_v03.

[51] M. L. Cohen, “Calculation of bulk moduli of diamond and zinc-blende solids,” *Physical Review B*, vol. 32, no. 12, p. 7988, Dec. 1985, doi: 10.1103/physrevb.32.7988.

[52] A. Y. Liu and M. L. Cohen, “Prediction of New Low Compressibility Solids,” *Science (1979)*, vol. 245, no. 4920, pp. 841–842, Aug. 1989, doi: 10.1126/science.245.4920.841.

[53] M. L. Cohen, “Predicting useful materials,” *Science (1979)*, vol. 261, no. 5119, pp. 307–308, Jul. 1993, doi: 10.1126/science.261.5119.307/asset/a3111ec4-4183-4a1d-ade2-abfad03db4cc/assets/science.261.5119.307.fp.png.

[54] D. M. Teter and R. J. Hemley, “Low-Compressibility Carbon Nitrides,” *Science (1979)*, vol. 271, no. 5245, pp. 53–55, Jan. 1996, doi: 10.1126/science.271.5245.53.

[55] J. L. Corkill and M. L. Cohen, “Calculated quasiparticle band gap of β-C3N4,” *Physical Review B*, vol. 48, no. 23, pp. 17622–17624, Dec. 1993, doi: 10.1103/physrevb.48.17622.

[56] L. Maya, D. R. Cole, and E. W. Hagaman, “Carbon–Nitrogen Pyrolyzates: Attempted Preparation of Carbon Nitride,” *Journal of the American Ceramic Society*, vol. 74, no. 7, pp. 1686–1688, Jul. 1991, doi: 10.1111/J.1151-2916.1991.tb07161.x.

[57] C. Niu, Y. Z. Lu, and C. M. Lieber, “Experimental Realization of the Covalent Solid Carbon Nitride,” *Science (1979)*, vol. 261, no. 5119, pp. 334–337, Jul. 1993, doi: 10.1126/science.261.5119.334.

[58] D. Marton, K. J. Boyd, A. H. Al-Bayati, S. S. Todorov, and J. W. Rabalais, “Carbon Nitride Deposited Using Energetic Species: A Two-Phase System,” *Physical Review Letters*, vol. 73, no. 1, p. 118, Jul. 1994, doi: 10.1103/physrevlett.73.118.

[59] Yu, K. M., Cohen, M. L., Haller, E. E., Hansen, W. L., Liu, A. Y., & Wu, I. C. (1994). Observation of crystalline C3N4. Physical review. B, Condensed matter, 49(7), 5034–5037. https://doi.org/10.1103/physrevb.49.5034

[60] J. P. Rivière, D. Texier, J. Delafond, M. Jaouen, E. L. Mathé, and J. Chaumont, “Formation of the crystalline β-C3N4 phase by dual ion beam sputtering deposition,” *Materials Letters*, vol. 22, no. 1–2, pp. 115–118, Jan. 1995, doi: 10.1016/0167-577x(94)00233-9.

[61] Z. M. Ren *et al.*, “Carbon nitride films synthesized by combined ion-beam and laser-ablation processing,” *Physical Review B*, vol. 51, no. 8, p. 5274, Feb. 1995, doi: 10.1103/physrevb.51.5274.

[62] D. C. Nesting and J. v. Badding, “High-Pressure Synthesis of sp2-Bonded Carbon Nitrides,” *Chemistry of Materials*, vol. 8, no. 7, pp. 1535–1539, 1996, doi: 10.1021/cm9601289/asset/images/medium/cm9601289e00001.gif.

[63] A. Y. Liu and R. M. Wentzcovitch, “Stability of carbon nitride solids,” *Physical Review B*, vol. 50, no. 14, p. 10362, Oct. 1994, doi: 10.1103/physrevb.50.10362.

[64] J. E. Lowther, “Relative stability of some possible phases of graphitic carbon nitride,” *Physical Review B*, vol. 59, no. 18, p. 11683, May 1999, doi: 10.1103/physrevb.59.11683.

[65] J. Ortega and O. F. Sankey, “Relative stability of hexagonal and planar structures of hypothetical C&N4 solids”, *Physical Review B*, vol. 51, no. 4, p. 2624, Jan. 1995, doi: 10.1103/PhysRevB.51.2624.

[66] T. Komatsu, “Prototype carbon nitrides similar to the symmetrictriangular form of melon,” *Journal of Materials Chemistry*, vol. 11, no. 3, pp. 802–803, Jan. 2001, doi: 10.1039/b007165j.

[67] B. Jürgens, E. Irran, J. Senker, P. Kroll, H. Müller, and W. Schnick, “Melem (2,5,8-triamino-tri-s-triazine), an important intermediate during condensation of melamine rings to graphitic carbon nitride: Synthesis, structure determination by x-ray powder diffractometry, solid-state NMR, and theoretical studies,” *J Am Chem Soc*, vol. 125, no. 34, pp. 10288–10300, Aug. 2003, doi: 10.1021/ja0357689/suppl_file/ja0357689si20030429_062527.cif.

[68] A. Sattler and W. Schnick, “Zur Kenntnis der Kristallstruktur von Melem C6N7(NH2)3,” *Zeitschrift für anorganische und allgemeine Chemie*, vol. 632, no. 2, pp. 238–242, Jan. 2006, doi: 10.1002/zaac.200500363.

[69] S. Eken Korkut, H. Küçükkeçeci, and Ö. Metin, “Mesoporous Graphitic Carbon Nitride/Black Phosphorus/AgPd Alloy Nanoparticles Ternary Nanocomposite: A Highly Efficient Catalyst for the Methanolysis of Ammonia Borane,” *ACS Applied Materials and Interfaces*, vol. 12, no. 7, pp. 8130–8139, Feb. 2020, doi: 10.1021/acsami.9b18917/asset/images/large/am9b18917_0009.jpeg.

[70] E. Horvath-Bordon *et al.*, “High-Pressure Synthesis of Crystalline Carbon Nitride Imide, C2N2(NH),” *Angewandte Chemie*, vol. 119, no. 9, pp. 1498–1502, Feb. 2007, doi: 10.1002/ange.200603851.

[71] S. P. Sun, S. Gu, J. H. Sun, F. F. Xia, and G. H. Chen, “First principles investigation of the electronic properties of graphitic carbon nitride with different building block

and sheet staggered arrangement," *Journal of Alloys and Compounds*, vol. 735, pp. 131–139, Feb. 2018, doi: 10.1016/j.jallcom.2017.11.061.

[72] M. Aksoy and Ö. Metin, "Pt Nanoparticles Supported on Mesoporous Graphitic Carbon Nitride as Catalysts for Hydrolytic Dehydrogenation of Ammonia Borane," *ACS Applied Nano Materials*, vol. 3, no. 7, pp. 6836–6846, Jul. 2020, doi: 10.1021/acsanm.0c01208/asset/images/large/an0c01208_0010.jpeg.

[73] L. Shen *et al.*, "Black TiO2 nanobelts/g-C3N4 nanosheets Laminated Heterojunctions with Efficient Visible-Light-Driven Photocatalytic Performance," *Scientific Reports 2017 7:1*, vol. 7, no. 1, pp. 1–11, Feb. 2017, doi: 10.1038/srep41978.

[74] A. Jabbari, H. Mahdavi, M. Nikoorazm, and A. Ghorbani-Choghamarani, "Salen copper(II) complex heterogenized on mesoporous MCM-41 as nano-reactor catalyst for the selective oxidation of sulfides using urea hydrogen peroxide (UHP)," *Research on Chemical Intermediates*, vol. 41, no. 8, pp. 5649–5663, Aug. 2015, doi: 10.1007/s11164-014-1690-x/figures/8.

[75] J. Lei *et al.*, "Carbon Dot-Incorporated PMO Nanoparticles as Versatile Platforms for the Design of Ratiometric Sensors, Multichannel Traceable Drug Delivery Vehicles, and Efficient Photocatalysts," *Advanced Optical Materials*, vol. 3, no. 1, pp. 57–63, Jan. 2015, doi: 10.1002/adom.201400364.

[76] J. Lei, L. Wang, and J. Zhang, "Superbright multifluorescent core - Shell mesoporous nanospheres as trackable transport carrier for drug," *ACS Nano*, vol. 5, no. 5, pp. 3447–3455, May 2011, doi: 10.1021/nn103254g/suppl_file/nn103254g_si_001.pdf.

[77] J. Lei, L. Wang, and J. Zhang, "Ratiometric pH sensor based on mesoporous silica nanoparticles and Förster resonance energy transfer," *Chemical Communications*, vol. 46, no. 44, pp. 8445–8447, Nov. 2010, doi: 10.1039/c0cc03310c.

[78] S. Xiao *et al.*, "Intramolecular cyclization of N-phenylanthranilic acid catalyzed by MCM-41 with different pore diameters," *Research on Chemical Intermediates*, vol. 41, no. 12, pp. 10125–10135, Dec. 2015, doi: 10.1007/s11164-015-2017-2/figures/10.

[79] J. Xu, H. T. Wu, X. Wang, B. Xue, Y. X. Li, and Y. Cao, “A new and environmentally benign precursor for the synthesis of mesoporous g-C3N4 with tunable surface area,” *Physical Chemistry Chemical Physics*, vol. 15, no. 13, pp. 4510–4517, Mar. 2013, doi: 10.1039/c3cp44402c.

[80] J. Cui, S. Liang, S. Sun, X. Zheng, and J. Zhang, “Enhanced photocatalytic property of hybrid graphitic C3N4 and graphitic ZnO nanocomposite: the effects of interface and doping,” *Journal of Physics: Condensed Matter*, vol. 30, no. 17, p. 175001, Apr. 2018, doi: 10.1088/1361-648x/aab511.

[81] S. Sun and S. Liang, “Recent advances in functional mesoporous graphitic carbon nitride (mpg-C3N4) polymers,” *Nanoscale*, vol. 9, no. 30, pp. 10544–10578, Aug. 2017, doi: 10.1039/c7nr03656f.

[82] W. Wang, J. C. Yu, Z. Shen, D. K. L. Chan, and T. Gu, “g-C3N4 quantum dots: direct synthesis, upconversion properties and photocatalytic application,” *Chemical Communications*, vol. 50, no. 70, pp. 10148–10150, Aug. 2014, doi: 10.1039/c4cc02543a.

[83] C. Cao, F. Huang, C. Cao, J. Li, and H. Zhu, “Synthesis of carbon nitride nanotubes via a catalytic-assembly solvothermal route,” *Chemistry of Materials*, vol. 16, no. 25, pp. 5213–5215, Dec. 2004, doi: 10.1021/cm0493039/suppl_file/cm0493039si20040912_051214.pdf.

[84] X. Du, G. Zou, Z. Wang, and X. Wang, “A scalable chemical route to soluble acidified graphitic carbon nitride: an ideal precursor for isolated ultrathin g-C3N4 nanosheets,” *Nanoscale*, vol. 7, no. 19, pp. 8701–8706, May 2015, doi: 10.1039/c5nr00665a.

[85] M. Groenewolt and M. Antonietti, “Synthesis of g-C3N4 Nanoparticles in Mesoporous Silica Host Matrices,” *Advanced Materials*, vol. 17, no. 14, pp. 1789–1792, Jul. 2005, doi: 10.1002/adma.200401756.

[86] E. G. Gillan, “Synthesis of nitrogen-rich carbon nitride networks from an energetic molecular azide precursor,” *Chemistry of Materials*, vol. 12, no. 12, pp. 3906–3912, 2000, doi: 10.1021/cm000570y/suppl_file/cm000570y_s.pdf.

[87] S. C. Yan, Z. S. Li, and Z. G. Zou, “Photodegradation performance of g-C3N4 fabricated by directly heating melamine,” *Langmuir*, vol. 25, no. 17, pp. 10397–10401, Sep. 2009, doi: 10.1021/la900923z/suppl_file/la900923z_si_001.pdf.

[88] A. Thomas *et al.*, “Graphitic carbon nitride materials: variation of structure and morphology and their use as metal-free catalysts,” *Journal of Materials Chemistry*, vol. 18, no. 41, pp. 4893–4908, Oct. 2008, doi: 10.1039/b800274f.

[89] R. Paduch, M. Kandefer-Szerszeń, M. Trytek, and J. Fiedurek, “Terpenes: substances useful in human healthcare,” *Archivum Immunologiae et Therapiae Experimentalis 2007 55:5*, vol. 55, no. 5, pp. 315–327, Oct. 2007, doi: 10.1007/s00005-007-0039-1.

[90] E. ALDRED, “Terpenes,” *Pharmacology*, pp. 167–174, Jan. 2009, doi: 10.1016/b978-0-443-06898-0.00022-0.

[91] F. Vinale, K. Sivasithamparam, S. Zeilinger, and S. Gutiérrez, “Fungal Secondary Metabolism,” *Encyclopedia of Mycology*, pp. 54–63, Jan. 2021, doi: 10.1016/b978-0-12-819990-9.00031-7.

[92] G. Richter, T. Hazzah, J. A. Hartsel, J. Eades, B. Hickory, and A. Makriyannis, “Cannabis sativa: an overview,” *Nutraceuticals: Efficacy, Safety and Toxicity*, pp. 603–624, Jan. 2021, doi: 10.1016/b978-0-12-821038-3.00038-0.

[93] S. Howe, “Raw materials,” *The Craft Brewing Handbook*, pp. 1–46, Jan. 2020, doi: 10.1016/b978-0-08-102079-1.00001-1.

[94] J. L. F. Monteiro and C. O. Veloso, “Catalytic Conversion of Terpenes into Fine Chemicals,” *Topics in Catalysis 2004 27:1*, vol. 27, no. 1, pp. 169–180, 2004, doi: 10.1023/b:toca.0000013551.99872.8d.

[95] C. C. C. R. de Carvalho and M. M. R. da Fonseca, “Carvone: Why and how should one bother to produce this terpene,” *Food Chemistry*, vol. 95, no. 3, pp. 413–422, Apr. 2006, doi: 10.1016/j.foodchem.2005.01.003.

[96] B. S. Reddy *et al.*, “Chemoprevention of colon carcinogenesis by dietary perillyl alcohol.,” *Cancer Res*, vol. 57, no. 3, pp. 420–5, Feb. 1997.

[97] R. P. Linstead, K. O. A. Michaelis, and S. L. S. Thomas, “210. Dehydrogenation. Part IV. Catalytic disproportionation and dehydrogenation of some terpenes and

terpene ketones," *Journal of the Chemical Society (Resumed)*, no. 0, pp. 1139–1147, Jan. 1940, doi: 10.1039/jr9400001139.

[98] E. F. Armstrong and T. P. H. Ilditch, "A study of catalytic actions at solid surfaces. Part XIII.—Some factors controlling selective hydrogenation, with particular reference to certain terpene derivatives," *Proceedings of the Royal Society of London. Series A, Containing Papers of a Mathematical and Physical Character*, vol. 108, no. 745, pp. 121–131, May 1925, doi: 10.1098/rspa.1925.0063.

[99] V. Ponec and G. C. (Geoffrey C. Bond, "Catalysis by metals and alloys," p. 734, 1995.

[100] L. S. Benner, T. Suzuki, K. Meguro, and S. Tanaka, *Precious metals: science and technology*. Allentown PA: Int. Prec. Met. Inst, 1991.

[101] P. B. Kettler, "Platinum group metals in catalysis: Fabrication of catalysts and catalyst precursors," *Organic Process Research and Development*, vol. 7, no. 3, pp. 342–354, 2003, doi: 10.1021/op034017o/asset/images/large/op034017oh00010.jpeg.

[102] J. Fan *et al.*, "Recent Progress on Rational Design of Bimetallic Pd Based Catalysts and Their Advanced Catalysis," *ACS Catalysis*, vol. 10, no. 22, pp. 13560–13583, Nov. 2020, doi: 10.1021/acscatal.0c03280/asset/images/large/cs0c03280_0017.jpeg.

[103] F. Liao, T. W. B. Lo, and S. C. E. Tsang, "Recent Developments in Palladium-Based Bimetallic Catalysts," *ChemCatChem*, vol. 7, no. 14, pp. 1998–2014, Jul. 2015, doi: 10.1002/cctc.201500245.

[104] N. Miyaura and A. Suzuki, "Palladium-Catalyzed Cross-Coupling Reactions of Organoboron Compounds," *Chemical Reviews*, vol. 95, no. 7, pp. 2457–2483, 1995, doi: 10.1021/cr00039a007/asset/cr00039a007.fp.png_v03.

[105] H. Li, C. C. C. Johansson Seechurn, and T. J. Colacot, "Development of preformed Pd catalysts for cross-coupling reactions, beyond the 2010 nobel prize," *ACS Catalysis*, vol. 2, no. 6, pp. 1147–1164, Jun. 2012, doi: 10.1021/cs300082f/asset/images/medium/cs-2012-00082f_0024.gif.

[106] J. Wildschut, F. H. Mahfud, R. H. Venderbosch, and H. J. Heeres, “Hydrotreatment of fast pyrolysis oil using heterogeneous noble-metal catalysts,” *Industrial and Engineering Chemistry Research*, vol. 48, no. 23, pp. 10324–10334, 2009, doi: 10.1021/ie9006003/asset/images/medium/ie-2009-006003_0012.gif.

[107] R. J. Bunting, X. Cheng, J. Thompson, and P. Hu, “Amorphous Surface PdO X and Its Activity toward Methane Combustion,” *ACS Catalysis*, vol. 9, no. 11, pp. 10317–10323, Nov. 2019, doi: 10.1021/acscatal.9b01942/suppl_file/cs9b01942_si_002.cif.

[108] Y. QIN, “Stabilization of Active Structures of Pd catalysts for Methane Combustion by Al2O3 Overlayers,” *Acta Physico-Chimica Sinica*, vol. 35, no. 12, pp. 1305–1306, 2019, doi: 10.3866/pku.whxb201906082.

[109] G. Spezzati *et al.*, “CO oxidation by Pd supported on CeO2(100) and CeO2(111) facets,” *Applied Catalysis B: Environmental*, vol. 243, pp. 36–46, Apr. 2019, doi: 10.1016/j.apcatb.2018.10.015.

[110] D. I. Enache *et al.*, “Solvent-free oxidation of primary alcohols to aldehydes using Au-Pd/TiO2 catalyst,” *Science (1979)*, vol. 311, no. 5759, pp. 362–365, Jan. 2006, doi: 10.1126/science.1120560/suppl_file/enache.som.pdf.

[111] J. Feng *et al.*, “Au–Pd nanoalloys supported on Mg–Al mixed metal oxides as a multifunctional catalyst for solvent-free oxidation of benzyl alcohol,” *Dalton Transactions*, vol. 42, no. 40, pp. 14498–14508, Sep. 2013, doi: 10.1039/c3dt51855h.

[112] G. Vilé, D. Albani, N. Almora-Barrios, N. López, and J. Pérez-Ramírez, “Advances in the Design of Nanostructured Catalysts for Selective Hydrogenation,” *ChemCatChem*, vol. 8, no. 1, pp. 21–33, Jan. 2016, doi: 10.1002/cctc.201501269.

[113] C. W. A. Chan *et al.*, “Interstitial modification of palladium nanoparticles with boron atoms as a green catalyst for selective hydrogenation,” *Nature Communications 2014 5:1*, vol. 5, no. 1, pp. 1–10, Dec. 2014, doi: 10.1038/ncomms6787.

[114] Z. Ma, Z. Wu, and J. T. Miller, “Effect of Cu content on the bimetallic Pt–Cu catalysts for propane dehydrogenation,”

https://doi.org/10.1080/2055074X.2016.1263177, vol. 3, no. 1–2, pp. 43–53, Apr. 2017, doi: 10.1080/2055074x.2016.1263177.

[115] M. Aksoy, H. Kilic, B. Nisanci, and Ö. Metin, "Recent advances in the development of palladium nanocatalysts for sustainable organic transformations," *Inorganic Chemistry Frontiers*, vol. 8, no. 2, pp. 499–545, Jan. 2021, doi: 10.1039/d0qi01283a.

[116] D. Wang and Y. Li, "Bimetallic Nanocrystals: Liquid-Phase Synthesis and Catalytic Applications," *Advanced Materials*, vol. 23, no. 9, pp. 1044–1060, Mar. 2011, doi: 10.1002/adma.201003695.

[117] M. Sankar, N. Dimitratos, P. J. Miedziak, P. P. Wells, C. J. Kiely, and G. J. Hutchings, "Designing bimetallic catalysts for a green and sustainable future," *Chemical Society Reviews*, vol. 41, no. 24, pp. 8099–8139, Nov. 2012, doi: 10.1039/c2cs35296f.

[118] L. Zhang, Z. Xie, and J. Gong, "Shape-controlled synthesis of Au–Pd bimetallic nanocrystals for catalytic applications," *Chemical Society Reviews*, vol. 45, no. 14, pp. 3916–3934, Jul. 2016, doi: 10.1039/c5cs00958h.

[119] Z. W. She, J. Kibsgaard, C. F. Dickens, I. Chorkendorff, J. K. Nørskov, and T. F. Jaramillo, "Combining theory and experiment in electrocatalysis: Insights into materials design," *Science (1979)*, vol. 355, no. 6321, Jan. 2017, doi: 10.1126/science.aad4998/asset/456d2edc-7985-473d-9ce8-06020de97887/assets/graphic/355_aad4998_fa.jpeg.

[120] P. Liu and J. K. Nørskov, "Ligand and ensemble effects in adsorption on alloy surfaces," *Physical Chemistry Chemical Physics*, vol. 3, no. 17, pp. 3814–3818, Jan. 2001, doi: 10.1039/b103525h.

[121] K. W. Park *et al.*, "Chemical and electronic effects of Ni in Pt/Ni and Pt/Ru/Ni alloy nanoparticles in methanol electrooxidation," *Journal of Physical Chemistry B*, vol. 106, no. 8, pp. 1869–1877, Feb. 2002, doi: 10.1021/jp013168v/asset/images/large/jp013168vf00011.jpeg.

[122] H. Li, K. Shin, and G. Henkelman, "Effects of ensembles, ligand, and strain on adsorbate binding to alloy surfaces," *The Journal of Chemical Physics*, vol. 149, no. 17, p. 174705, Nov. 2018, doi: 10.1063/1.5053894.

[123] N. Schweitzer, H. Xin, E. Nikolla, J. T. Miller, and S. Linic, "Establishing relationships between the geometric structure and chemical reactivity of alloy catalysts based on their measured electronic structure," *Topics in Catalysis*, vol. 53, no. 5–6, pp. 348–356, May 2010, doi: 10.1007/s11244-010-9448-1/figures/5.

[124] J. K. Nørskov, T. Bligaard, J. Rossmeisl, and C. H. Christensen, "Towards the computational design of solid catalysts," *Nature Chemistry 2009 1:1*, vol. 1, no. 1, pp. 37–46, Apr. 2009, doi: 10.1038/nchem.121.

[125] W. Nie, Y. Luo, Q. Yang, G. Feng, Q. Yao, and Z. H. Lu, "An amine-functionalized mesoporous silica-supported PdIr catalyst: boosting room-temperature hydrogen generation from formic acid," *Inorganic Chemistry Frontiers*, vol. 7, no. 3, pp. 709–717, Feb. 2020, doi: 10.1039/c9qi01375j.

[126] J. Bai *et al.*, "Component-Dependent Electrocatalytic Activity of Ultrathin PdRh Alloy Nanocrystals for the Formate Oxidation Reaction," *ACS Sustainable Chemistry and Engineering*, vol. 7, no. 2, pp. 2830–2836, Jan. 2019, doi: 10.1021/acssuschemeng.8b06193/asset/images/large/sc-2018-06193n_0007.jpeg.

[127] R. Hong, Y. He, J. Feng, and D. Li, "Fabrication of supported Pd–Ir/Al2O3 bimetallic catalysts for 2-ethylanthraquinone hydrogenation," *AIChE Journal*, vol. 63, no. 9, pp. 3955–3965, Sep. 2017, doi: 10.1002/aic.15748.

[128] H. Wang *et al.*, "Enhancing formic acid dehydrogenation for hydrogen production with the metal/organic interface," *Applied Catalysis B: Environmental*, vol. 255, p. 117776, Oct. 2019, doi: 10.1016/j.apcatb.2019.117776.

[129] L. Rößner and M. Armbrüster, "Electrochemical Energy Conversion on Intermetallic Compounds: A Review," *ACS Catalysis*, vol. 9, no. 3, pp. 2018–2062, Mar. 2019, doi: 10.1021/acscatal.8b04566/asset/images/large/cs-2018-04566z_0012.jpeg.

[130] Y. Peng *et al.*, "Bimetallic Composition-Promoted Electrocatalytic Hydrodechlorination Reaction on Silver-Palladium Alloy Nanoparticles," *ACS Catalysis*, pp. 10803–10811, 2019, doi: 10.1021/acscatal.9b02282/asset/images/large/cs9b02282_0008.jpeg.

[131] Z. P. Wu *et al.*, "Revealing the Role of Phase Structures of Bimetallic Nanocatalysts in the Oxygen Reduction Reaction," *ACS Catalysis*, vol. 8, no. 12,

pp. 11302–11313, Dec. 2018, doi: 10.1021/acscatal.8b03106/asset/images/large/cs-2018-03106e_0008.jpeg.

[132] S. Han, K. Shin, G. Henkelman, and C. Buddie Mullins, "Selective Oxidation of Acetaldehyde to Acetic Acid on Pd-Au Bimetallic Model Catalysts," *ACS Catalysis*, vol. 9, no. 5, pp. 4360–4368, May 2019, doi: 10.1021/acscatal.9b00079/asset/images/large/cs-2019-00079y_0007.jpeg.

[133] J. H. Lee *et al.*, "Experimental and computational studies of formic acid dehydrogenation over PdAu: influence of ensemble and ligand effects on catalysis," *Journal of Materials Chemistry A*, vol. 4, no. 37, pp. 14141–14147, Sep. 2016, doi: 10.1039/c6ta03654f.

[134] M. Guo, J. Peng, Q. Yang, and C. Li, "Highly Active and Selective RuPd Bimetallic NPs for the Cleavage of the Diphenyl Ether C-O Bond," *ACS Catalysis*, vol. 8, no. 12, pp. 11174–11183, Dec. 2018, doi: 10.1021/acscatal.8b03253/asset/images/medium/cs-2018-03253u_m005.gif.

[135] D. M. Sedgwick and G. B. Hammond, "The history and future challenges associated with the hydrogenation of vinyl fluorides," *Journal of Fluorine Chemistry*, vol. 207, pp. 45–58, Mar. 2018, doi: 10.1016/j.jfluchem.2017.12.019.

[136] S. Trasatti, "Work function, electronegativity, and electrochemical behaviour of metals: III. Electrolytic hydrogen evolution in acid solutions," *Journal of Electroanalytical Chemistry and Interfacial Electrochemistry*, vol. 39, no. 1, pp. 163–184, Sep. 1972, doi: 10.1016/s0022-0728(72)80485-6.

[137] J. A. Widegren and R. G. Finke, "A review of soluble transition-metal nanoclusters as arene hydrogenation catalysts," *Journal of Molecular Catalysis A: Chemical*, vol. 191, no. 2, pp. 187–207, Jan. 2003, doi: 10.1016/s1381-1169(02)00125-5.

[138] R. L. Augustine, Ed., *Heterogeneous Catalysis for the Synthetic Chemist*. New York: Marcel Dekker, 1996.

[139] "Industrial Catalysis: A Practical Approach, 2nd Edition | Wiley." https://www.wiley.com/en-us/Industrial+Catalysis:+A+Practical+Approach,+2nd+Edition-p-9783527311446 (accessed Aug. 05, 2022).

[140] P. N. Rylander, “Catalytic hydrogenation over platinum metals,” p. 550, 1967.

[141] H. Greenfield, “STUDIES IN NUCLEAR HYDROGENATION,” *Ann N Y Acad Sci*, vol. 214, no. 1, pp. 233–242, Jun. 1973, doi: 10.1111/j.1749-6632.1973.tb49536.x.

[142] B. Yoon, H. bin Pan, and C. M. Wai, “Relative catalytic activities of carbon nanotube-supported metallic nanoparticles for room-temperature hydrogenation of benzene,” *Journal of Physical Chemistry C*, vol. 113, no. 4, pp. 1520–1525, Jan. 2009, doi: 10.1021/jp809366w/suppl_file/jp809366w_si_001.pdf.

[143] A. A. Lamberov *et al.*, “Changes in the course of reaction and regeneration of a Pd-Ag/Al2O3 catalyst for the selective hydrogenation of acetylene,” *Kinetics and Catalysis 2007 48:1*, vol. 48, no. 1, pp. 136–142, Feb. 2007, doi: 10.1134/s0023158407010181.

[144] B. Coq and F. Figueras, “Bimetallic palladium catalysts: influence of the co-metal on the catalyst performance,” *Journal of Molecular Catalysis A: Chemical*, vol. 173, no. 1–2, pp. 117–134, Sep. 2001, doi: 10.1016/s1381-1169(01)00148-0.

[145] D. Mei, M. Neurock, and C. M. Smith, “Hydrogenation of acetylene–ethylene mixtures over Pd and Pd–Ag alloys: First-principles-based kinetic Monte Carlo simulations,” *Journal of Catalysis*, vol. 268, no. 2, pp. 181–195, Dec. 2009, doi: 10.1016/j.jcat.2009.09.004.

[146] T. v. Choudhary, C. Sivadinarayana, A. K. Datye, D. Kumar, and D. W. Goodman, “Acetylene Hydrogenation on Au-Based Catalysts,” *Catalysis Letters 2003 86:1*, vol. 86, no. 1, pp. 1–8, Mar. 2003, doi: 10.1023/a:1022694505504.

[147] G. A. Olah, “Beyond Oil and Gas: The Methanol Economy,” *Angewandte Chemie International Edition*, vol. 44, no. 18, pp. 2636–2639, Apr. 2005, doi: 10.1002/anie.200462121.

[148] J. Turner *et al.*, “Renewable hydrogen production,” *International Journal of Energy Research*, vol. 32, no. 5, pp. 379–407, Apr. 2008, doi: 10.1002/er.1372.

[149] “Handbook of Homogeneous Hydrogenation, 3 Volume Set | Wiley.” https://www.wiley.com/en-

us/Handbook+of+Homogeneous+Hydrogenation%2C+3+Volume+Set-p-9783527311613 (accessed Aug. 05, 2022).

[150] T. Sakakura, J. C. Choi, and H. Yasuda, "Transformation of carbon dioxide," *Chemical Reviews*, vol. 107, no. 6, pp. 2365–2387, Jun. 2007, doi: 10.1021/cr068357u/asset/images/medium/cr068357uh00039.gif.

[151] F. Liao *et al.*, "Electronic Modulation of a Copper/Zinc Oxide Catalyst by a Heterojunction for Selective Hydrogenation of Carbon Dioxide to Methanol," *Angewandte Chemie*, vol. 124, no. 24, pp. 5934–5938, Jun. 2012, doi: 10.1002/ange.201200903.

[152] T. Fitzpatrick, "Synthesis of Methanol: Part 1. Catalysts and Kinetics," *Applied Catalysis*, vol. 36, no. 9, pp. 1–65, Jan. 1988, doi: 10.1016/s0166-9834(00)80103-7.

[153] M. Fernández-García, J. A. Anderson, and G. L. Haller, "Alloy formation and stability in Pd-Cu bimetallic catalysts," *Journal of Physical Chemistry*, vol. 100, no. 40, pp. 16247–16254, Oct. 1996, doi: 10.1021/jp9608133/asset/images/large/jp9608133f00009.jpeg.

[154] J. L. G. Fierro, I. Melián-Cabrera, and M. López Granados, "Pd-Modified Cu–Zn Catalysts for Methanol Synthesis from CO2/H2 Mixtures: Catalytic Structures and Performance," *Journal of Catalysis*, vol. 210, no. 2, pp. 285–294, Sep. 2002, doi: 10.1006/jcat.2002.3677.

[155] A. L. Bonivardi, D. L. Chiavassa, C. A. Querini, and M. A. Baltanás, "Enhancement of the catalytic performance to methanol synthesis from CO2/H2 by gallium addition to palladium/silica catalysts," *Studies in Surface Science and Catalysis*, vol. 130, pp. 3747–3752, Jan. 2000, doi: 10.1016/s0167-2991(00)80606-0.

[156] J. G. Speight, "Industrial Organic Chemistry," *Environmental Organic Chemistry for Engineers*, pp. 87–151, Jan. 2017, doi: 10.1016/b978-0-12-804492-6.00003-4.

[157] T. C. Johnson, D. J. Morris, and M. Wills, "Hydrogen generation from formic acid and alcohols using homogeneous catalysts," *Chemical Society Reviews*, vol. 39, no. 1, pp. 81–88, Dec. 2009, doi: 10.1039/b904495g.

[158] F. Joó, “Breakthroughs in Hydrogen Storage—Formic Acid as a Sustainable Storage Material for Hydrogen,” *ChemSusChem*, vol. 1, no. 10, pp. 805–808, Oct. 2008, doi: 10.1002/cssc.200800133.

[159] B. Loges, A. Boddien, F. Gärtner, H. Junge, and M. Beller, “Catalytic generation of hydrogen from formic acid and its derivatives: Useful hydrogen storage materials,” *Topics in Catalysis*, vol. 53, no. 13–14, pp. 902–914, Aug. 2010, doi: 10.1007/s11244-010-9522-8/figures/3.

[160] X. Zhou, Y. Huang, W. Xing, C. Liu, J. Liao, and T. Lu, “High-quality hydrogen from the catalyzed decomposition of formic acid by Pd–Au/C and Pd–Ag/C,” *Chemical Communications*, no. 30, pp. 3540–3542, Jul. 2008, doi: 10.1039/b803661f.

[161] Ö. Metin, X. Sun, and S. Sun, “Monodisperse gold–palladium alloy nanoparticles and their composition-controlled catalysis in formic acid dehydrogenation under mild conditions,” *Nanoscale*, vol. 5, no. 3, pp. 910–912, Jan. 2013, doi: 10.1039/c2nr33637e.

[162] N. Akiya and P. E. Savage, “Role of water in formic acid decomposition,” *AIChE Journal*, vol. 44, no. 2, pp. 405–415, Feb. 1998, doi: 10.1002/aic.690440217.

[163] X. Gu, Z. H. Lu, H. L. Jiang, T. Akita, and Q. Xu, “Synergistic catalysis of metal-organic framework-immobilized au-pd nanoparticles in dehydrogenation of formic acid for chemical hydrogen storage,” *J Am Chem Soc*, vol. 133, no. 31, pp. 11822–11825, Aug. 2011, doi: 10.1021/ja200122f/suppl_file/ja200122f_si_001.pdf.

[164] S. Zhang *et al.*, “Monodisperse AgPd Alloy Nanoparticles and Their Superior Catalysis for the Dehydrogenation of Formic Acid,” *Angewandte Chemie*, vol. 125, no. 13, pp. 3769–3772, Mar. 2013, doi: 10.1002/ange.201300276.

[165] K. S. Kim and M. A. Barteau, “Structural Dependence of the Selectivity of Formic Acid Decomposition on Faceted TiO2 (001) Surfaces,” *Langmuir*, vol. 6, no. 9, pp. 1485–1488, 1990, doi: 10.1021/la00099a009/asset/la00099a009.fp.png_v03.

[166] N. Hoshi, M. Nakamura, and K. Kida, “Structural effects on the oxidation of formic acid on the high index planes of palladium,” *Electrochemistry Communications*, vol. 9, no. 2, pp. 279–282, Feb. 2007, doi: 10.1016/j.elecom.2006.09.023.

[167] Y. Liu, J. Goebl, and Y. Yin, “Templated synthesis of nanostructured materials,” *Chemical Society Reviews*, vol. 42, no. 7, pp. 2610–2653, Mar. 2013, doi: 10.1039/c2cs35369e.

[168] S. Sun and Z. Yang, “Cu2O-templated strategy for synthesis of definable hollow architectures,” *Chemical Communications*, vol. 50, no. 56, pp. 7403–7415, Jun. 2014, doi: 10.1039/c4cc00304g.

[169] C. Pan, J. Xu, Y. Wang, D. Li, and Y. Zhu, “Dramatic Activity of C3N4/BiPO4 Photocatalyst with Core/Shell Structure Formed by Self-Assembly,” *Advanced Functional Materials*, vol. 22, no. 7, pp. 1518–1524, Apr. 2012, doi: 10.1002/adfm.201102306.

[170] X. H. Li and M. Antonietti, “Metal nanoparticles at mesoporous N-doped carbons and carbon nitrides: functional Mott–Schottky heterojunctions for catalysis,” *Chemical Society Reviews*, vol. 42, no. 16, pp. 6593–6604, Jul. 2013, doi: 10.1039/c3cs60067j.

[171] P. Munnik, P. E. de Jongh, and K. P. de Jong, “Recent Developments in the Synthesis of Supported Catalysts,” *Chemical Reviews*, vol. 115, no. 14, pp. 6687–6718, Jul. 2015, doi: 10.1021/cr500486u/asset/images/large/cr-2014-00486u_0029.jpeg.

[172] Y. Di, X. Wang, A. Thomas, and M. Antonietti, “Making Metal-Carbon Nitride Heterojunctions for Improved Photocatalytic Hydrogen Evolution with Visible Light,” *ChemCatChem*, vol. 2, no. 7, pp. 834–838, Jun. 2010, doi: 10.1002/cctc.201000057.

[173] R. Li *et al.*, “Spatial separation of photogenerated electrons and holes among {010} and {110} crystal facets of BiVO4,” *Nature Communications 2013 4:1*, vol. 4, no. 1, pp. 1–7, Feb. 2013, doi: 10.1038/ncomms2401.

[174] X. Meng *et al.*, “Photothermal Conversion of CO2 into CH4 with H2 over Group VIII Nanocatalysts: An Alternative Approach for Solar Fuel Production,” *Angewandte Chemie International Edition*, vol. 53, no. 43, pp. 11478–11482, Oct. 2014, doi: 10.1002/anie.201404953.

[175] S. Cao and J. Yu, “G-C3N4-based photocatalysts for hydrogen generation,” *Journal of Physical Chemistry Letters*, vol. 5, no. 12, pp. 2101–2107, Jun. 2014, doi: 10.1021/jz500546b/asset/images/large/jz-2014-00546b_0006.jpeg.

[176] X. H. Li, X. Wang, and M. Antonietti, “Mesoporous g-C3N4 nanorods as multifunctional supports of ultrafine metal nanoparticles: hydrogen generation from water and reduction of nitrophenol with tandem catalysis in one step,” *Chemical Science*, vol. 3, no. 6, pp. 2170–2174, May 2012, doi: 10.1039/c2sc20289a.

[177] L. el Firdoussi *et al.*, “Selective palladium-catalysed functionalization of limonene: synthetic and mechanistic aspects,” *Journal of Molecular Catalysis A: Chemical*, vol. 135, no. 1, pp. 11–22, Sep. 1998, doi: 10.1016/s1381-1169(97)00285-9.

[178] J. Filley, A. Miedaner, M. Ibrahim, M. R. Nimlos, and D. M. Blake, “Energetics of the 2+2 cyclization of limonene,” *Journal of Photochemistry and Photobiology A: Chemistry*, vol. 139, no. 1, pp. 17–21, Feb. 2001, doi: 10.1016/s1010-6030(00)00424-x.

[179] R. M. Scrowston, “Chemistry of the monoterpenes. An encyclopedic handbook, parts A + B : William F. Erman, M. Dekker, New York, 1985 (ISBN 0-8247-1573-X, Pt. A, ISBN 0-8247-7312-8, Pt. B), pp. 1709.,” *Analytica Chimica Acta*, vol. 189, pp. 393–394, Jan. 1986, doi: 10.1016/s0003-2670(00)83748-4.

[180] G. W. Huber, S. Iborra, and A. Corma, “Synthesis of transportation fuels from biomass: Chemistry, catalysts, and engineering,” *Chemical Reviews*, vol. 106, no. 9, pp. 4044–4098, Sep. 2006, doi: 10.1021/cr068360d/asset/images/large/cr068360df00033.jpeg.

[181] M. S. Kharasch and W. B. Reynolds, “Rearrangements in the terpene series. I. Isomerization and esterification of α-pinene,” *Journal of Organic Chemistry*, vol. 9, no. 2, pp. 148–154, Mar. 1944, doi: 10.1021/jo01184a003/asset/jo01184a003.fp.png_v03.

[182] B. A. Allal, L. el Firdoussi, S. Allaoud, A. Karim, Y. Castanet, and A. Mortreux, “Catalytic oxidation of α-pinene by transition metal using t-butyl hydroperoxide and hydrogen peroxide,” *Journal of Molecular Catalysis A: Chemical*, vol. 200, no. 1–2, pp. 177–184, Jun. 2003, doi: 10.1016/s1381-1169(03)00038-4.

[183] S. el Houssame, L. el Firdoussi, S. Allaoud, A. Karim, Y. Castanet, and A. Mortreux, “Palladium-catalyzed alkoxycarbonylation of allylic natural terpenic functionalized olefins,” *Journal of Molecular Catalysis A: Chemical*, vol. 168, no. 1–2, pp. 15–23, Mar. 2001, doi: 10.1016/s1381-1169(00)00381-2.

[184] A. C. Bueno, B. B. N. S. Brandão, and E. v. Gusevskaya, “Aromatization of para-menthenic terpenes by aerobic oxidative dehydrogenation catalyzed by p-benzoquinone,” *Applied Catalysis A: General*, vol. 351, no. 2, pp. 226–230, Dec. 2008, doi: 10.1016/j.apcata.2008.09.023.

[185] V. Kumar and A. K. Agarwal, “A REVIEW ON CATALYTIC TERPENE TRANSFORMATION OVER HETEROGENEOUS CATALYST,” *CHEMISTRY Int.J.Curr.Res.Chem.Pharma.Sci*, vol. 1, no. 2, pp. 78–88, 2014, Accessed: Aug. 05, 2022. [Online]. Available: www.ijcrcps.com

[186] G. Tegge, “Ullmann’s Encyclopedia of Industrial Chemistry. Fifth, Completely Revised Edition. Volume B 4: Principles of Chemical Reaction Engineering and Plant Design. VCH Verlagsgesellschaft mbH, D-6940 Weinheim (Fed. Rep. of Germany), 1992. ISBN 3-527-20134-3 (Weinheim …) Pp., ISBN 0-89573-539-3 (New York) Pp. Executive Editor: Wolfgang Gerhartz. Editors: Barbara Elvers, Stephen Hawkins, Gail Schulz. XV, 625 pages, with numerous Figures and Tables. Hardcover DM 550,–; Special set price for Volumes B1-B4,” *Starch - Stärke*, vol. 45, no. 5, pp. 201–201, Jan. 1993, doi: 10.1002/star.19930450522.

[187] P. W. D. Mitchell and D. E. Sasser, “Catalytic dehydrogenation of cyclic dienes,” 1993

[188] S. Barman, S. K. Maity, and N. C. Pradhan, “Alkylation of toluene with isopropyl alcohol catalyzed by Ce-exchanged NaX zeolite,” *Chemical Engineering Journal*, vol. 114, no. 1–3, pp. 39–45, Nov. 2005, doi: 10.1016/j.cej.2005.08.014.

[189] C. M. McBride, W. Chrisman, C. E. Harris, and B. Singaram, “Efficient synthesis of substituted benzenes from 1,3-dienes or 1,4-cyclohexadienes with KMnO4 under mild conditions,” *Tetrahedron Letters*, vol. 40, no. 1, pp. 45–48, Jan. 1999, doi: 10.1016/s0040-4039(98)80015-4.

[190] L. Reggel, S. Friedman, and I. Wender, “The Lithium-Ethylenediamine System. II. Isomerization of Olefins and Dehydrogenation of Cyclic Dienes,” *Journal of*

Organic Chemistry, vol. 23, no. 8, pp. 1136–1139, Aug. 1958, doi: 10.1021/jo01102a014/asset/jo01102a014.fp.png_v03.

[191] D. Buhl, P. A. Weyrich, W. M. H. Sachtler, and W. F. Hölderich, "Support effects in the Pd catalyzed dehydrogenation of terpene mixtures to p-cymene," *Applied Catalysis A: General*, vol. 171, no. 1, pp. 1–11, Jun. 1998, doi: 10.1016/s0926-860x(98)00039-8.

[192] H. Pines, R. C. Olberg, V. N. Ipatieff, and R. C. Olberg, "Studies in the Terpene Series. VIII. Effect of Catalyst, Solvent and Temperature on the Dehydrogenation of Pinane and p-Menthane," *J Am Chem Soc*, vol. 70, no. 2, pp. 533–537, Feb. 1948, doi: 10.1021/ja01182a031/asset/ja01182a031.fp.png_v03.

[193] J. Du, H. Xu, J. Shen, J. Huang, W. Shen, and D. Zhao, "Catalytic dehydrogenation and cracking of industrial dipentene over M/SBA-15 (M = Al, Zn) catalysts," *Applied Catalysis A: General*, vol. 296, no. 2, pp. 186–193, Dec. 2005, doi: 10.1016/j.apcata.2005.08.030.

[194] C. Catrinescu, C. Fernandes, P. Castilho, and C. Breen, "Influence of exchange cations on the catalytic conversion of limonene over Serra de Dentro (SD) and SAz-1 clays: Correlations between acidity and catalytic activity/selectivity," *Applied Catalysis A: General*, vol. 311, no. 1–2, pp. 172–184, Sep. 2006, doi: 10.1016/j.apcata.2006.06.023.

[195] C. Lopes, J. Lourenço, C. Pereira, and M. J. Marcelo-Curto, "Aromatization of Limonene with Zeolites Y," *Natural Products in the New Millennium: Prospects and Industrial Application*, pp. 429–436, 2002, doi: 10.1007/978-94-015-9876-7_43.

[196] V. Ipat'ev and G. J. Balachinskii, "No title," *Russian Physical Chemistry Society*, vol. 43, 1912.

[197] R. M. Albert and S. G. Traynor, *Naval stores-production, chemistry and utilization*. Pulp Chemical Association, 1989.

[198] J. Wright, G. J. Drtina, R. A. Roberts, and L. A. Paquette, "A convergent synthesis of triquinane sesterterpenes. Enantioselective synthesis of (-)-retigeranic acid A," *J Am Chem Soc*, vol. 110, no. 17, pp. 5806–5817, 1988, doi: 10.1021/ja00225a036/suppl_file/ja00225a036_si_001.pdf.

[199] N. I. Tracy, D. Chen, D. W. Crunkleton, and G. L. Price, “Hydrogenated monoterpenes as diesel fuel additives,” *Fuel*, vol. 88, no. 11, pp. 2238–2240, Nov. 2009, doi: 10.1016/j.fuel.2009.02.002.

[200] S. Agarwal and J. N. Ganguli, “Selective hydrogenation of monoterpenes on Rhodium (0) nanoparticles stabilized in Montmorillonite K-10 clay,” *Journal of Molecular Catalysis A: Chemical*, vol. 372, pp. 44–50, Jun. 2013, doi: 10.1016/j.molcata.2013.01.036.

[201] R. J. Grau, P. D. Zgolicz, C. Gutierrez, and H. A. Taher, “Liquid phase hydrogenation, isomerization and dehydrogenation of limonene and derivatives with supported palladium catalysts,” *Journal of Molecular Catalysis A: Chemical*, vol. 148, no. 1–2, pp. 203–214, Dec. 1999, doi: 10.1016/s1381-1169(99)00108-9.

[202] T. Osako, K. Torii, A. Tazawa, and Y. Uozumi, “Continuous-flow hydrogenation of olefins and nitrobenzenes catalyzed by platinum nanoparticles dispersed in an amphiphilic polymer,” *RSC Advances*, vol. 5, no. 57, pp. 45760–45766, May 2015, doi: 10.1039/c5ra07563g.

[203] S. Shimazu, N. Baba, N. Ichikuni, and T. Uematsu, “Regioselective hydrogenation of dienes catalyzed by palladium–aminosilane complexes grafted on MCM-41,” *Journal of Molecular Catalysis A: Chemical*, vol. 182–183, pp. 343–350, May 2002, doi: 10.1016/s1381-1169(01)00508-8.

[204] H. A. Smith and J. F. Fuzek, “The Influence of Certain Additives on the Rate of Catalytic Hydrogenation of Terpenes on Nickel,” *J Am Chem Soc*, vol. 72, no. 8, pp. 3454–3458, Aug. 1950, doi: 10.1021/ja01164a035/asset/ja01164a035.fp.png_v03.

[205] G. Rubulotta *et al.*, “Highly Selective Hydrogenation of R-(+)-Limonene to (+)-p-1-Menthene in Batch and Continuous Flow Reactors,” *ACS Sustainable Chemistry and Engineering*, vol. 5, no. 5, pp. 3762–3767, May 2017, doi: 10.1021/acssuschemeng.6b02381/asset/images/large/sc-2016-02381s_0003.jpeg.

[206] E. Bogel-Łukasik *et al.*, “Phase equilibrium-driven selective hydrogenation of limonene in high-pressure carbon dioxide,” *Green Chemistry*, vol. 9, no. 5, pp. 427–430, May 2007, doi: 10.1039/b617187g.

[207] H. Göksu, H. Can, K. Şendil, M. S. Gültekin, and Ö. Metin, "CoPd alloy nanoparticles catalyzed tandem ammonia borane dehydrogenation and reduction of aromatic nitro, nitrile and carbonyl compounds," *Applied Catalysis A: General*, vol. 488, pp. 176–182, Nov. 2014, doi: 10.1016/j.apcata.2014.09.043.

[208] Ö. Metin, H. Can, K. Şendil, and M. S. Gültekin, "Monodisperse Ag/Pd core/shell nanoparticles assembled on reduced graphene oxide as highly efficient catalysts for the transfer hydrogenation of nitroarenes," *Journal of Colloid and Interface Science*, vol. 498, pp. 378–386, Jul. 2017, doi: 10.1016/j.jcis.2017.03.066.

[209] P. T. Anastas and R. H. Crabtree, Eds., *Green Chemistry*. Weinheim: Wiley-VCH, 2009.

[210] M. Lajunen and A. M. P. Koskinen, "Co(II)-catalysed allylic oxidation of α-pinene by molecular oxygen; synthesis of verbenone," *Tetrahedron Letters*, vol. 35, no. 25, pp. 4461–4464, Jun. 1994, doi: 10.1016/s0040-4039(00)73384-3.

[211] M. K. Lajunen, T. Maunula, and A. M. P. Koskinen, "Co(II) Catalysed Oxidation of α-Pinene by Molecular Oxygen. Part 2," *Tetrahedron*, vol. 56, no. 41, pp. 8167–8171, Oct. 2000, doi: 10.1016/s0040-4020(00)00742-0.

[212] M. K. Lajunen, M. Myllykoski, and J. Asikkala, "Co(II)-catalysed oxidation of α-pinene by molecular oxygen: Part IV," *Journal of Molecular Catalysis A: Chemical*, vol. 198, no. 1–2, pp. 223–229, May 2003, doi: 10.1016/s1381-1169(02)00696-9.

[213] L. Menini, M. C. Pereira, L. A. Parreira, J. D. Fabris, and E. v. Gusevskaya, "Cobalt- and manganese-substituted ferrites as efficient single-site heterogeneous catalysts for aerobic oxidation of monoterpenic alkenes under solvent-free conditions," *Journal of Catalysis*, vol. 254, no. 2, pp. 355–364, Mar. 2008, doi: 10.1016/j.jcat.2008.01.013.

[214] N. v. Maksimchuk, M. S. Melgunov, Y. A. Chesalov, J. Mrowiec-Białoń, A. B. Jarzebski, and O. A. Kholdeeva, "Aerobic oxidations of α-pinene over cobalt-substituted polyoxometalate supported on amino-modified mesoporous silicates," *Journal of Catalysis*, vol. 246, no. 2, pp. 241–248, Mar. 2007, doi: 10.1016/j.jcat.2006.11.026.

[215] P. A. Robles-Dutenhefner, K. A. da Silva Rocha, E. M. B. Sousa, and E. v. Gusevskaya, “Cobalt-catalyzed oxidation of terpenes: Co-MCM-41 as an efficient shape-selective heterogeneous catalyst for aerobic oxidation of isolongifolene under solvent-free conditions,” *Journal of Catalysis*, vol. 265, no. 1, pp. 72–79, Jul. 2009, doi: 10.1016/j.jcat.2009.04.012.

[216] J. Xu, H. T. Wu, X. Wang, B. Xue, Y. X. Li, and Y. Cao, “A new and environmentally benign precursor for the synthesis of mesoporous g-C3N4 with tunable surface area,” *Physical Chemistry Chemical Physics*, vol. 15, no. 13, pp. 4510–4517, Mar. 2013, doi: 10.1039/c3cp44402c.

[217] X. Wang *et al.*, “A metal-free polymeric photocatalyst for hydrogen production from water under visible light,” *Nature Materials 2009 8:1*, vol. 8, no. 1, pp. 76–80, Nov. 2008, doi: 10.1038/nmat2317.

[218] S. Ergen, B. Nişanci, and Ö. Metin, “One-pot reductive amination of aldehydes with nitroarenes using formic acid as the hydrogen donor and mesoporous graphitic carbon nitride supported AgPd alloy nanoparticles as the heterogeneous catalyst,” *New Journal of Chemistry*, vol. 42, no. 12, pp. 10000–10006, Jun. 2018, doi: 10.1039/c8nj01569d.

[219] A. Thomas *et al.*, “Graphitic carbon nitride materials: variation of structure and morphology and their use as metal-free catalysts,” *Journal of Materials Chemistry*, vol. 18, no. 41, pp. 4893–4908, Oct. 2008, doi: 10.1039/b800274f.

[220] A. L. Wang, X. J. He, X. F. Lu, H. Xu, Y. X. Tong, and G. R. Li, “Palladium–Cobalt Nanotube Arrays Supported on Carbon Fiber Cloth as High-Performance Flexible Electrocatalysts for Ethanol Oxidation,” *Angewandte Chemie International Edition*, vol. 54, no. 12, pp. 3669–3673, Mar. 2015, doi: 10.1002/anie.201410792.

[221] Y. Wang *et al.*, “Carboxyl Multiwalled Carbon-Nanotube-Stabilized Palladium Nanocatalysts toward Improved Methanol Oxidation Reaction,” *ChemElectroChem*, vol. 2, no. 4, pp. 559–570, Apr. 2015, doi: 10.1002/celc.201402378.

[222] M. Brun, A. Berthet, and J. C. Bertolini, “XPS, AES and Auger parameter of Pd and PdO,” *Journal of Electron Spectroscopy and Related Phenomena*, vol. 104, no. 1–3, pp. 55–60, Jul. 1999, doi: 10.1016/s0368-2048(98)00312-0.

[223] K. A. Cychosz and M. Thommes, “Progress in the Physisorption Characterization of Nanoporous Gas Storage Materials,” *Engineering*, vol. 4, no. 4, pp. 559–566, Aug. 2018, doi: 10.1016/j.eng.2018.06.001.

[224] S. Cao *et al.*, “Single-Atom Engineering of Directional Charge Transfer Channels and Active Sites for Photocatalytic Hydrogen Evolution,” *Advanced Functional Materials*, vol. 28, no. 32, p. 1802169, Aug. 2018, doi: 10.1002/adfm.201802169.

[225] M. Retajczyk and A. Wróblewska, “Isomerization and Dehydroaromatization of R(+)-Limonene Over the Ti-MCM-41 Catalyst: Effect of Temperature, Reaction Time and Catalyst Content on Product Yield,” *Catalysts 2019, Vol. 9, Page 508*, vol. 9, no. 6, p. 508, Jun. 2019, doi: 10.3390/catal9060508.

[226] M. Guo, J. Peng, Q. Yang, and C. Li, “Highly Active and Selective RuPd Bimetallic NPs for the Cleavage of the Diphenyl Ether C-O Bond,” *ACS Catalysis*, vol. 8, no. 12, pp. 11174–11183, Dec. 2018, doi: 10.1021/acscatal.8b03253/asset/images/medium/cs-2018-03253u_m005.gif.

APPENDIX A: NMR Spectra

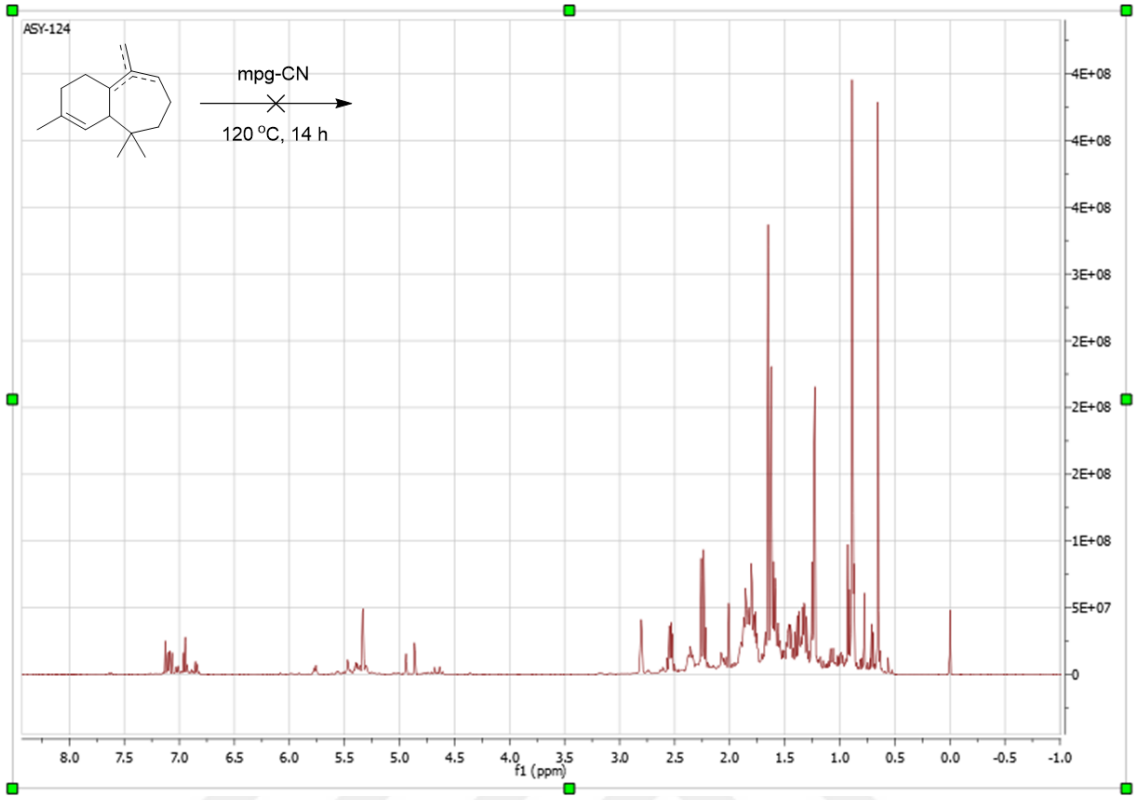

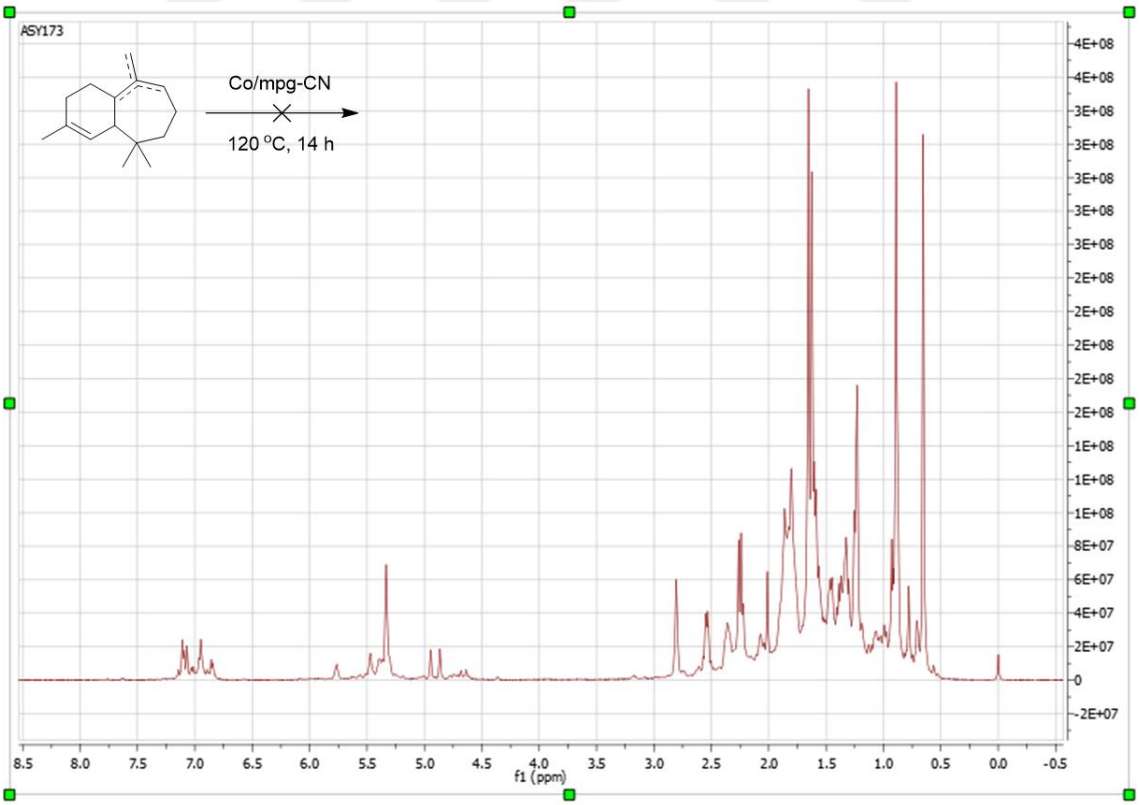

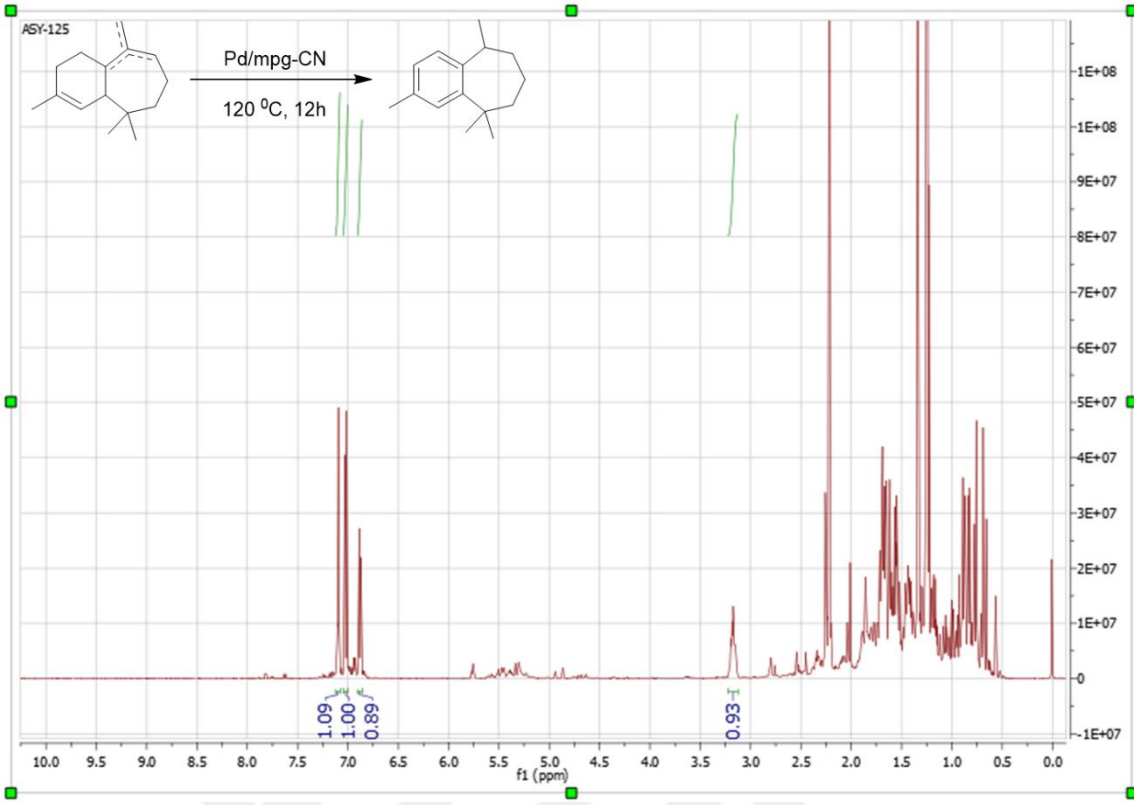
ASY-125
Pd/mpg-CN
120 °C, 12h
1.09
1.00
0.89
0.93
f1 (ppm)

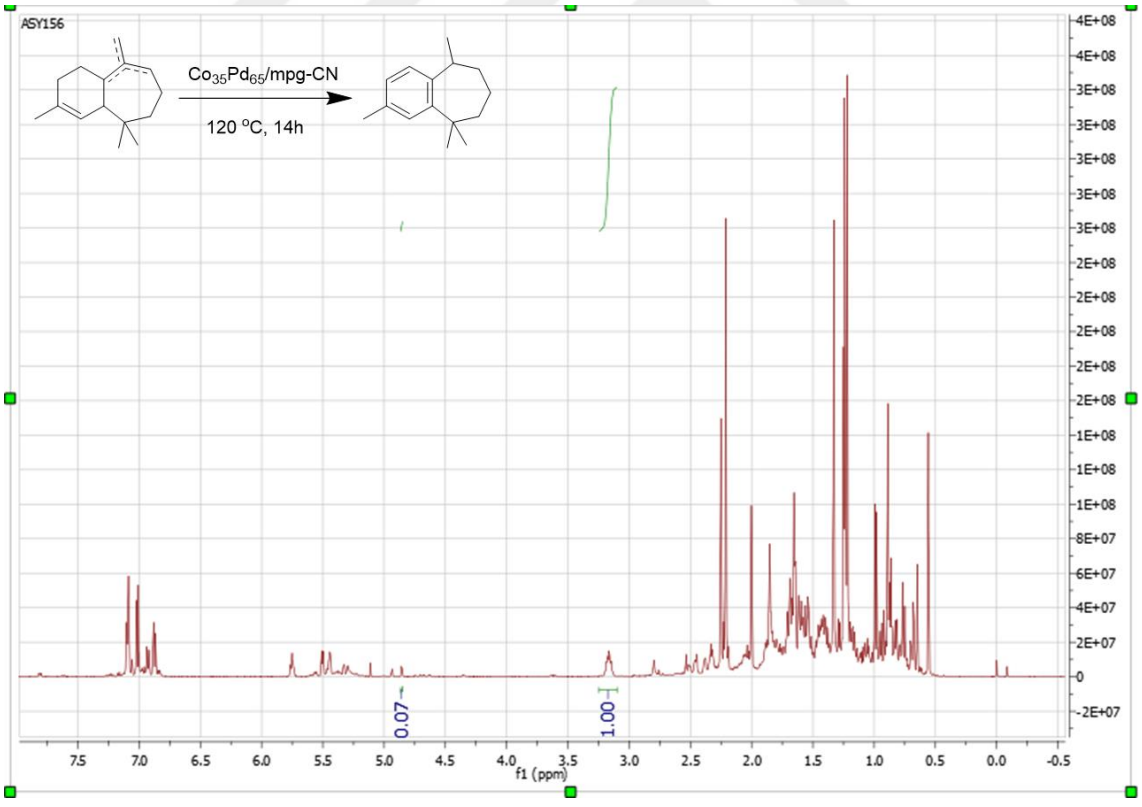
ASY156
Co35Pd65/mpg-CN
120 °C, 14h
0.07
1.00
f1 (ppm)

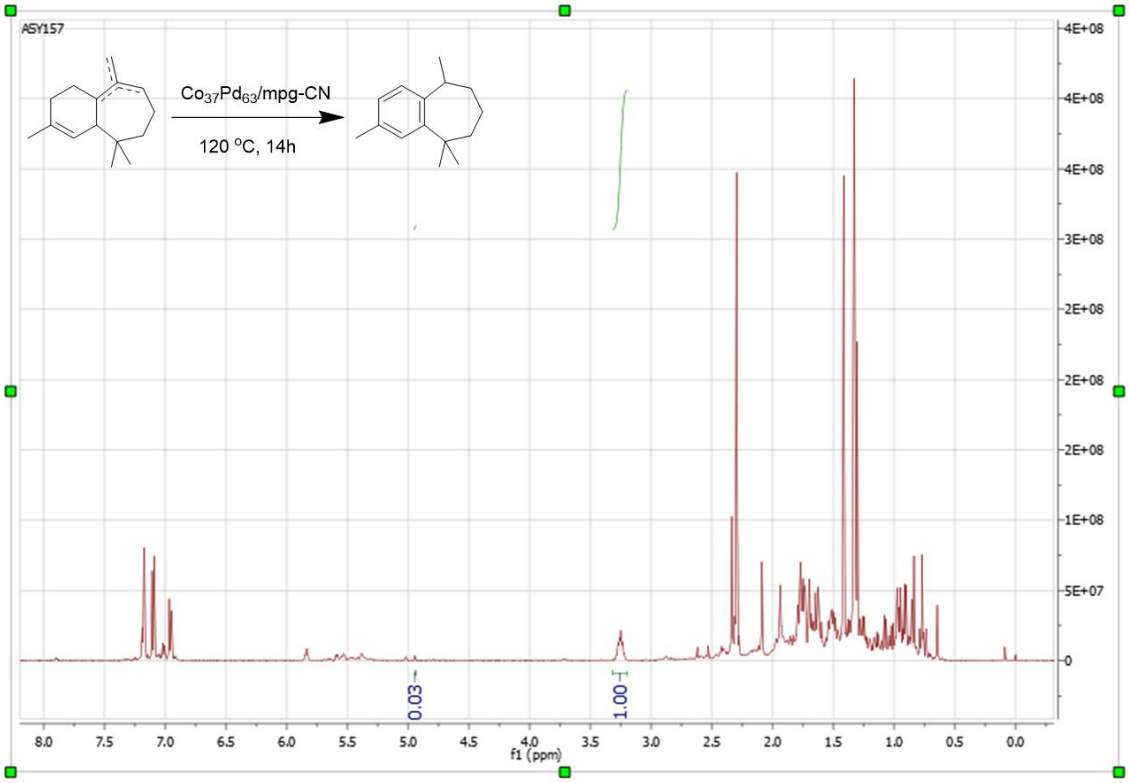
ASY157
Co37Pd63/mpg-CN
120 °C, 14h
0.03
1.00
f1 (ppm)

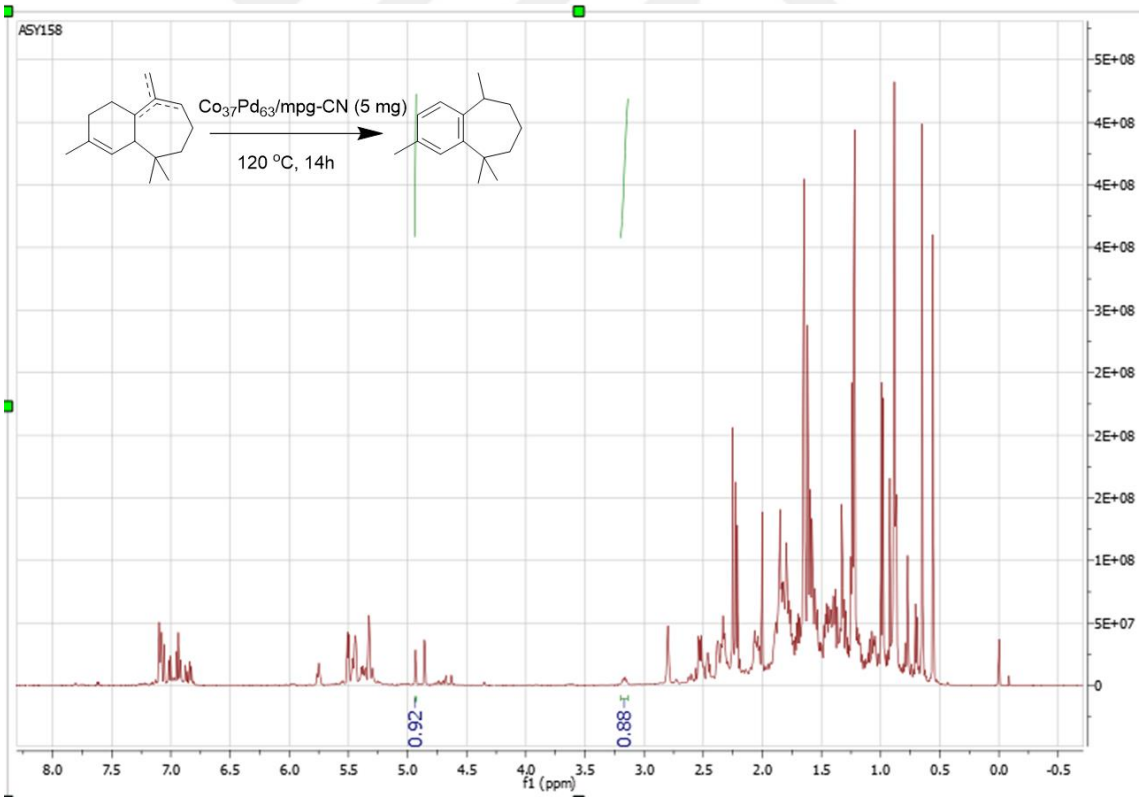
ASY158
Co37Pd63/mpg-CN (5 mg)
120 °C, 14h
0.92
0.88
f1 (ppm)

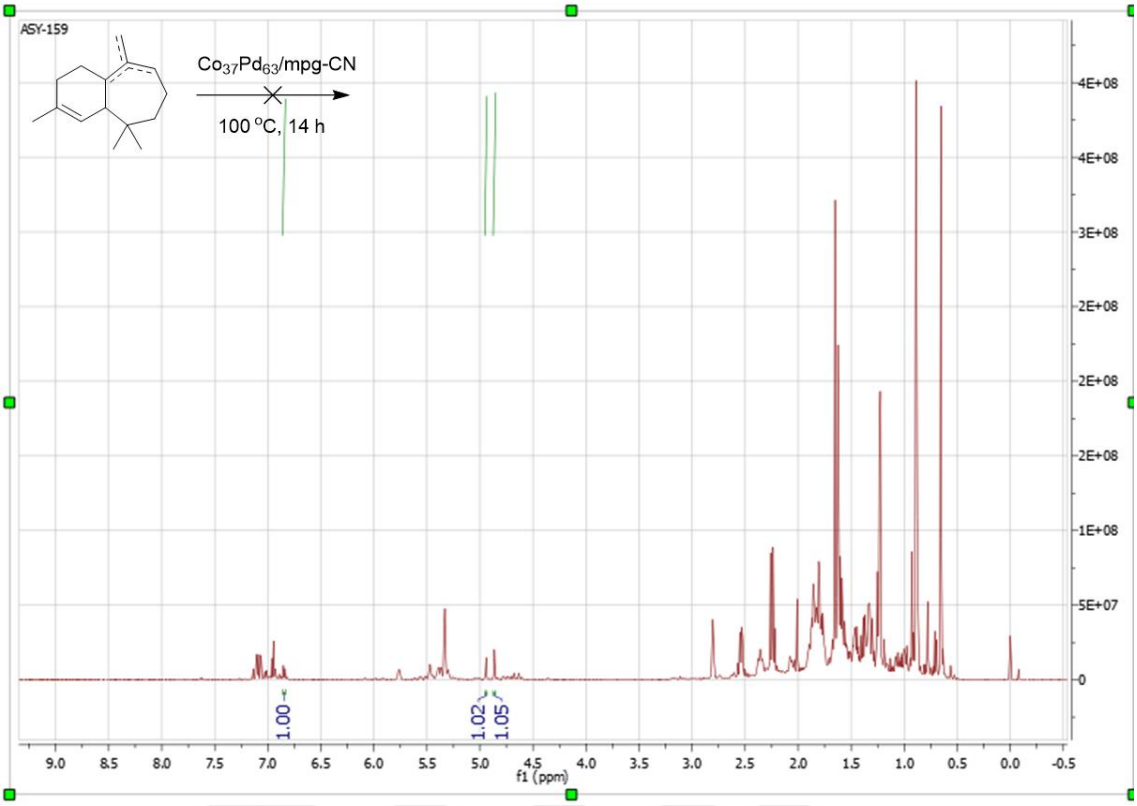
ASY-159
Co37Pd63/mpg-CN
100 °C, 14 h
1.00
1.02
1.05
f1 (ppm)

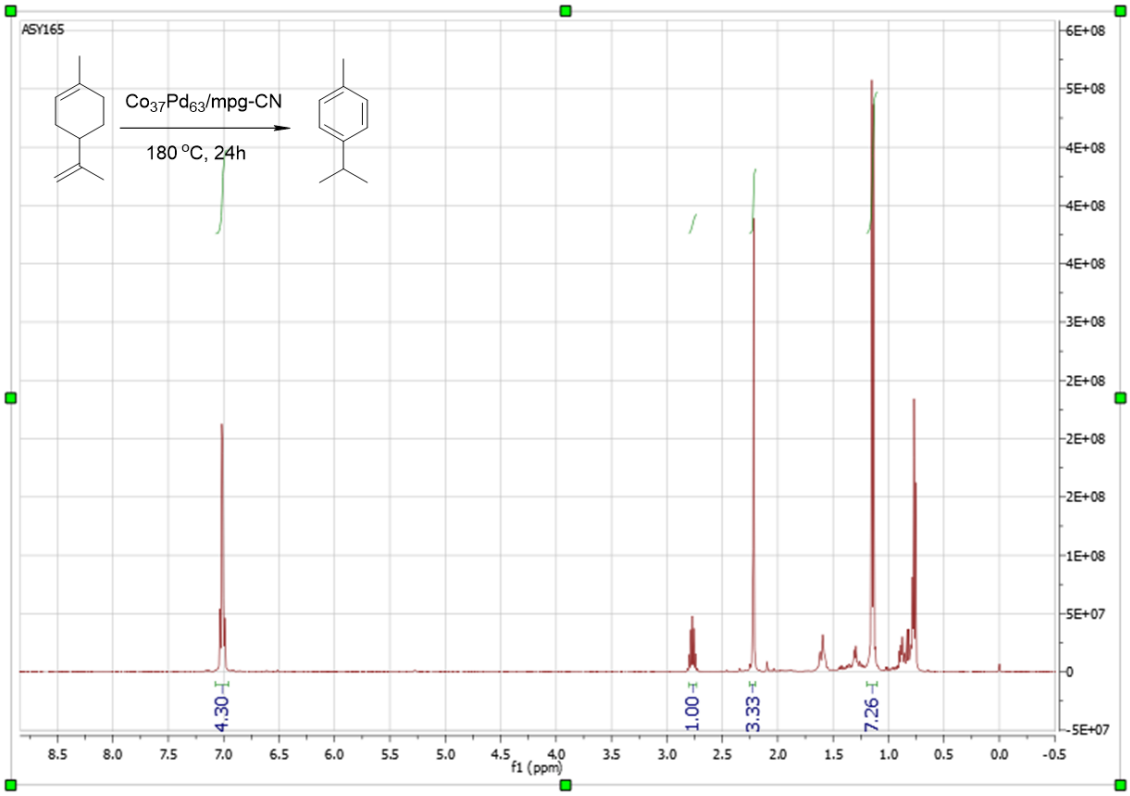
ASY165
Co37Pd63/mpg-CN
180 °C, 24h
4.30
1.00
3.33
7.26
f1 (ppm)

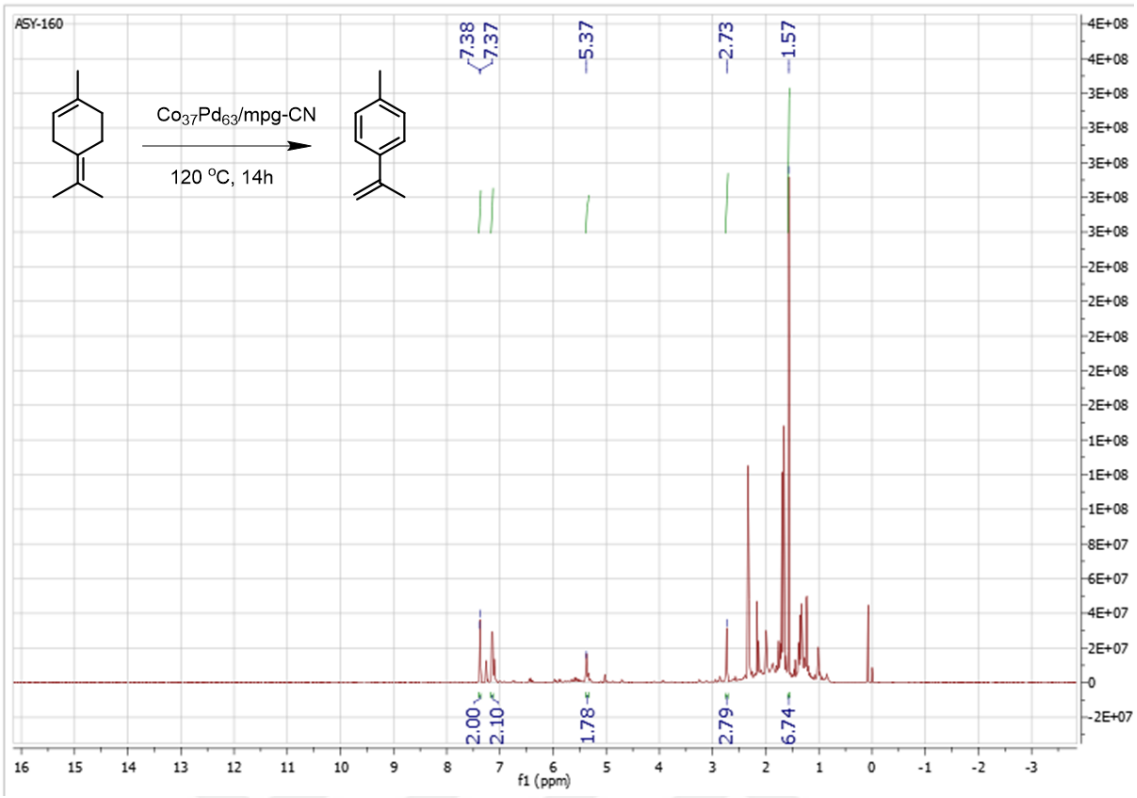
ASY-160
Co37Pd63/mpg-CN
120 °C, 14h
7.38
7.37
5.37
2.73
1.57
2.00
2.10
1.78
2.79
6.74
f1 (ppm)

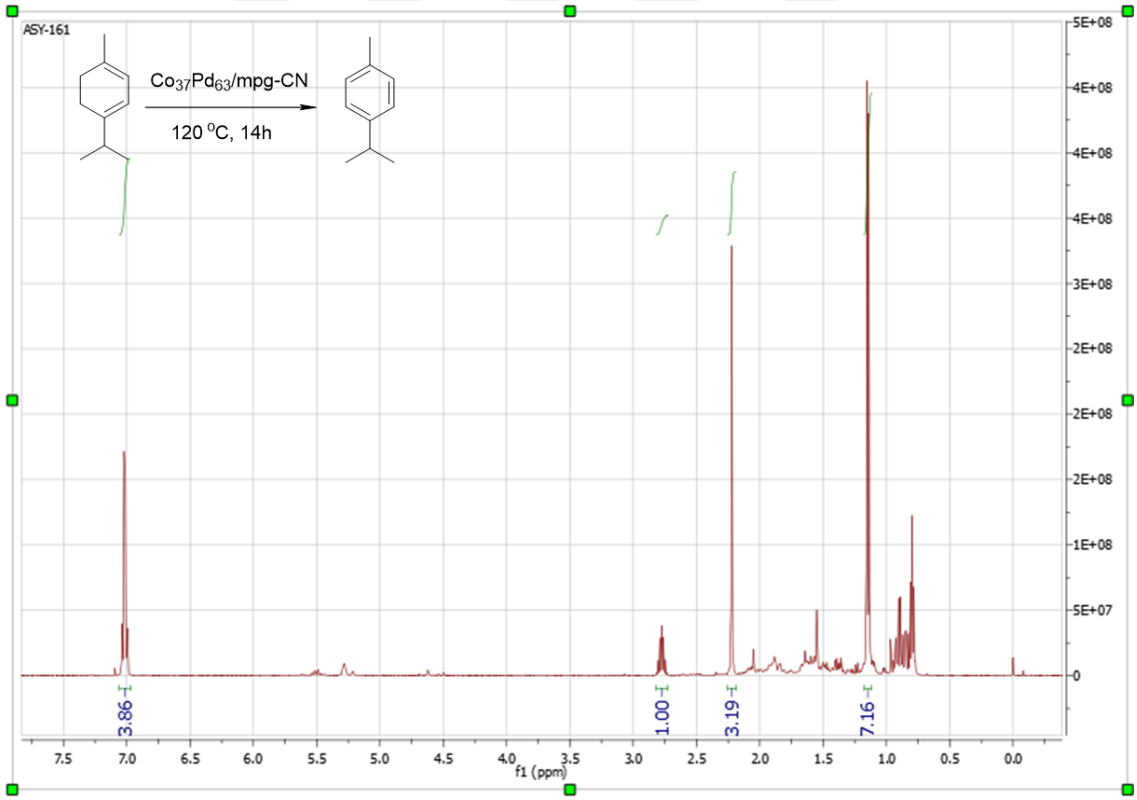
ASY-161
Co37Pd63/mpg-CN
120 °C, 14h
3.86
1.00
3.19
7.16
f1 (ppm)

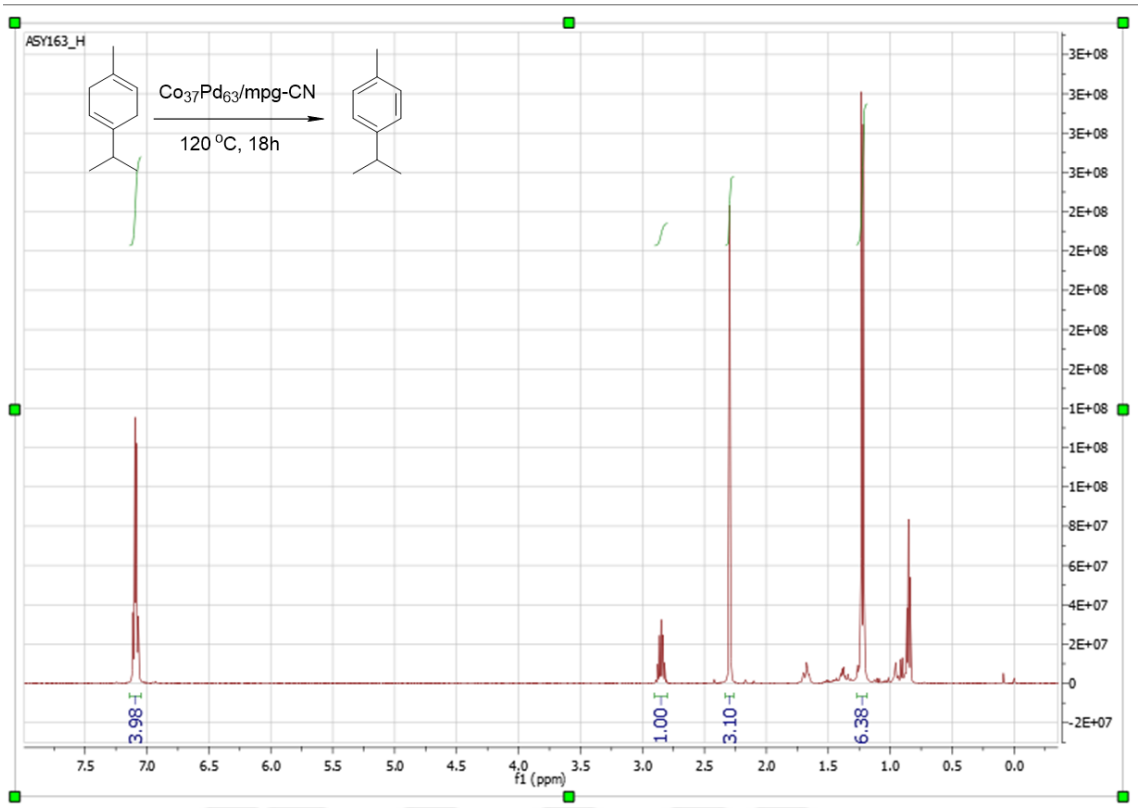
ASY163_H
Co37Pd63/mpg-CN
120 °C, 18h
3.98
1.00
3.10
6.38
f1 (ppm)

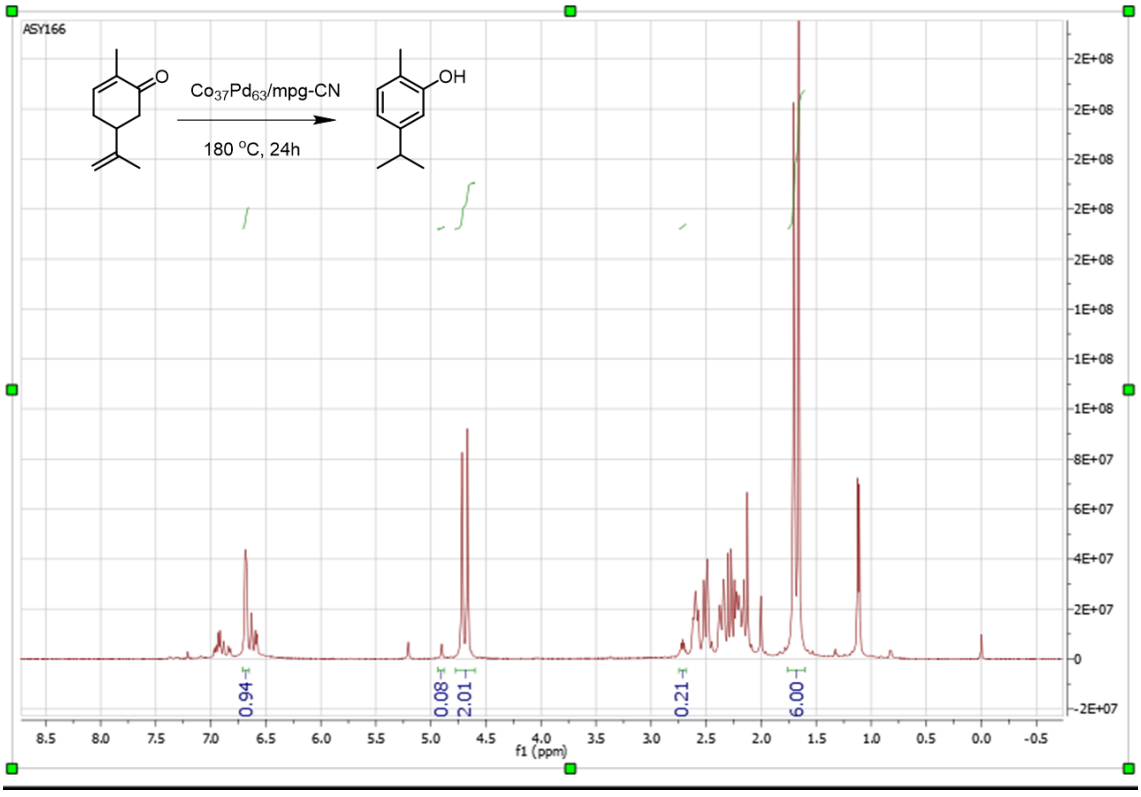
ASY166
Co37Pd63/mpg-CN
180 °C, 24h
OH
0.94
0.08
2.01
0.21
6.00
f1 (ppm)

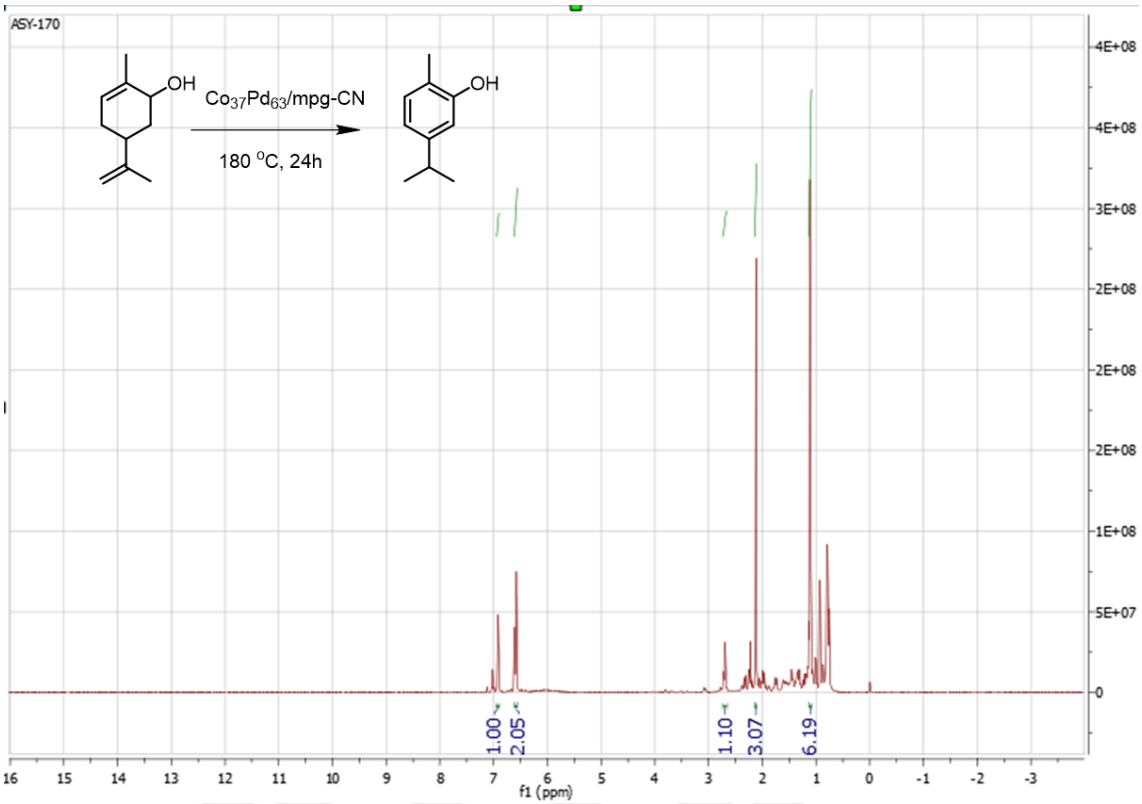
ASY-170
OH
Co37Pd63/mpg-CN
180 °C, 24h
OH
1.00
2.05
1.10
3.07
6.19
f1 (ppm)

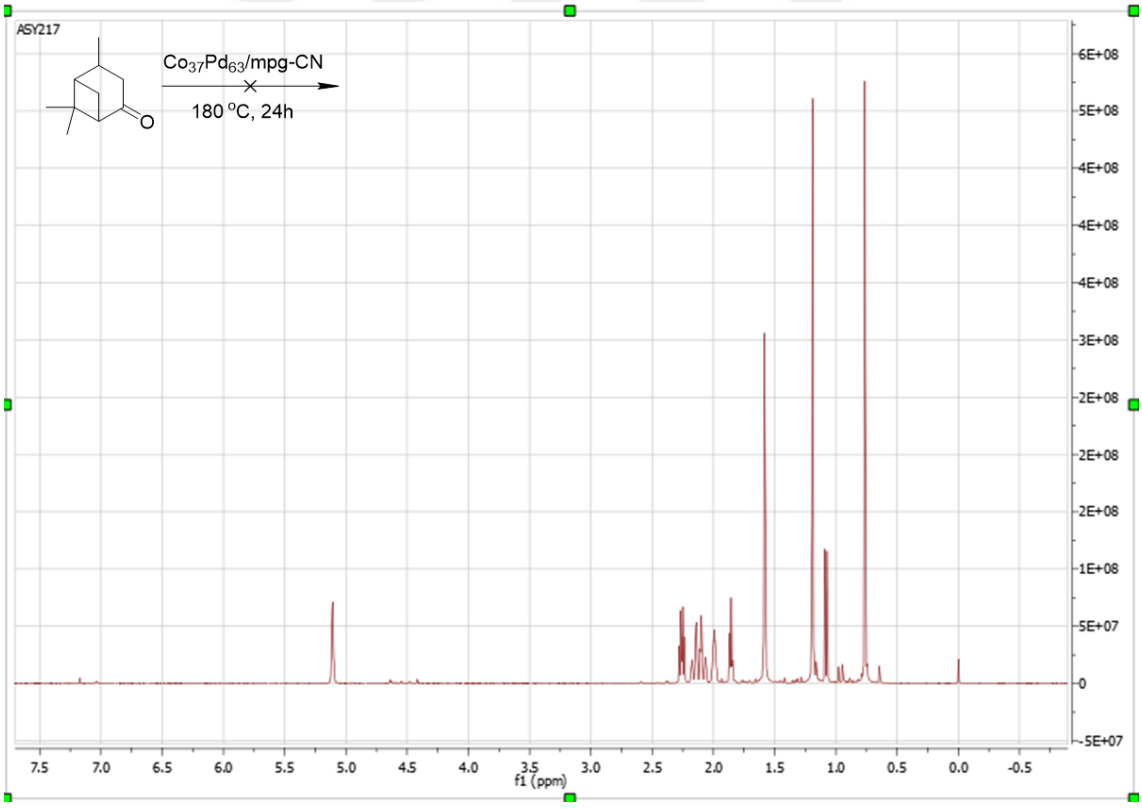
ASY217
Co37Pd63/mpg-CN
180 °C, 24h
O
f1 (ppm)

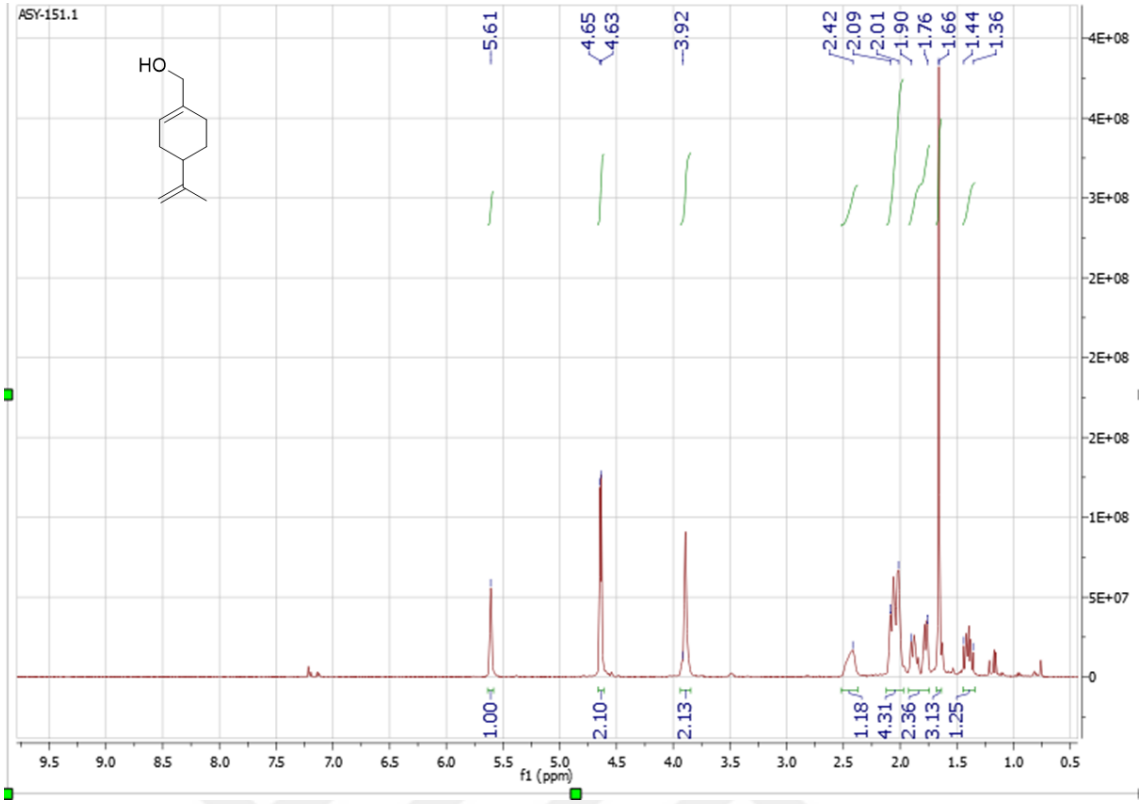
ASY-151.1
HO
5.61
4.65
4.63
3.92
2.42
2.09
2.01
1.90
1.76
1.66
1.44
1.36
1.00
2.10
2.13
1.18
4.31
2.36
3.13
1.25
f1 (ppm)

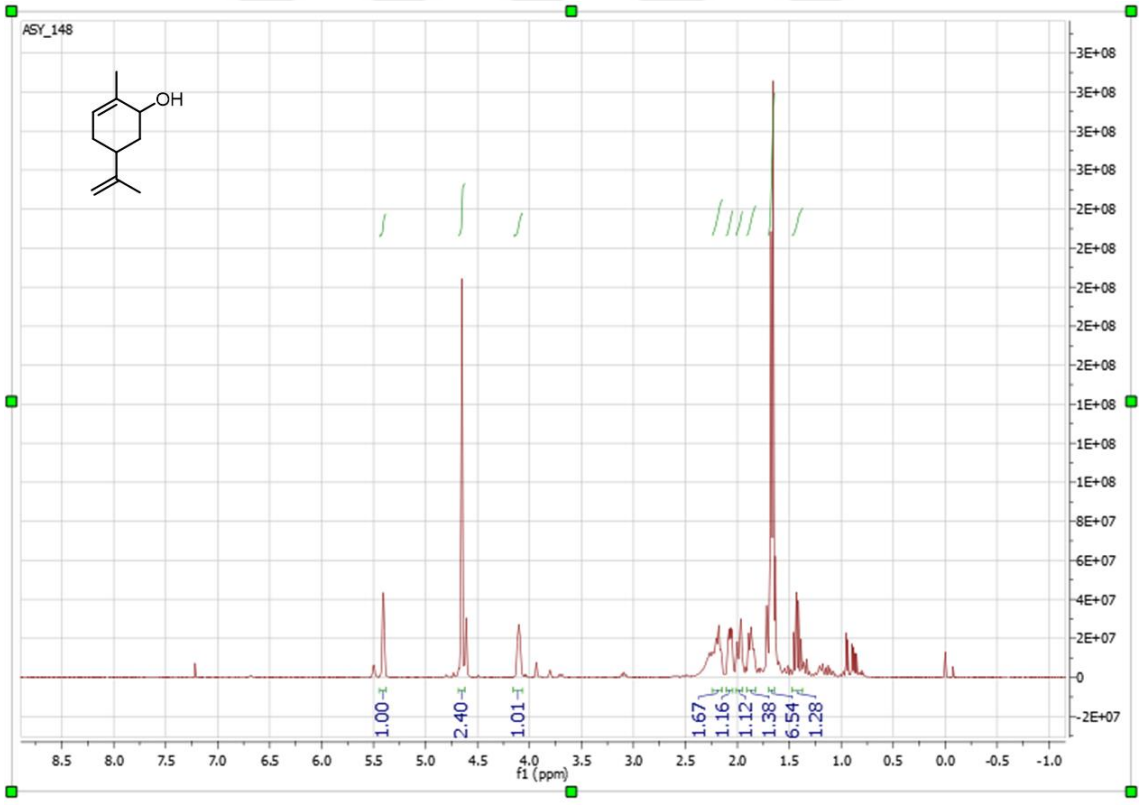
ASY_148
OH
1.00
2.40
1.01
1.67
1.16
1.12
1.38
6.54
1.28
f1 (ppm)

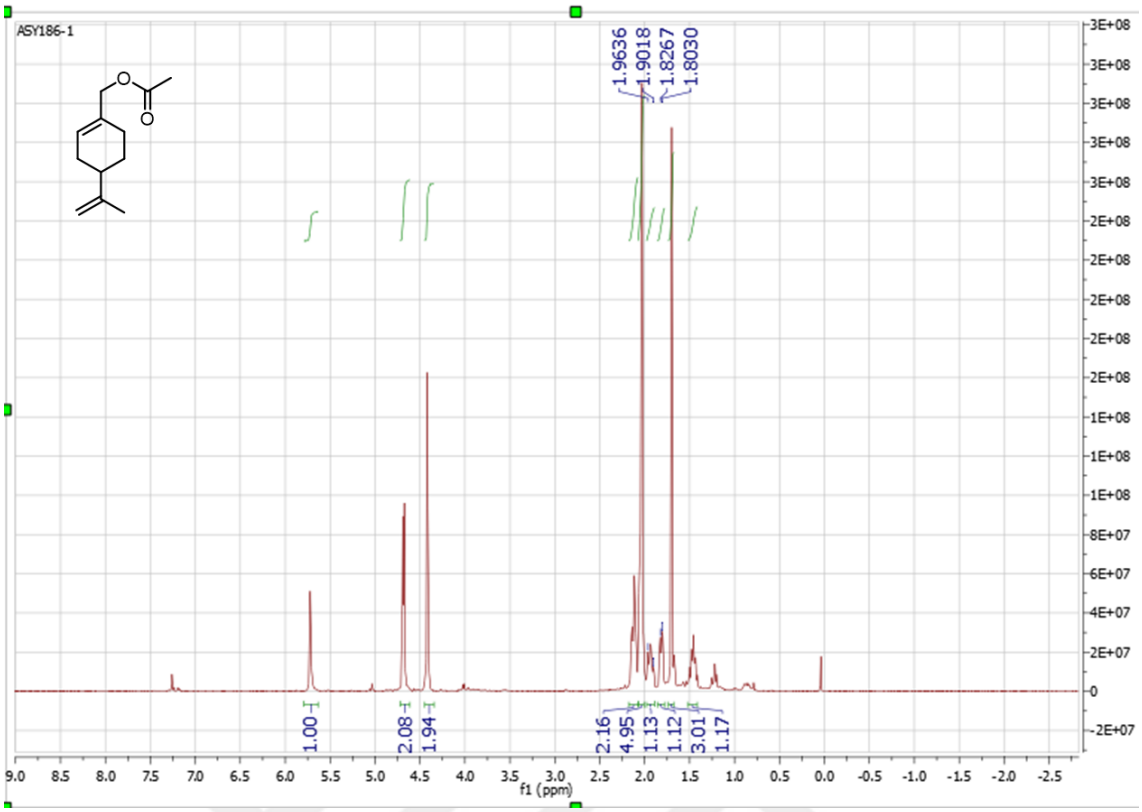
ASY186-1
1.9636
1.9018
1.8267
1.8030
1.00
2.08
1.94
2.16
4.95
1.13
1.12
3.01
1.17
f1 (ppm)

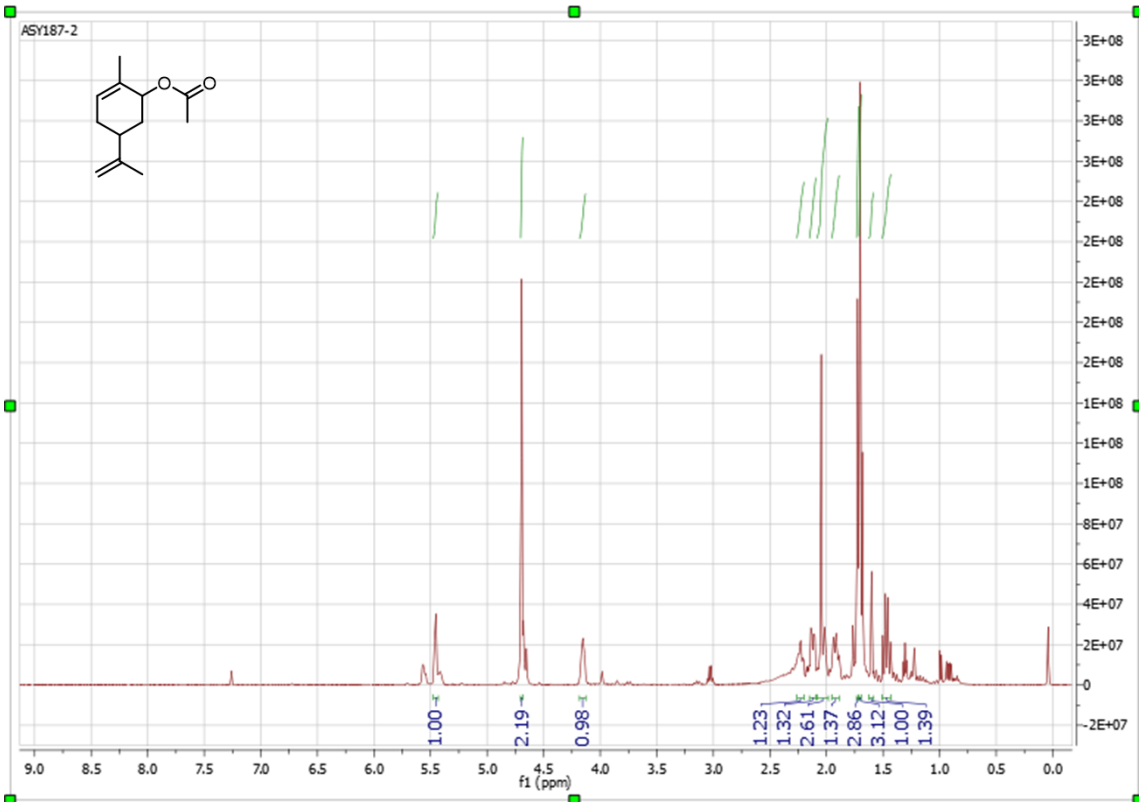
ASY187-2
1.00
2.19
0.98
1.23
1.32
2.61
1.37
2.86
3.12
1.00
1.39
f1 (ppm)

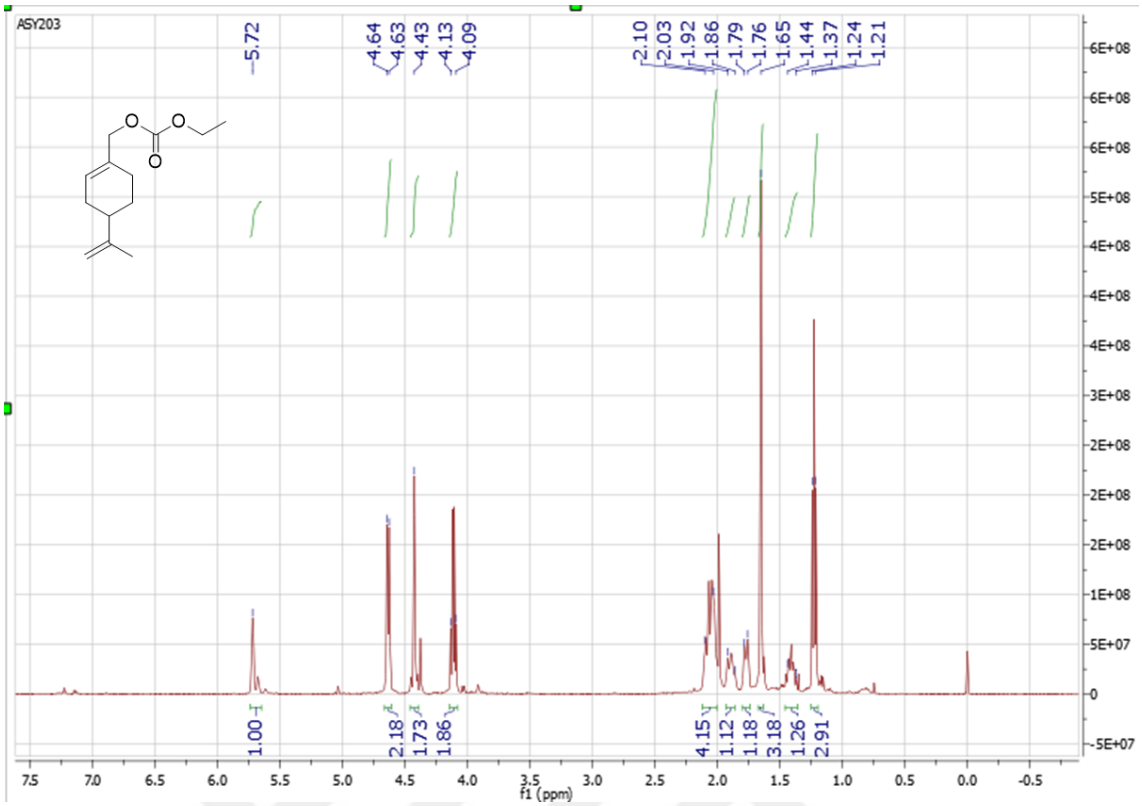
ASY203
5.72
4.64
4.63
4.43
4.13
4.09
2.10
2.03
1.92
1.86
1.79
1.76
1.65
1.44
1.37
1.24
1.21
1.00
2.18
1.73
1.86
4.15
1.12
1.18
3.18
1.26
2.91
f1 (ppm)

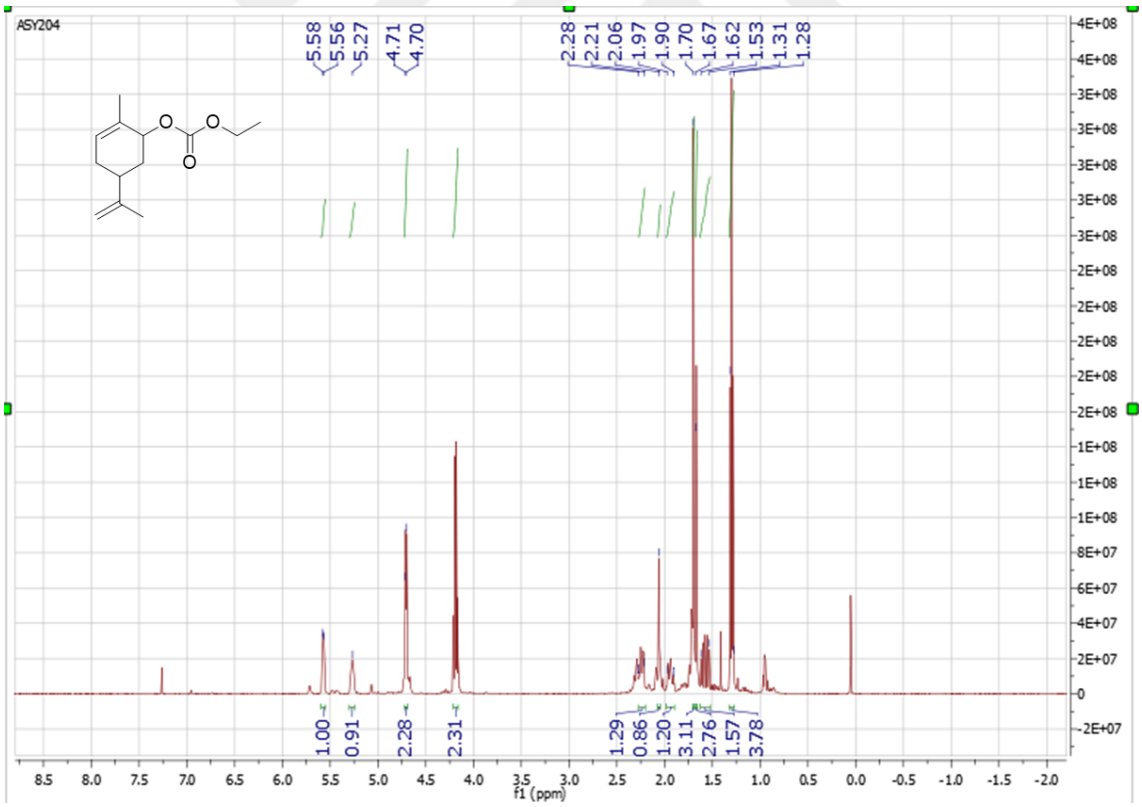
ASY204
5.58
5.56
5.27
4.71
4.70
2.28
2.21
2.06
1.97
1.90
1.70
1.67
1.62
1.53
1.31
1.28
1.00
0.91
2.28
2.31
1.29
0.86
1.20
3.11
2.76
1.57
3.78
f1 (ppm)

APPENDIX B: GC-MS Spectra

Chromatogram ASY_184 C:\GCMSsolution\Data\2021\PerillylAlcohol\ASY_184_Qualitative.qgd

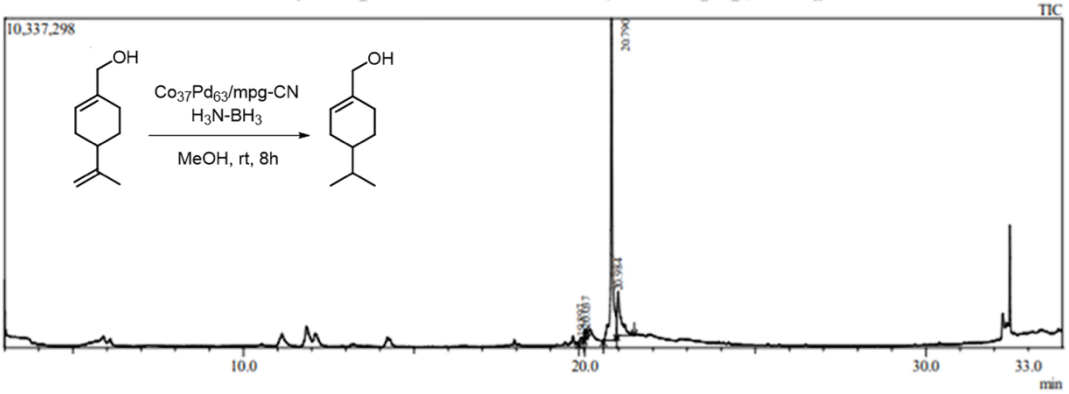

Peak Report TIC

Peak#	R.Time	I.Time	F.Time	Area	Area%	Height	Height%	A/H	Name
1	19.897	19.827	19.977	1011026	1.94	171465	1.43	5.90	trans-p-Menthan-7-ol
2	20.037	19.983	20.087	1201373	2.30	318323	2.66	3.77	p-Menth-1(7)-en-9-ol
3	20.790	20.547	20.937	39441456	75.49	10104806	84.45	3.90	p-Menth-2-en-7-ol, trans-
4	20.984	20.937	21.453	10591351	20.27	1370513	11.45	7.73	Perilla alcohol
				52245206	100.00	11965107	100.00		

Chromatogram ASY_185 C:\GCMSsolution\Data\2021\PerillylAlcohol\ASY_185_Qualitative.qgd

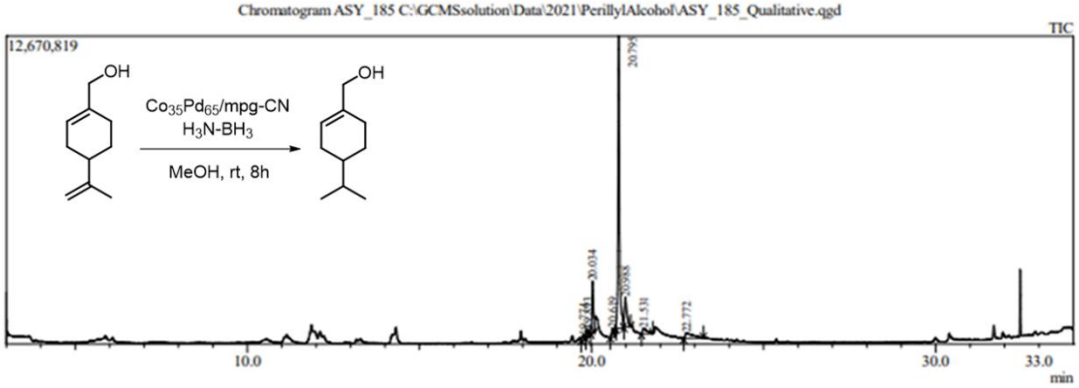

Peak Report TIC

Peak#	R.Time	I.Time	F.Time	Area	Area%	Height	Height%	A/H	Name
1	19.774	19.707	19.827	995803	1.63	201590	1.21	4.94	p-Menth-2-en-7-ol, cis-
2	19.893	19.837	19.957	1322273	2.17	321090	1.92	4.12	Cyclohexanemethanol, 4-(1-methylethyl)-, tra
3	20.034	19.987	20.097	7059468	11.58	2143041	12.81	3.29	Camphene (CAS)
4	20.619	20.547	20.690	1928299	3.16	360647	2.16	5.35	trans-Shisool
5	20.795	20.710	20.930	38376369	62.95	12017378	71.84	3.19	p-Menth-2-en-7-ol, trans-
6	20.988	20.950	21.140	5610096	9.20	1233953	7.38	4.55	Perilla alcohol
7	21.531	21.457	21.783	2139353	3.51	243578	1.46	8.78	p-Menth-2-en-7-ol, trans-
8	22.772	22.680	23.253	3533191	5.80	206450	1.23	17.11	2,3-Diazabicyclo[2.2.1]hept-2-ene, 5-ethenyl-
				60964852	100.00	16727727	100.00		

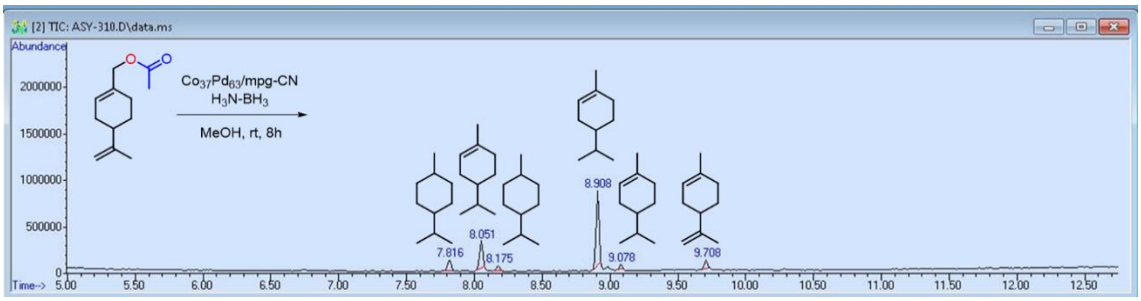

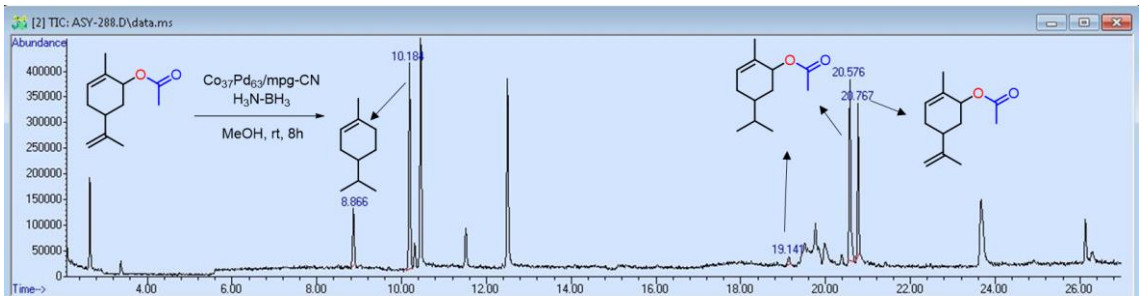
[2] TIC: ASY-288.D\data.ms
Abundance
Co37Pd63/mpg-CN
H3N-BH3
MeOH, rt, 8h
10.184
8.866
20.576
20.767
19.141
Time-->

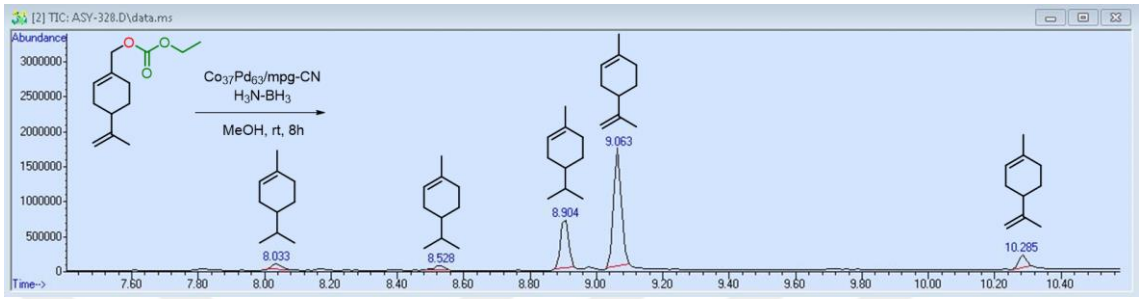
[2] TIC: ASY-328.D\data.ms
Abundance
Co37Pd63/mpg-CN
H3N-BH3
MeOH, rt, 8h
8.033
8.528
8.904
9.063
10.285
Time-->

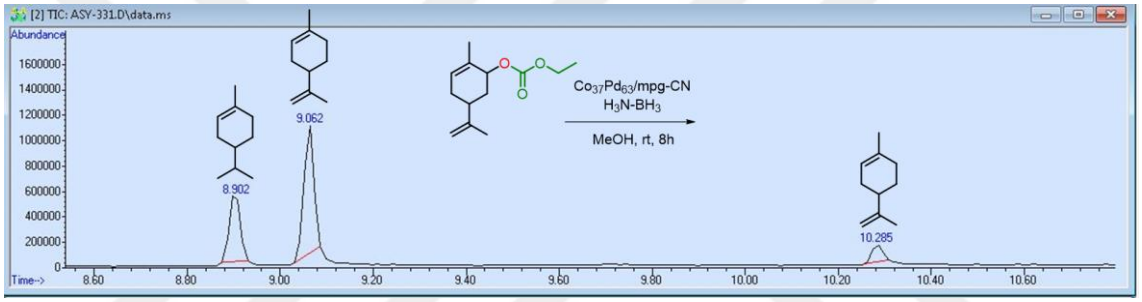
[2] TIC: ASY-331.D\data.ms
Abundance
Co37Pd63/mpg-CN
H3N-BH3
MeOH, rt, 8h
8.902
9.062
10.285
Time-->

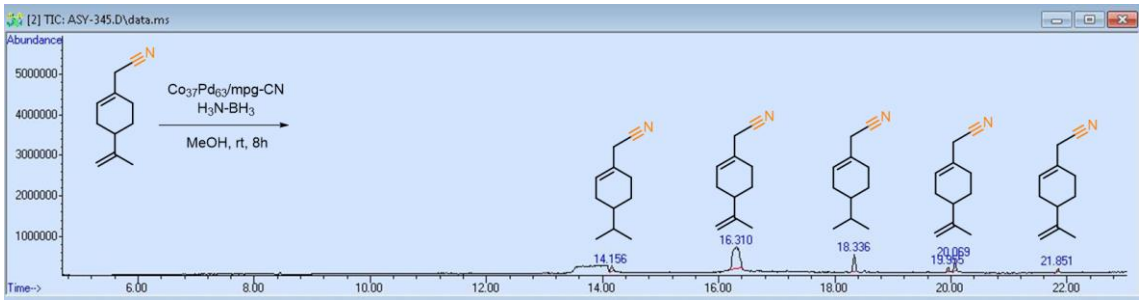
[2] TIC: ASY-345.D\data.ms
Abundance
Co37Pd63/mpg-CN
H3N-BH3
MeOH, rt, 8h
14.156
16.310
18.336
19.969
21.851
Time-->

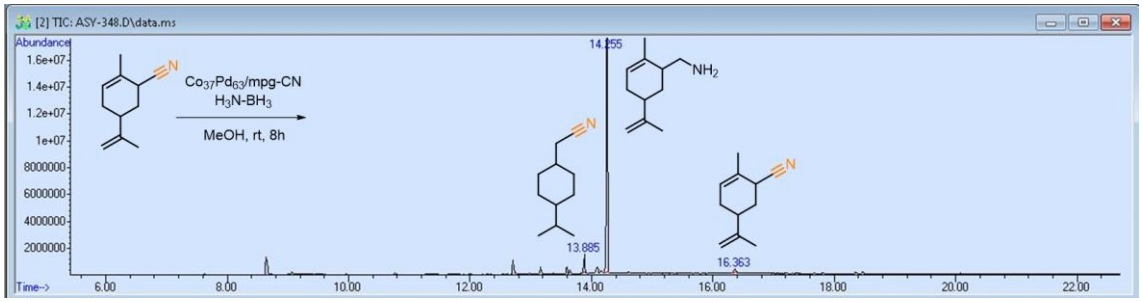
[2] TIC: ASY-348.D\data.ms
Abundance
Co37Pd63/mpg-CN
H3N-BH3
MeOH, rt, 8h
14.155
NH2
13.885
16.363
Time-->

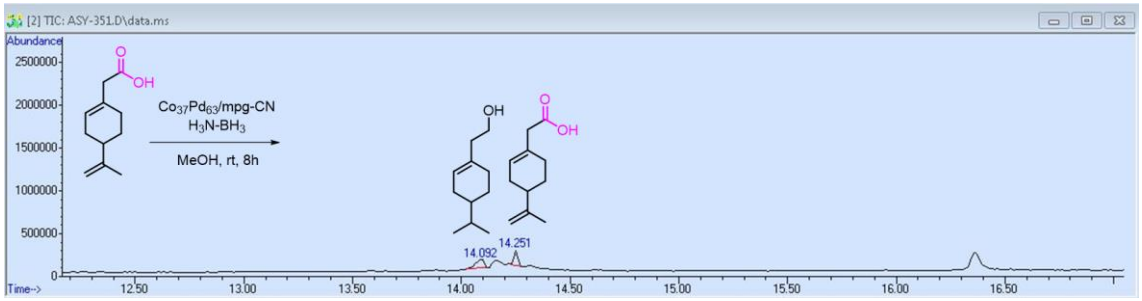
[2] TIC: ASY-351.D\data.ms
Abundance
Co37Pd63/mpg-CN
H3N-BH3
MeOH, rt, 8h
14.092
14.251
Time-->

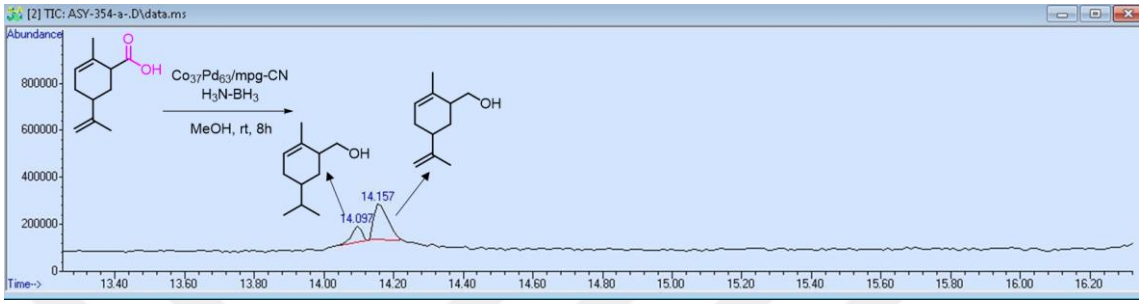
[2] TIC: ASY-354-a-.D\data.ms
Abundance
Co37Pd63/mpg-CN
H3N-BH3
MeOH, rt, 8h
14.097
14.157
Time-->

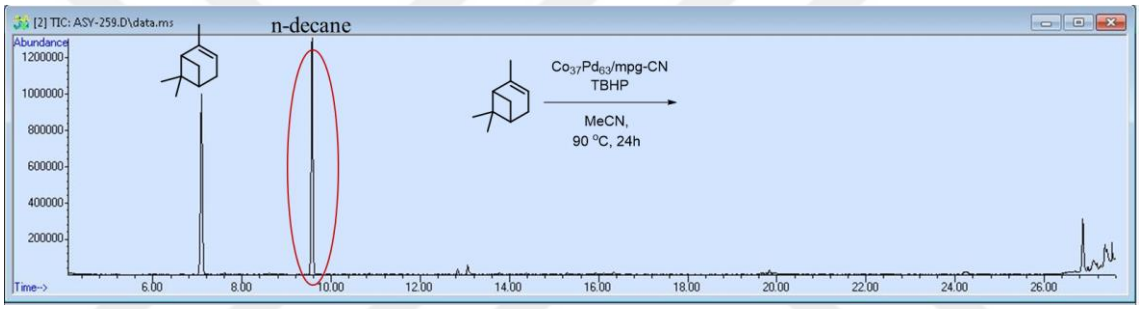
[2] TIC: ASY-259.D\data.ms
n-decane
Abundance
Co37Pd63/mpg-CN
TBHP
MeCN,
90 °C, 24h
Time-->

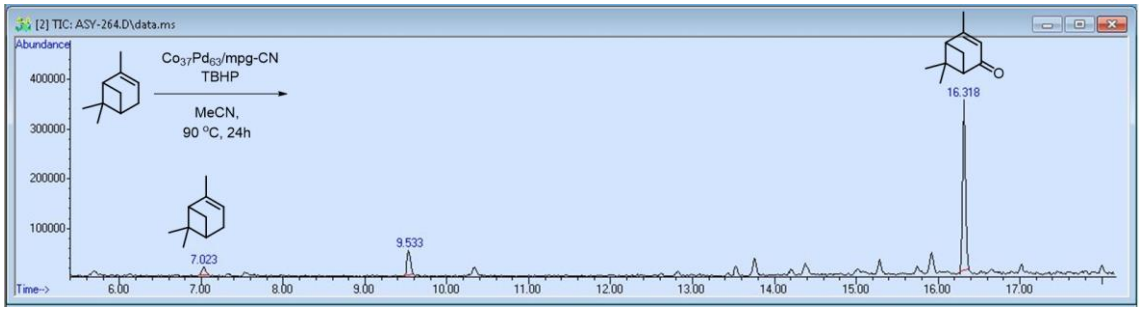
[2] TIC: ASY-264.D\data.ms
Abundance
Co37Pd63/mpg-CN
TBHP
MeCN,
90 °C, 24h
7.023
9.533
16.318
Time-->

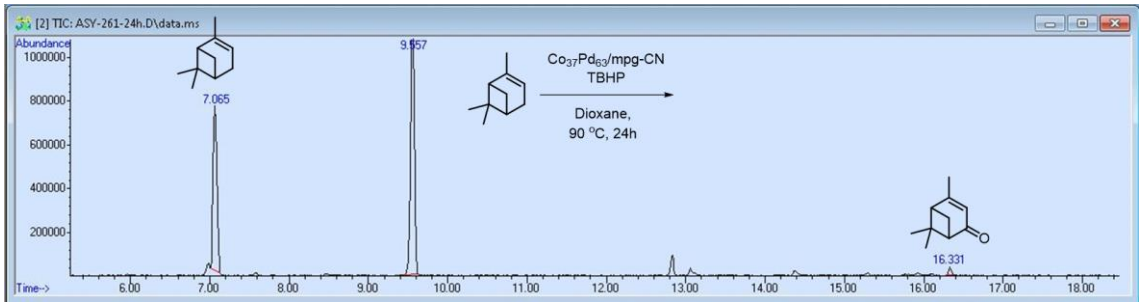
[2] TIC: ASY-261-24h.D\data.ms
Abundance
Co37Pd63/mpg-CN
TBHP
Dioxane,
90 °C, 24h
7.065
9.957
16.331
Time-->

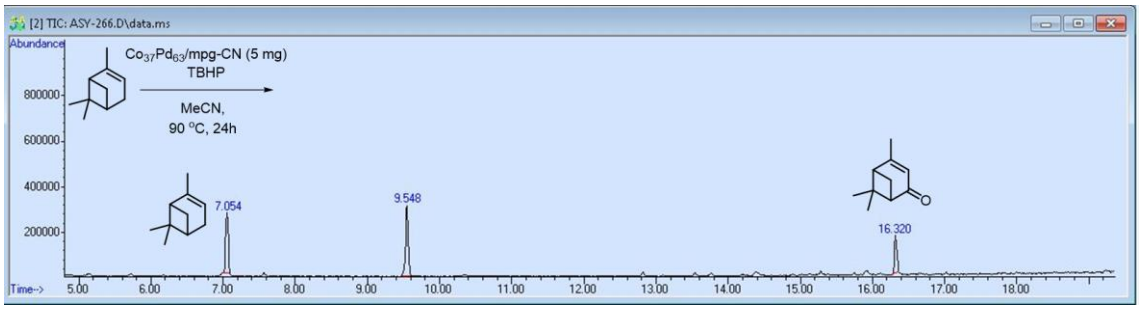
[2] TIC: ASY-266.D\data.ms
Abundance
Co37Pd63/mpg-CN (5 mg)
TBHP
MeCN,
90 °C, 24h
7.054
9.548
16.320
Time-->

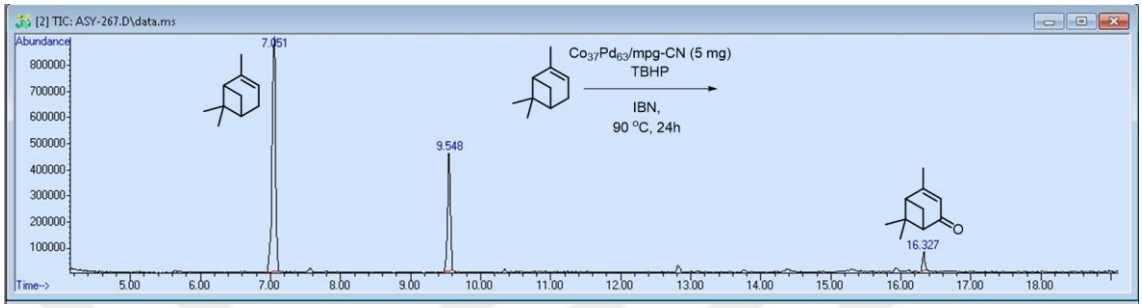
[2] TIC: ASY-267.D\data.ms
Abundance
7.051
Co37Pd63/mpg-CN (5 mg)
TBHP
IBN,
90 °C, 24h
9.548
16.327
Time-->

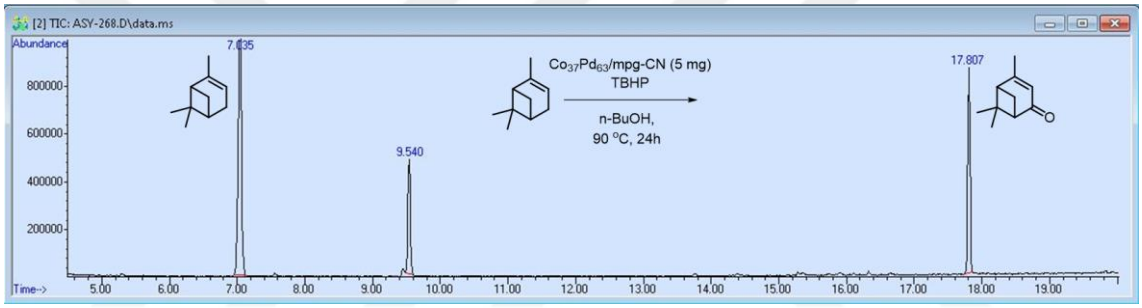
[2] TIC: ASY-268.D\data.ms
Abundance
7.035
Co37Pd63/mpg-CN (5 mg)
TBHP
n-BuOH,
90 °C, 24h
9.540
17.807
Time-->

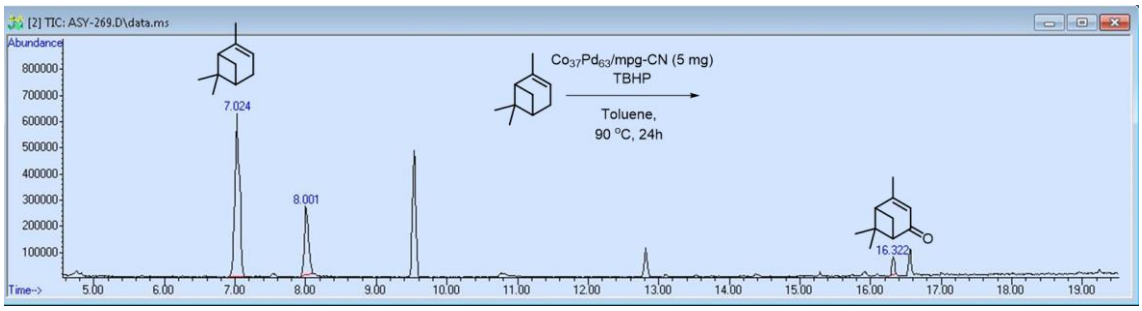
[2] TIC: ASY-269.D\data.ms
Abundance
7.024
Co37Pd63/mpg-CN (5 mg)
TBHP
Toluene,
90 °C, 24h
8.001
16.322
Time-->

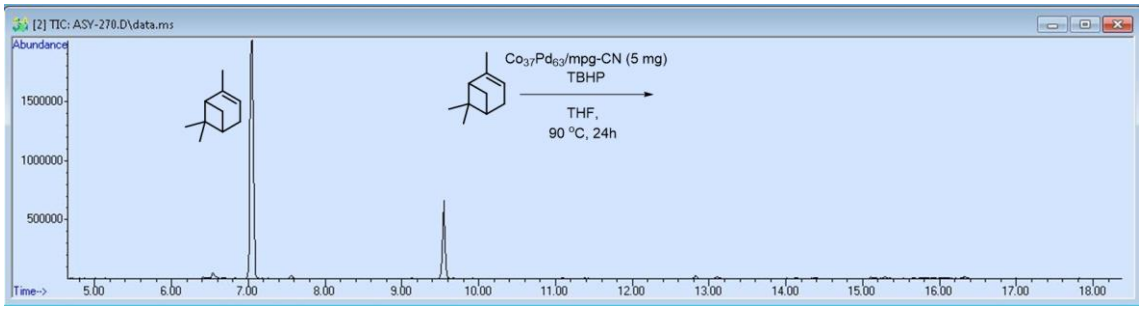
[2] TIC: ASY-270.D\data.ms
Abundance
Co37Pd63/mpg-CN (5 mg)
TBHP
THF,
90 °C, 24h
Time-->

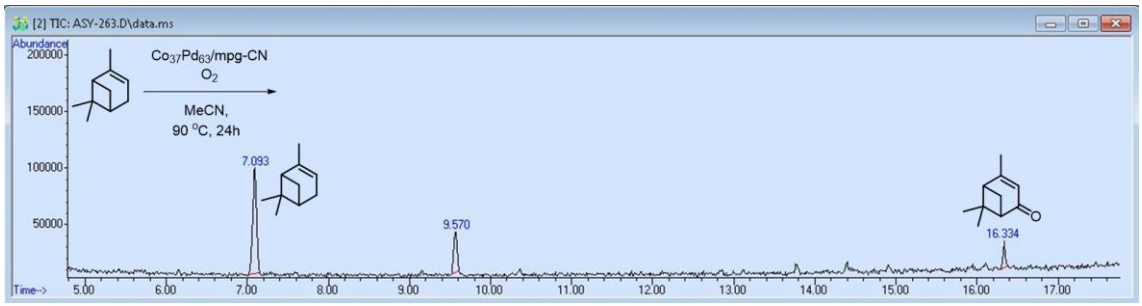
[2] TIC: ASY-263.D\data.ms
Abundance
Co37Pd63/mpg-CN
O2
MeCN,
90 °C, 24h
7.093
9.570
16.334
Time-->

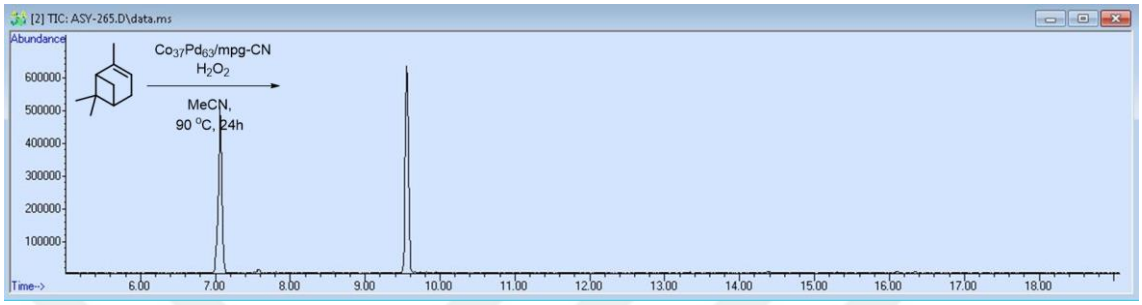
[2] TIC: ASY-265.D\data.ms
Abundance
Co37Pd63/mpg-CN
H2O2
MeCN,
90 °C, 24h
Time-->

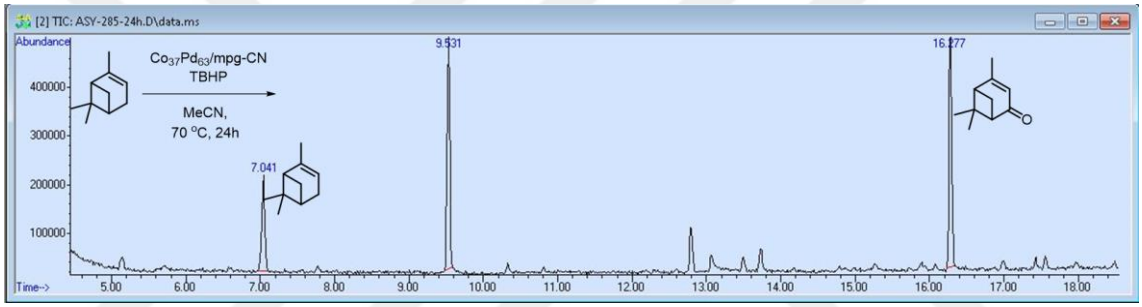
[2] TIC: ASY-285-24h.D\data.ms
Abundance
Co37Pd63/mpg-CN
TBHP
MeCN,
70 °C, 24h
7.041
9.531
16.277
Time-->

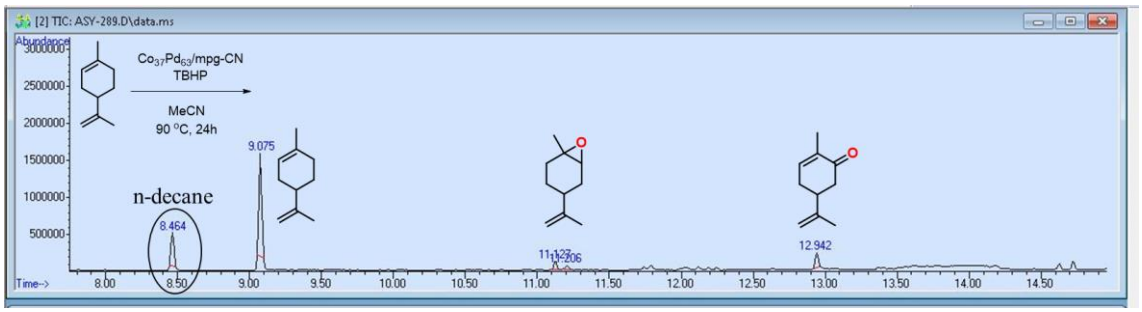
[2] TIC: ASY-289.D\data.ms
Abundance
Co37Pd63/mpg-CN
TBHP
MeCN
90 °C, 24h
n-decane
8.464
9.075
12.942
Time-->

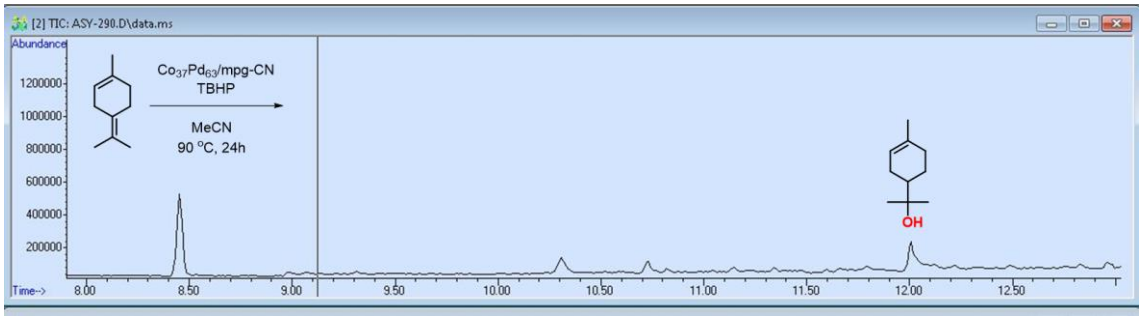
[2] TIC: ASY-290.D\data.ms
Abundance
Co37Pd63/mpg-CN
TBHP
MeCN
90 °C, 24h
OH
Time-->

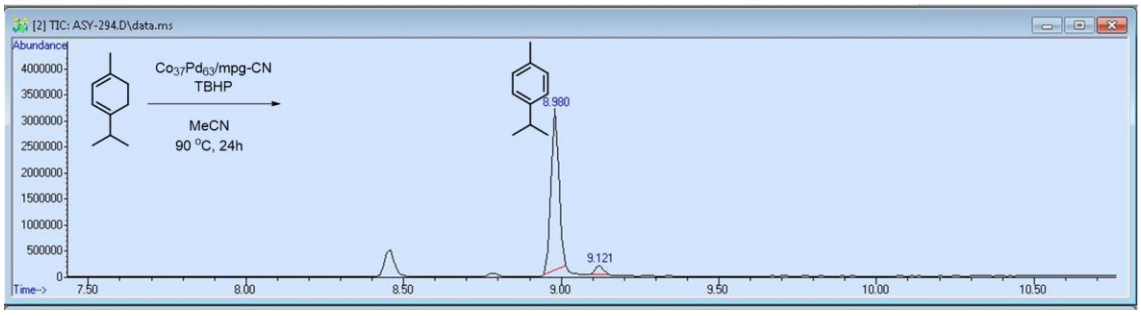
[2] TIC: ASY-294.D\data.ms
Abundance
Co37Pd63/mpg-CN
TBHP
MeCN
90 °C, 24h
8.980
9.121
Time-->

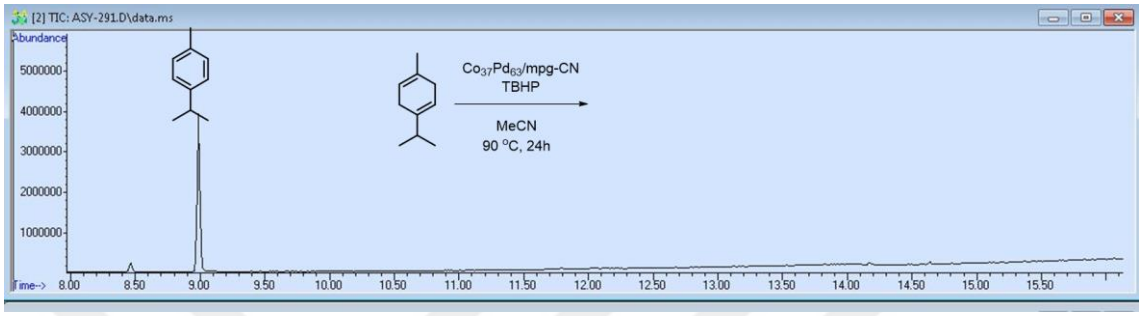
[2] TIC: ASY-291.D\data.ms
Abundance
Co37Pd63/mpg-CN
TBHP
MeCN
90 °C, 24h
Time-->

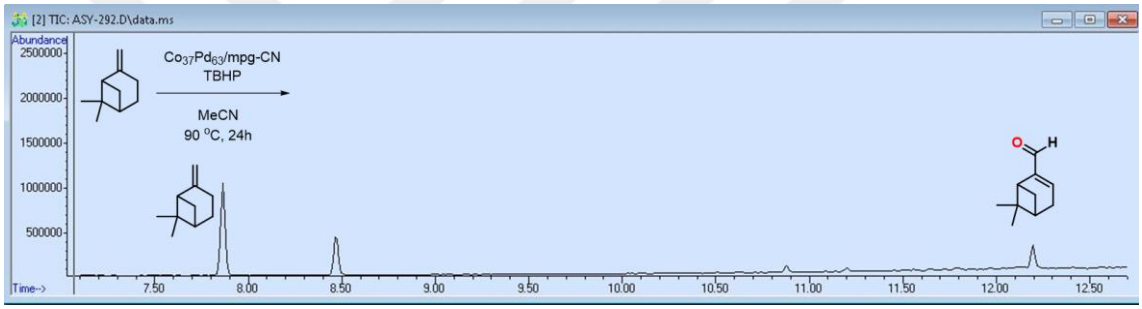
[2] TIC: ASY-292.D\data.ms
Abundance
Co37Pd63/mpg-CN
TBHP
MeCN
90 °C, 24h
O
H
Time-->

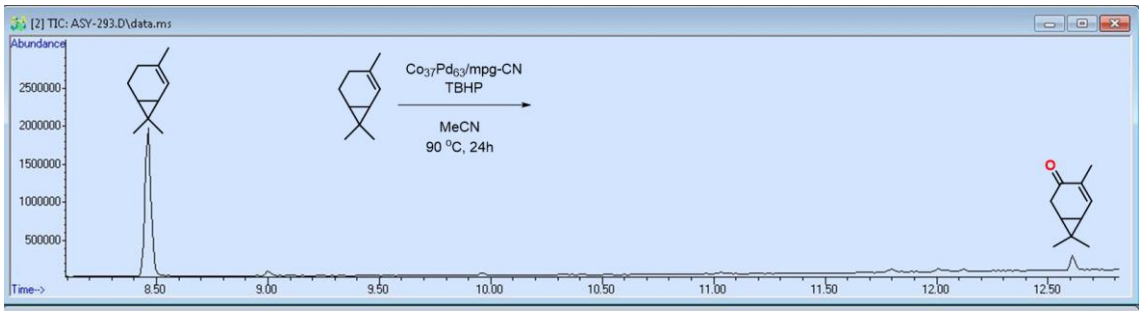
[2] TIC: ASY-293.D\data.ms
Abundance
Co37Pd63/mpg-CN
TBHP
MeCN
90 °C, 24h
O
Time-->

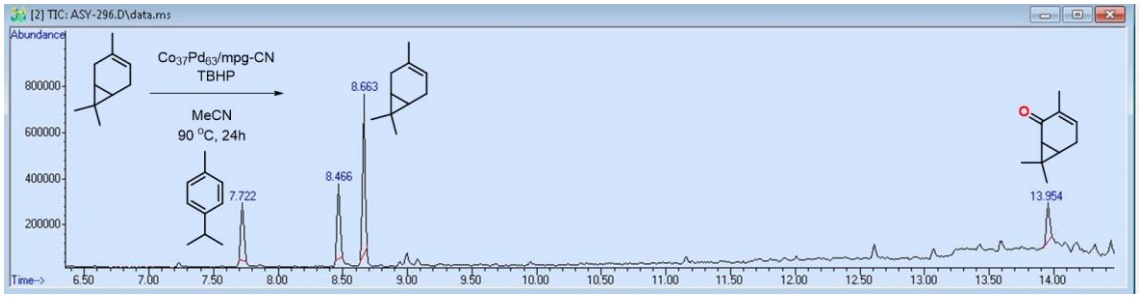
[2] TIC: ASY-296.D\data.ms
Abundance
Co37Pd63/mpg-CN
TBHP
MeCN
90 °C, 24h
8.663
8.466
7.722
O
13.954
Time-->

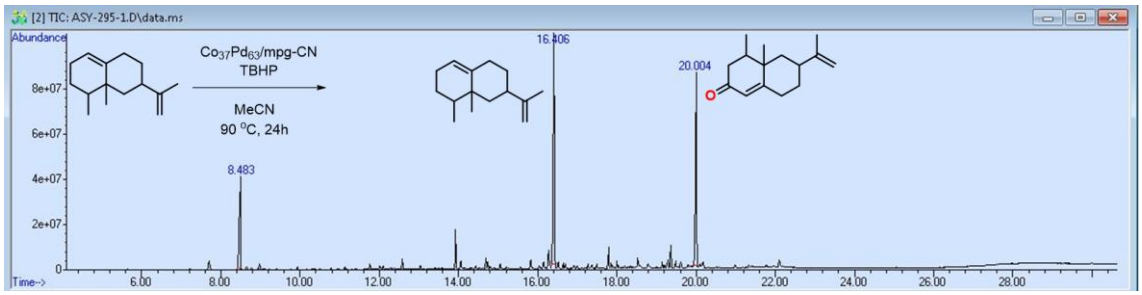
[2] TIC: ASY-295-1.D\data.ms
Abundance
Co37Pd63/mpg-CN
TBHP
MeCN
90 °C, 24h
8.483
16.406
20.004
Time-->

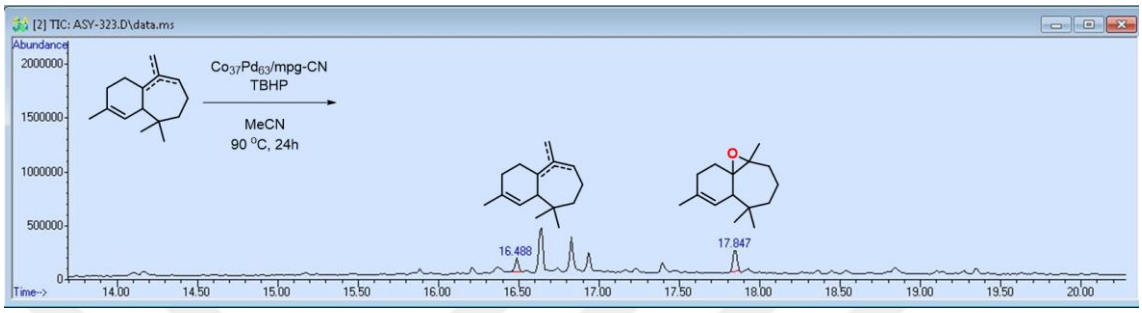
[2] TIC: ASY-323.D\data.ms
Abundance
Co37Pd63/mpg-CN
TBHP
MeCN
90 °C, 24h
16.488
17.847
Time-->